Advances in Civil Engineering

Sustainable Construction Engineering

Lead Guest Editor: Rahul V. Ralegaonkar
Guest Editors: Ana Bras, Paulina Faria, and S. K. Singh

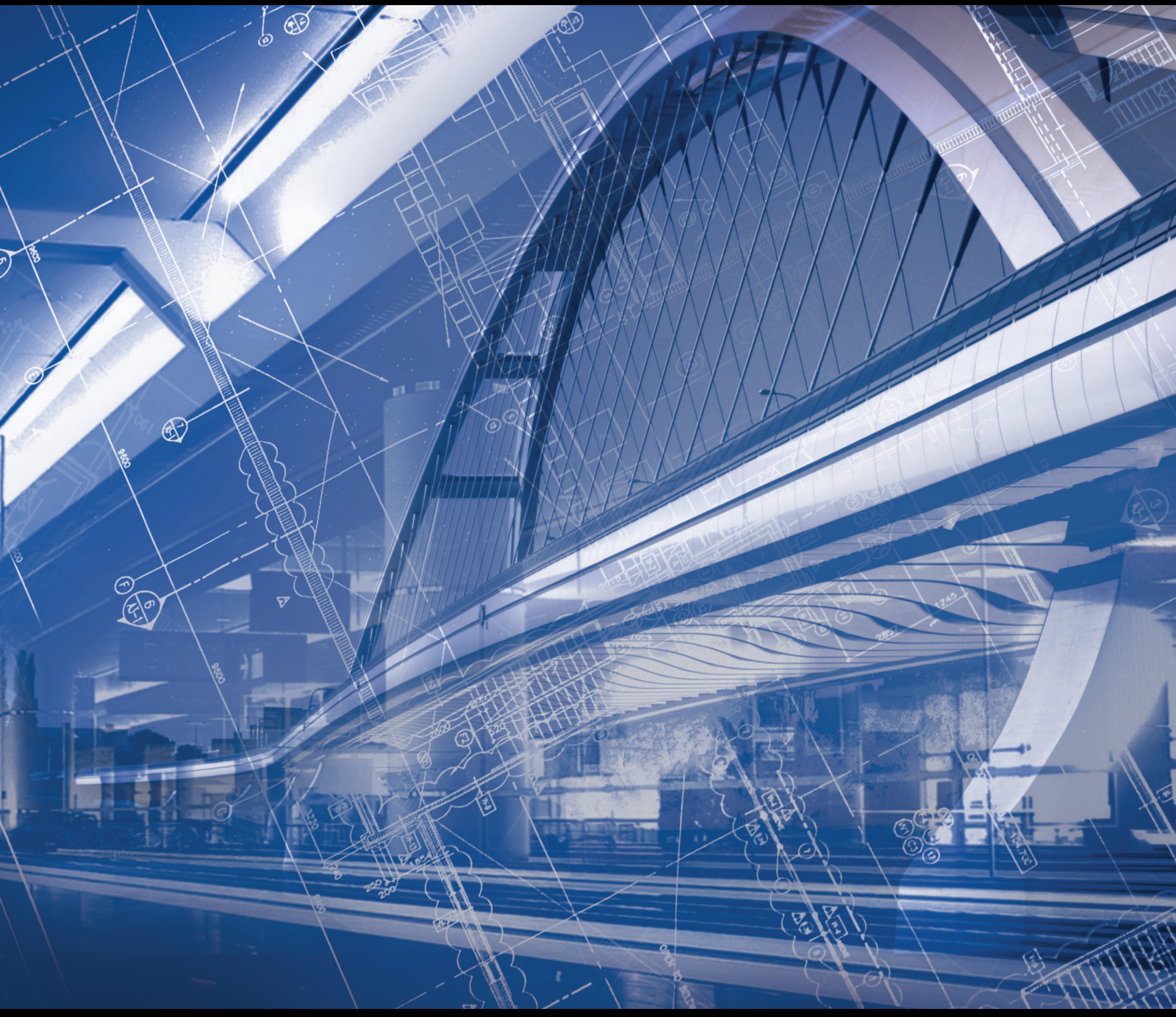

Sustainable Construction Engineering

Advances in Civil Engineering

Sustainable Construction Engineering

Lead Guest Editor: Rahul V. Ralegaonkar
Guest Editors: Ana Bras, Paulina Faria, and S. K. Singh

Contents

Hindawi
Advances in Civil Engineering
Volume 2021, Article ID 1013188, 15 pages
https://doi.org/10.1155/2021/1013188

Research Article

Experimental Study on SSRC under Eccentric Compression

Qingfu Li, Tianjing Zhang, Yaqian Yan, and Qunhua Xiang

School of Water Conservancy Engineering, Zhengzhou University, Zhengzhou 450001, China

Correspondence should be addressed to Yaqian Yan; yyq@zzu.edu.cn

Received 15 June 2021; Accepted 11 November 2021; Published 1 December 2021

Academic Editor: Rahul V. Ralegaonkar

The use of stainless steel bars can improve the durability and sustainability of building materials. Through the static performance test, this research analyzes the failure pattern and bearing performance of bias stainless steel reinforced concrete (SSRC) column. The influence of reinforcement ratio of longitudinal bars and eccentricity on the mechanical performance of specimens was studied. Different constitutive models of stainless steel bars were used to calculate the ultimate bearing capacity of the section of the column under eccentric compression column. Based on the experimental results, a method to modify the expression of the design specification is proposed. And, the results were compared with the test results. The results showed that the damage patterns and failure modes of SSRC columns are essentially the same as those of traditional reinforced concrete columns. The bearing capacity of SSRC columns rises with the increase in the longitudinal reinforcement ratio, and the ductility of the specimens is enhanced. The ultimate load of the specimen decreases with the rise in eccentricity but the deflection increases gradually. The strain distribution of the mid-span section of the SSRC column conforms to the plane section assumption. The bearing capacity of the specimen can be analyzed by referring to the calculation method of the specification, and some parameters in the calculation formula of the specification are modified to adapt to the design and calculation of the SSRC column.

1. Introduction

Reinforcement corrosion problems commonly exist in the concrete structure's durability, which lead to the unsustainability of construction projects. The investigation results show that more than 80% of concrete structures have a certain degree of durability problems or more serious steel corrosion just 5–10 years after construction [1]. How to improve the durability and sustainability of reinforced concrete structures under poor environmental conditions has become a pressing problem that requires solution. At present, the main measures taken to prevent the rapid corrosion of steel bars and improve the durability of reinforced concrete structures include [2–5] coating the surface of ordinary steel bars with antirust materials, using epoxy-coated steel bars and hot-dip galvanized steel bars, controlling the quality of concrete, and using stainless steel bars. In order to fundamentally solve a series of problems caused by steel corrosion, the use of stainless steel bars is the first choice. The stainless steel reinforcement is an alloy steel and contains significant amounts of chromium in order to protect the steel against rust. It can generate a thin and smooth layer of colorless, transparent oxide film on the surface of the weak corrosive medium to protect it against environmental conditions, such as air and water. Existing research has focused on the corrosion resistance of stainless steel; however, there has been relatively little research on the mechanical performance of SSRC members. The eccentric compression member is the most fundamental and important mechanical component in a building's structure [6]; as such, research on its mechanical performance will have theoretical significance and high application value.

Currently, in China, there is a range of research on and applications for stainless steel bars and their composite materials. It mainly focuses on two aspects: one is to study its corrosion law in simulated concrete pore fluid and the other is to study its corrosion law in mortar or concrete environment, which is usually compared with carbon steel bars in the same situation by monitoring the corrosion rate. In 2006, Guoxue et al. preliminarily discussed the mechanical properties of SSRC beams, slates, and columns [7–11]. In 2007, Yongsheng et al. studied and analyzed the influence of

the use of stainless steel bars on deflection, crack width, and ultimate bearing capacity of concrete beams and verified that the SSRC beams can meet the requirements of the maximum deflection and maximum crack width limits specified in the design of ordinary reinforced concrete structures[12]. In 2011, Huanxin et al. identified the difference between the constitutive models of stainless steel bars and ordinary steel bars [13]. In 2013, Jiawei et al. discussed the influence of use stainless steel bars on the bearing capacity of concrete beams through fatigue tests and studied the mechanical performance of SSRC beams, which included the stress-strain relationship between steel bars and concrete [10]. In 2013, Huitao conducted an experimental study on the mechanical properties of stainless steel bars, the bond properties between stainless steel bars and concrete, and the flexural properties of SSRC beams. The results showed that the strength, elongation, and cold bending property of stainless steel bars are higher than those of ordinary hot-rolled bars. The bonding performance between stainless steel bars and concrete is excellent. Under the same reinforcement condition, the bearing capacity of SSRC beam is higher than that of ordinary hot-rolled reinforced concrete beam, the failure law is consistent, and the plane section assumption is still applicable [14]. In 2014, Chen Long et al. used the potentiodynamic scanning technology and electron microscope test to study the critical chloride ion concentration of stainless steel bar and ordinary steel bar in simulated concrete pore fluid and concluded that the critical chloride ion concentration of the stainless steel bar is more than 20 times that of the ordinary steel bar and its corrosion resistance is far better than that of ordinary steel bar [15]. In 2016, Chengchang et al. proposed a preliminary calculation method for the bonding force between stainless steel bars and concrete [16], concluding that the carrying capacity of concrete beams with stainless steel bars was relatively greater. In 2018, Hailong et al. concluded that the critical value of corrosion resistance of stainless steel bars in the simulated liquid of freshly mixed concrete was more than 75 times that of carbon steel [17]. In 2018, Yi et al. studied the corrosion law of stainless steel bars and ordinary steel bars used in concrete structures. The results showed that the corrosion rate of carbon steel bars connected with stainless steel bars is significantly accelerated, and the galvanic corrosion is strengthened with the increase in corrosion time. At the same time, when two kinds of steel bars are overlapped, the galvanic corrosion is more severe [18]. In 2019, Chunyi et al. presented the bonding force formula between stainless steel bars and concrete [19].

However, overseas research on the application of stainless steel bars is a long-standing concern; as early as 1937, the Progreso Pier Bridge in Mexico used stainless steel ones to replace ordinary steel bars to improve the durability of the structure [20]. Foreign scholars' research on stainless steel bars mainly focuses on corrosion resistance. For example, in 1985, Zoob et al. carried out the corrosion resistance test on 304 stainless steel bars. The research showed that the allowable chloride content of stainless steel bars buried in concrete is 7–10 times that of ordinary steel bars in the same environment and there is no obvious corrosion of stainless steel bars. In 1988, Flint et al. buried one end of 316 stainless steel bars and carbon steel bars in concrete and exposed the other end to sea water. The experimental results showed that the local erosion of stainless steel bars only occurred in the immersion section of sea water, the stainless steel bars wrapped in concrete remained intact, and the overall strength was not affected. However, the corrosion of carbon steel bars was significant and the strength was seriously reduced [21, 22]. In 1995, McDonld and others conducted the same experimental study on SSRC members and the results showed that the corrosion resistance of SSRC members was better than that of ordinary reinforced concrete members [23]. In 1998, Bertolini et al. conducted corrosion tests on SSRC members in high pH value and high chloride environment and found that the corrosion resistance of stainless steel reinforcement is extremely excellent. It can still remain passive in high pH value and high chloride environment [24]. In 2002, Abreu et al. used sodium chloride solution to simulate concrete pore fluid and used the EIS method and ZRA method to study galvanic corrosion behavior of the stainless steel bar and carbon steel bar. The results show that if the carbon steel bar and stainless steel bar are connected in simulated pore fluid, the probability of galvanic corrosion is small [25]. Castro (2003) conducted tests on the mechanical properties and corrosion properties of the austenitic stainless steel rebar under both hot-rolled and cold-rolled conditions [26]. Blanco et al. experimentally compared the corrosion behavior of two traditional austenitic steels and a dual-phase stainless steel with that of low nickel austenitic steel [27]. In 2010, Milan Kouřil et al. studied the corrosion resistance of stainless steel bars by the electrochemical test, and the results showed that the critical chloride concentration of stainless steel bars in concrete structure depends not only on the chemical composition of stainless steel and the pH level of concrete pore fluid but also on the surface state of steel. Stainless steel bars with smooth surface have good corrosion resistance, while stainless steel bars with rough surface have weak resistance to chloride ion [28]. In 2013, Hansson et al. used the linear polarization method to compare the corrosion performance of the stainless steel bar and carbon steel bar in concrete environment with the same chloride concentration. The results showed that the corrosion of ordinary carbon steel bar occurred within two weeks, while the stainless steel bar began to rust after 139 weeks. The use of stainless steel bars has a significant effect on improving the service life of concrete structures [29]. And, Gastaldi and Bertolini tested the chloride-induced corrosion resistance of low nickel bidirectional stainless steel threaded bars in different temperature ranges and traditional austenitic stainless steel threaded bars [30]. In recent years, foreign studies on the mechanical properties of stainless steel have gradually increased. In 2015, Mdina et al. carried out a series of experimental studies on the structural properties of three kinds of stainless steel bars (austenitic AISI304, bidirectional AISI2304, and new bidirectional AISI2001) at reinforcement, section, and structural member levels, respectively [31]. In 2016, Gardner et al. conducted 164 heating tests on four kinds of stainless steel bars (1.4307[304Ln], 1.4311

[304Ln], 1.4162[LDX2101], and 1.4362[2304]) under high-temperature conditions [32]. In 2019, Yibu et al. conducted an experimental study on the strength of 59 stainless steel welding sections using through traditional welding and laser welding [33]. In 2019, Bemfica et al. studied axial torsional fatigue and cyclic deformation behavior of 304L stainless steel bars at room temperature [34].

Stainless steel bars have high strength, high flexural strength ratio, high fatigue life, high impact toughness, and other properties. The main problem of the current application of stainless steel reinforcement is the high price, which affects the initial cost of engineering construction. But, generally, the stainless steel reinforcement can only be used in the key parts of the actual project, so the proportion of stainless steel reinforcement in the whole project cost is very small and some other characteristics of stainless steel reinforcement also make its life cycle cost much lower than that of carbon steel [35]. Compared with ordinary steel bars, first of all, the application of stainless steel bars can reduce the thickness of concrete and the number of steel bars. Secondly, the transportation, processing, and installation of stainless steel bars have no special requirements, and the construction cost is 25% lower than that of epoxy-coated carbon steel bars. Thirdly, stainless steel reinforced concrete buildings require little or no maintenance which can reduce maintenance and inspection costs, thereby reducing the social cost of maintenance disrupting operations. The Federal Highway Administration (FHWA) conducted a cost analysis of three bridges built in Illinois with different rustproofing methods. The results showed that the initial cost of the bridge with stainless steel reinforcement increased by 16%, but it took about six times as long to crack, resulting in a significant reduction in maintenance costs [36]. V al et al. put forward a kind of time-varying probability model to predict the expected cost of repair and replacement, and then, the model was used to calculate different exposures of reinforced concrete structures in the marine environment under the conditions of life cycle cost. The results showed that although the price of stainless steel was six to nine times that of carbon steel, the use of stainless steel bars was justified on a life cycle cost basis [37]. Frank N. Smith analyzed the serious corrosion problems during the service of the Oland Bridge in Sweden, pointed out that if the bridge were constructed with stainless steel bars, the construction cost would only increase by 8%, but the 100-year life could be achieved with very little maintenance [38]. Cope et al. evaluated the superiority of stainless steel over conventional steel in terms of both long-term usage costs and user costs with the data from one Midwestern state in the United States, using Monte Carlo simulation methods for most of the analyzed scenarios, which proved that in the case of uncertainty, using stainless steel as the bridge reinforcement materials is more cost-effective than conventional steel [39]. Younis et al. conducted a life cycle cost analysis of high-rise buildings based on a 100-year study period and showed that the proposed combination using stainless steel bars had a life cycle cost (LCC) approximately 50% lower than the conventional combination (i.e., concrete containing fresh water, natural aggregate, and black steel) [40].

Although there has been much progress in the study of stainless steel bars, most has concentrated on the performance of the stainless steel material itself, such as stainless steel basic mechanical performance, weldability, and corrosion resistance. However, there has been relatively little research on the mechanical properties of concrete structural members containing stainless steel bars. When stainless steel bars are used in concrete compression members, whether the stainless steel bars and concrete materials can fully live up to their strengths needs to be verified through rigorous testing. In view of this, this paper will consider the SSRC columns as the research participants. Through testing, theoretical analysis, numerical simulation, and other technical methods, the mechanical performance of SSRC columns will be studied.

2. Experimental Design

2.1. Specimen. In order to conduct the study, eight SSRC eccentric compression columns were designed and constructed. The section determination of each specimen was 250 mm × 150 mm, with a height of 1000 mm. The form of symmetrical reinforcement was adopted, and the concrete cover thickness was 25 mm. The model of stainless steel bar used along the longitudinal direction of the specimen was 2304. The specific dimensions and reinforcement layout of the specimens are shown in Figure 1.

At the same time, six 150 mm × 150 mm × 150 mm standard concrete companion specimens were poured for each concrete bias specimen. These were used for testing the concrete strength of the specimens.

2.2. Experimental Methods. The design parameters of the specimens are listed in Table 1. The test was carried out on a WHY-5000 kN hydraulic pressure machine. In order to measure the strain on the concrete, six strain gauges were pasted equidistant on the middle section of the specimen. Three strain gauges were uniformly pasted on the surface of each longitudinal stainless steel bar of the specimen to measure the strain on the longitudinal steel bars. On the middle section of the bottom surface of the specimen, equidistant to each other, 5 displacement meters were placed to measure the deflection of the specimens. Figures 2 and 3 show the loading diagram and strain gauge distribution, respectively. Crack development, concrete strain, reinforcement strain, lateral displacement, and other test phenomena were observed and recorded during the test.

2.3. Mechanical Properties of Concrete and Reinforcement. In this experiment, 2304 stainless steel bars were used. Stainless steel specimens with diameters of 12 mm, 16 mm, and 25 mm were selected for tensile testing. The test results and the mechanical indexes of stainless steel bars are shown in Figure 4 and 5 and Table 2.

The design strength of the concrete specimen is C45, and the measured strength of the concrete test blocks is shown in Table 3. The axial compressive strength of concrete is calculated using formula (1), according to the

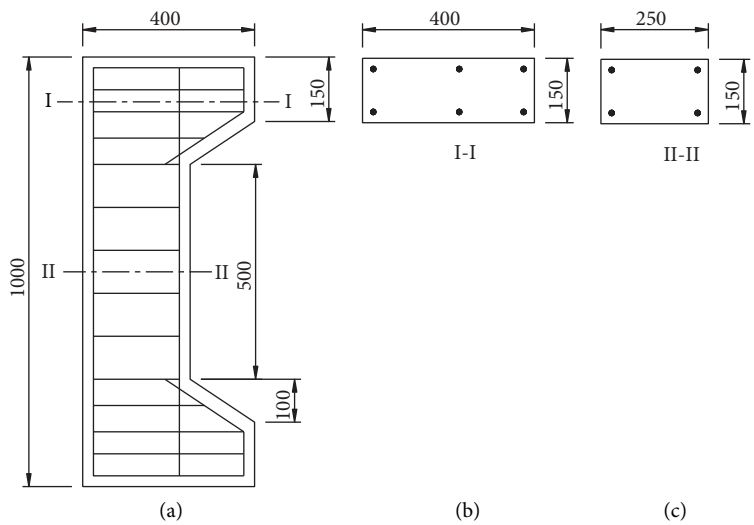

Figure 1: Schematic of specimen dimensions and reinforcement (mm).

Table 1: Specimen design parameters.

Specimen number	Strength grade of concrete	Sectional dimension (mm^2)	Initial eccentricity, e_0 (mm)	Longitudinal reinforcement diameter, d (mm)	Hoop reinforcement form, d (mm)
A-D1	C45	250 × 150	200	12	8@125
A-D4	C45	250 × 150	50	12	8@125
B-D1	C45	250 × 150	200	16	8@125
B-D2	C45	250 × 150	150	16	8@125
B-D3	C45	250 × 150	100	16	8@125
B-D4	C45	250 × 150	50	16	8@125
C-D1	C45	250 × 150	200	25	8@125
C-D4	C45	250 × 150	50	25	8@125

Note: letters A, B, and C represent the longitudinal stainless steel bars with diameters of 12 mm, 16 mm, and 25 mm respectively. D1, D2, D3, and D4 represent the initial eccentricity of 200 mm, 150 mm, 100 mm, and 50 mm, respectively, when the specimen is pressed.

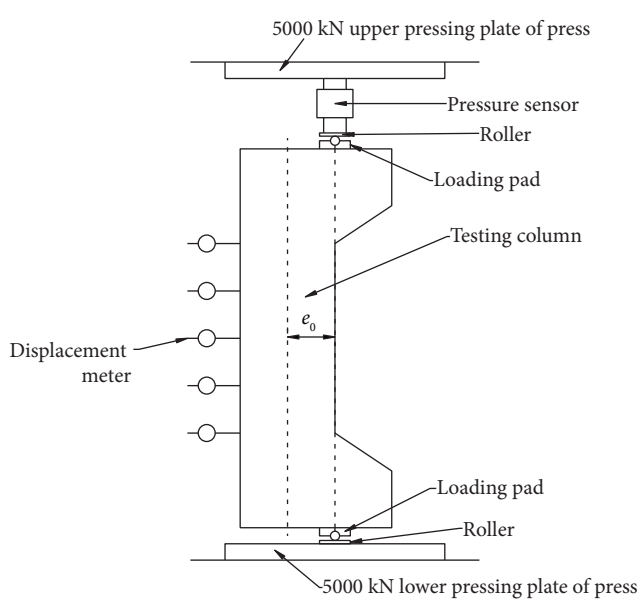

Figure 2: Experimental loading diagram.

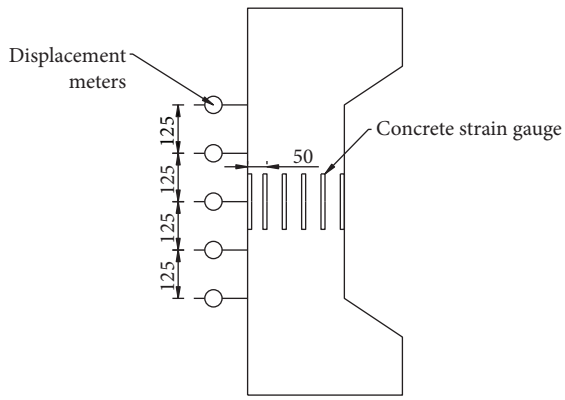

Figure 3: Distribution of the strain gauge (mm).

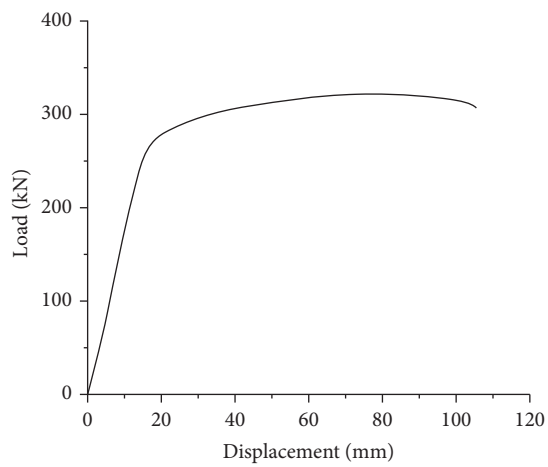

Figure 4: Load-displacement curve of stainless steel bars.

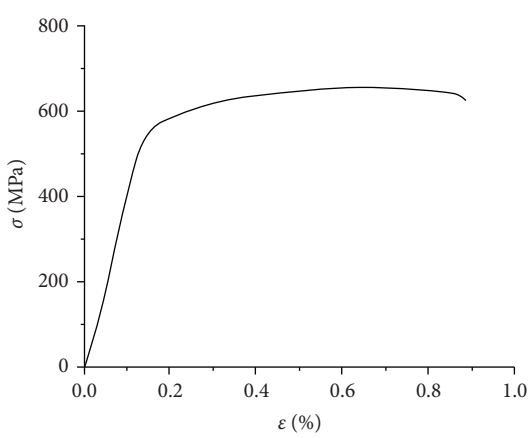

Figure 5: Stress-strain curve of stainless steel bars.

Code for Design of Concrete Structures (GB50010-2010). Considering that all the specimens are manufactured and tested under laboratory conditions, the reduction factor of 0.88 can be ignored, so the actual strength of the concrete can be calculated using formula (2). Calculations for the mechanical properties of the concrete are shown in Table 3.

$$f_{ck} = 0.88 \times 0.76 f_{cu,k}, \tag{1}$$

$$f_k = 00.76 f_{cu,k}. \tag{2}$$

3. Results and Discussion

3.1. Experiment Phenomena and Failure Modes. The experiments can be divided into two conditions: large eccentric compression, for which the initial eccentricities are 150 mm and 200 mm, and small eccentric compression, which includes the initial eccentricities of 50 mm and 100 mm. Specimens with D1/D2 in the specimen number are those with large eccentric compression, and the failure modes of specimens with large eccentric compression are essentially the same. When the load increased to 15–25% of the peak load, 2–4 horizontal cracks formed in the tensile zone of the SSRC columns. At the point of these cracks in the tensile zone, the strain on the stainless steel bars and the mid-span deflection of the SSRC columns greatly increased. As the load continued to increase, the cracks were more or less equally spaced, forming several major cracks. With further increase in the load, the width of the cracks increased, gradually extending to the compression zone, and the height

Table 2: Mechanical indexes of stainless steels.

Diameter (d/mm)	Tensile strength (MPa)	Yield strength (MPa)	Elastic modulus (10^5 MPa)	Elongation (%)
12	885.3	677.5	1.56	33.00
16	795.3	565.8	1.56	36.39
25	768.7	572.7	1.40	34.13

Table 3: Mechanical properties of concrete.

Specimen number	f_{cu} (MPa)	f_c (MPa)	Specimen number	f_{cu} (MPa)	f_c (MPa)
A-D1	43.47	33.04	B-D3	42.44	32.25
A-D4	42.64	31.65	B-D4	46.00	34.96
B-D1	45.20	34.20	C-D1	45.33	34.45
B-D2	44.93	34.15	C-D4	45.60	34.66

of the compression zone of the SSRC columns decreased. When the load reached 80–90% of the peak load, the stainless steel bars in the tensile zone were close to yield: the strain on the stainless steel bars rapidly increased, the height of the compression zone of the specimen decreased, the compressive strain on the concrete in the compression zone of the concrete columns and the stainless steel bars increased, and longitudinal cracks appeared. As the load continued to increase, the bearing capacity of the specimens decreased abruptly, the strain on the concrete in the compression zone reached the ultimate compressive strain state, and the specimens were crushed. On the destruction of the specimens, the concrete in the compression area was crushed and, while the stainless steel bars in the compression area did not yield, the stainless steel bars in the tensile area did. The lateral deflection of the specimens was large, and there were characteristics of ductile failure [41].

Specimens with D3/D4 in the specimen number are the specimens with small eccentric compression, and the failure modes of all specimens with small eccentric compression are essentially comparable. When the load increased to 25–40% of the peak load, several small cracks appeared in the tensile zone and the width of the cracks and their extension to the compression zone were not obvious. No main cracks formed, and the strain at the edge of the compression zone of the specimens increased rapidly. With an increase in the load, the strain on the stainless steel bars and concrete in the compression area of the specimens increased significantly and the cracks in the tensile area extended and developed slowly. When approaching failure conditions, longitudinal cracks appeared in the concrete in the compression zone. The destruction was sudden, without any visible symptoms, and the crushing area was large. When the specimens were destroyed, the reinforcement on the side closest to the loading point yielded, while the reinforcement on the side furthest from the loading point did not. The lateral deflection of the specimens was small, and the specimens showed certain characteristics of brittleness [41]. The failure mode of the specimens is shown in Figure 6.

3.2. Load-Deflection Curves. The load-deflection curves of each specimen are shown in Figure 7. It can be seen in the graphs that the load-deflection curve of SSRC eccentric compression columns is more or less divided into three stages. First is the linear elastic stage: the bearing capacity of the SSRC column is still small, the specimen has not cracked, and the deflection is also small. At this point, the relationship of load-deflection is approximately linear. The second stage is the nonlinear ascending stage: with the increase in load, both the amount and width of the cracks in the tensile zone of the specimen increase and the cracks further extend to the compression zone. The plastic characteristics of the specimen become increasingly obvious. At this stage, there is a nonlinear relationship between load and deflection and, with an increase in load, the relationship becomes increasingly obvious and the slope becomes smaller, indicating a continuous decline in specimen stiffness. The third stage is the descending stage: after the peak load exceeds, the deflection of the specimen increases and the load decreases [42]. The descending section of the large eccentric compression SSRC columns is relatively gentle, and the ductility of the specimens is good. In order to protect the instrument, the displacement gauge for some specimens was removed at 80% of the peak load, so the descending section is not presented in the graphs.

3.3. Influencing Factor Analysis. In order to study the stress of stainless steel bars in concrete eccentric pressure columns, the load-reinforcement strain curve of each specimen was drawn, as shown in Figure 8. As can be seen in Figure 8, the load-strain curve of the specimens with large eccentricity failure (A-D1, B-D1, B-D2, and C-D1) can be more or less divided into the following three stages: the elastic stage, where the strain and load of the tensile stainless steel bars show an approximate linear relationship; the nonlinear stage, where the height of the compression zone decreases gradually with an increase in load, the stress is redistributed, and the load-strain curve of the stainless steel bars deviated from the original linear relationship and began to show nonlinearity; and, finally, the approximate level development stage, where the stainless steel bar strain increased and the bars were close to yield. Making full use of tensile area and the compression area, the stainless steel bars did not yield. In the specimens with small eccentric failure (A-D4, B-D3, B-D4, and C-D4), the load-strain curve of the compressive steel bar is essentially the same as that of the

(a) (b)

Figure 6: Failure mode of the specimen. (a) Large eccentric compression failure. (b) Small eccentric compression failure.

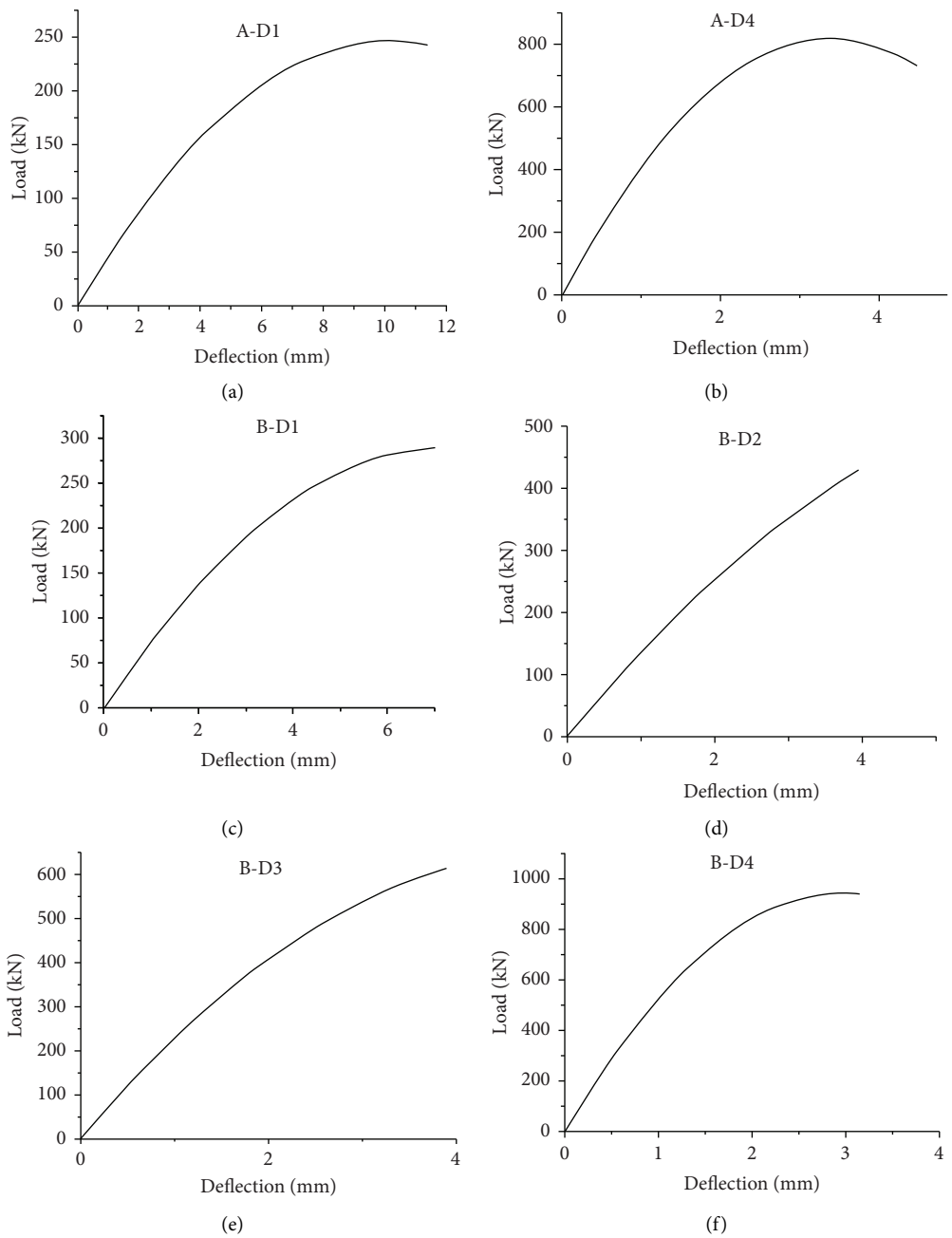

Figure 7: Continued.

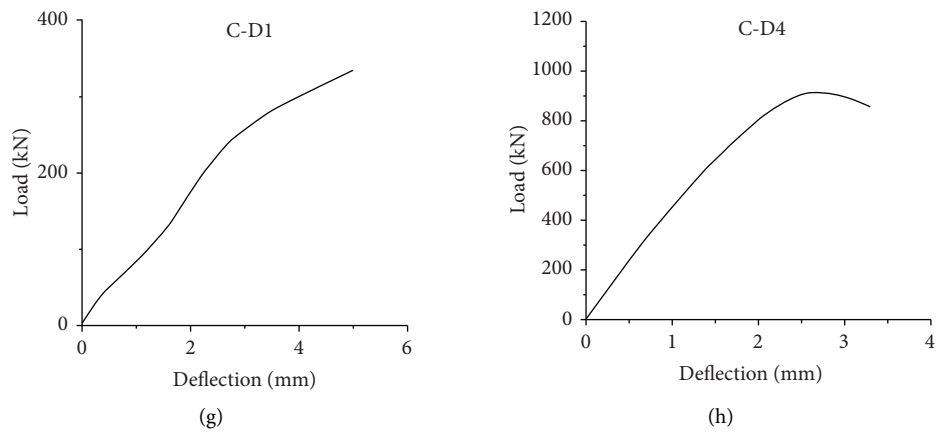

Figure 7: Load-deflection curve of the specimens.

tensile stainless steel bar in large bias pressure. The stainless steel bars in the compression zone ultimately yielded, meaning that the stainless steel bars in the compression zone can be fully utilized. The strain of the stainless steel bars in the tensile area is small, unyielding, and not fully utilized. This is synonymous with the small bias of ordinary concrete columns. When the eccentricity of the tensile stainless steel bars is 50 mm, the stainless steel bars furthest away from the loading point also appear to be under compression [42]. This is because the initial eccentricity is too small, so the steel bars in the tensile area of the specimen appear to be under compression, as shown in graphs (f) and (h) in Figure 8.

The load-deflection curves of different reinforcement ratios of longitudinal steels with the same eccentricity are displayed in Figure 9. It can be seen from the graphs that the ratio of longitudinal reinforcement has a significant influence on the bearing capacity and deflection of SSRC columns. When the initial eccentricity is 200 mm meaning the specimen is under large eccentricity compression, with the same load condition, the smaller the reinforcement ratio, the greater the deflection, and the flatter the load-deflection curve. When the initial eccentricity is 50 mm, in the case of small eccentricity compression, the change in the reinforcement ratio of longitudinal stainless steel has little effect on the deflection of the specimen.

Eccentricity has a significant effect on the load and deflection of concrete columns. Under the same conditions, the deflection corresponding to the ultimate load of the SSRC column rises with the increase in eccentricity, the load-deflection curves are gentler, and the bearing capacity of the specimens decreases. The comparison of the influence of eccentricity on the load-deflection curve of SSRC columns is shown in Figure 10 [43].

3.4. Main Results. The main results of this research are shown in Table 4. It can be seen from the table that, under the condition of large eccentricity pressure, the stainless steel bars on the tensile side have yielded, while the stainless steel bars on the compression side mostly have not. This phenomenon is different from that of ordinary carbon-reinforced concrete specimens. In the case of small eccentricity pressure, the steel on the compression side has mostly yielded, while the stainless steel bars on the side furthest from the loading point have not, which is consistent with that of ordinary carbon-reinforced concrete specimens [44–48]. Stainless steel bars can play a more beneficial role in concrete columns, but there are some disparities to ordinary reinforced concrete columns. As such, the calculation of SSRC columns cannot replicate the standard results of ordinary reinforced concrete columns.

4. Carrying Capacity Calculation

4.1. Verification of Plane Section Assumption. Figure 11 shows the distribution of strain in the mid-span section along the height under various loads. It can be seen that the strain distribution along the height of the column in the mid-span section of the specimen is uniform and mostly linear, which meets the requirements of plane section assumption [49].

4.2. Calculation of Ultimate Bearing Capacity. The mechanical properties of stainless steel bars are shown in Table 5.

The constitutive model of stainless steel adopts the Rasmussen model and the constitutive model of steel according to China's current standards [50].

The mathematical expression of the Rasmussen model is

$$\varepsilon = \begin{cases} \dfrac{\sigma_s}{E_0} + \varepsilon_{py}\left(\dfrac{\sigma_s}{\sigma_{0.2}}\right)^n, & \varepsilon \le \varepsilon_{0.2}, \\ \dfrac{\sigma_s - \sigma_{0.2}}{E_{0.2}} + \varepsilon_u\left(\dfrac{\sigma_m - \sigma_{0.2}}{\sigma_u - \sigma_{0.2}}\right)^m, & \varepsilon_{0.2} < \varepsilon \le \varepsilon_u, \end{cases} \tag{3}$$

where E_0 is the initial elastic modulus; ε_{py} is the residual strain, and $\varepsilon_{py} = 0.002$; $n = \ln 20/\ln(\sigma_{0.2}/\sigma_{0.01})$, and $\sigma_{0.01}$ is the point corresponding to the 0.01% residual strain of the steel bar; $E_{0.2}$ is the slope of the tangent line at the nominal yield point; $m = 1 + 3.5\sigma_{0.2}/\sigma_u$; and $\varepsilon_u = 1 - \sigma_{0.2}/\sigma_u$.

The mathematical expression of the steel bar constitutive model in China's current code is

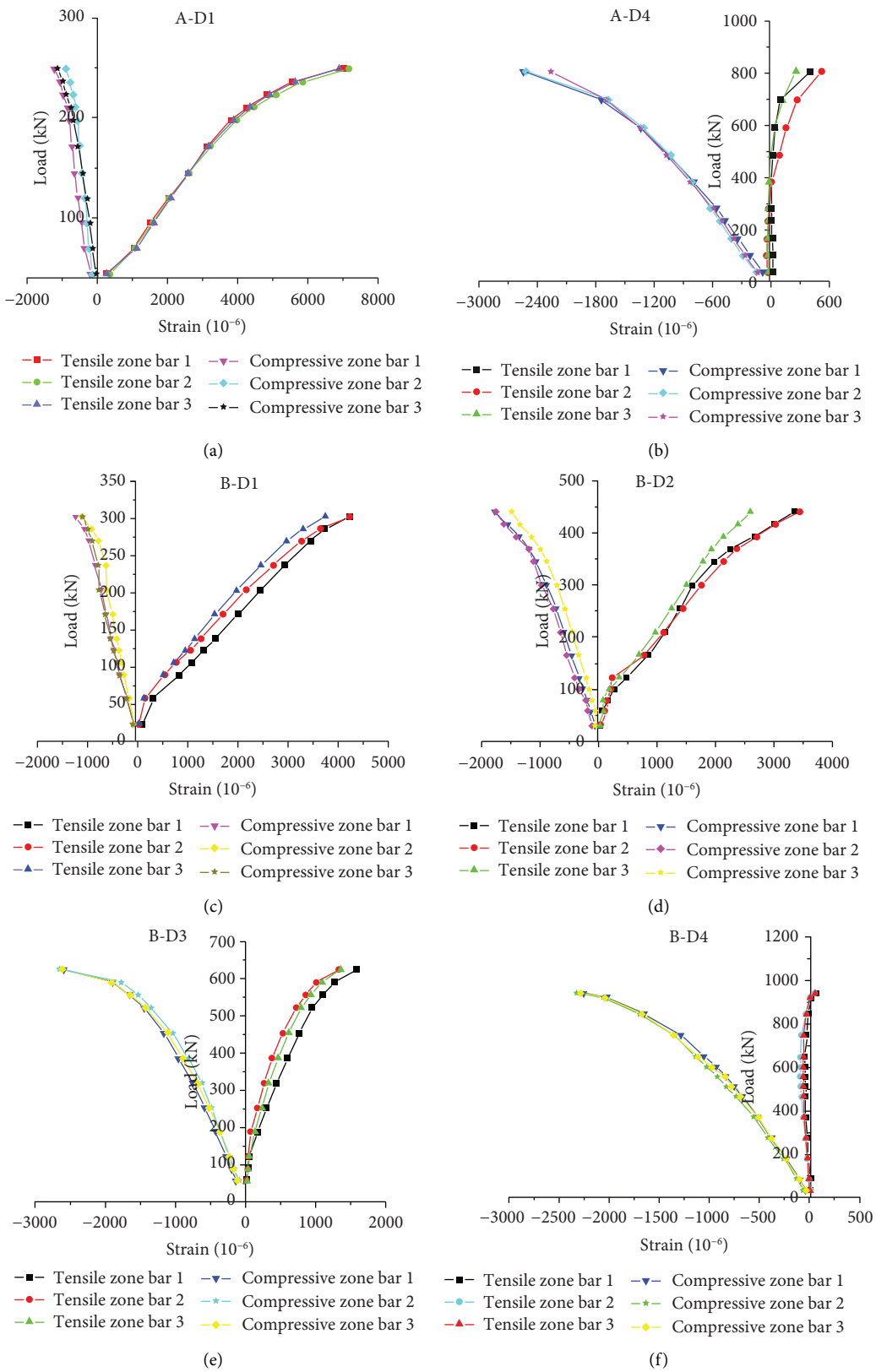

Figure 8: Continued.

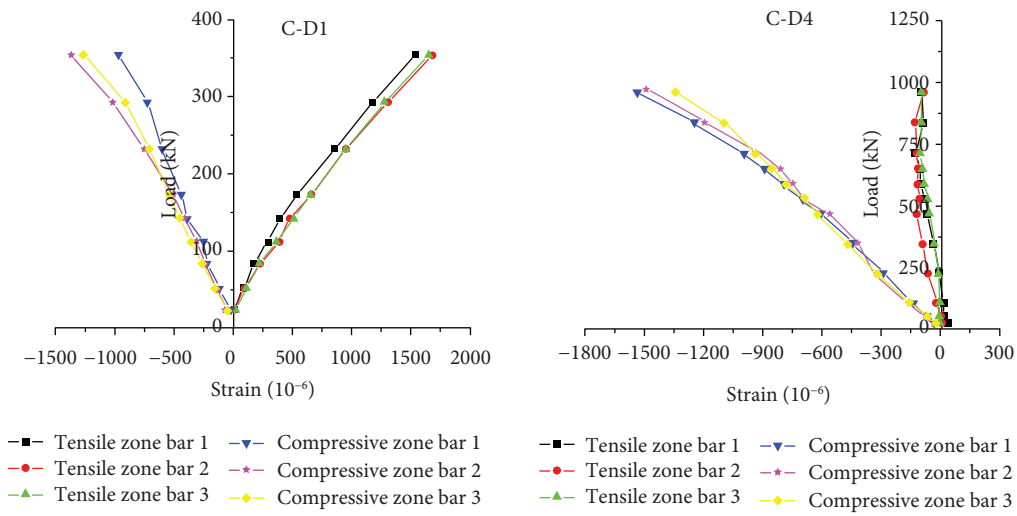

Figure 8: Load-longitudinal reinforcement strain curve of the specimen.

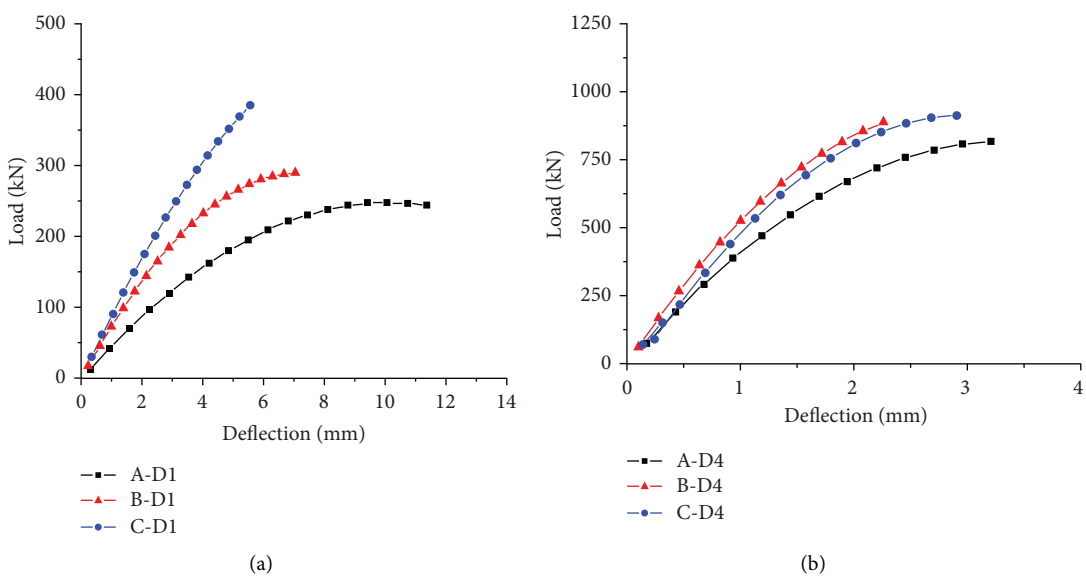

Figure 9: Influence of longitudinal reinforcement ratio on the load-deflection curve.

$$\sigma = \begin{cases} E_0\varepsilon, & \varepsilon \le \varepsilon_{0.2}, \\ \sigma_{0.2} + k(\varepsilon - \varepsilon_{0.2}), & \varepsilon_{0.2} < \varepsilon \le \varepsilon_u, \\ 0, & \varepsilon > \varepsilon_u, \end{cases} \tag{4}$$

where σ is the steel bar stress, E_0 is the initial elastic modulus of the steel, ε is the steel bar strain, $\sigma_{0.2}$ is the nominal yield stress of the stainless steel bar, $\varepsilon_{0.2}$ is the strain corresponding to the nominal yield stress of the steel bar, ε_u is the peak strain corresponding to the ultimate strength of the steel, and k is the slope of the hardened section of the steels, where $k = (\sigma_u - \sigma_{0.2})/(\varepsilon_u - \varepsilon_{0.2})$.

According to the force balance of the damaged section in the stainless steel reinforcement eccentric compression members and the momentary balance of the center point in the tension steel bars, the calculation formula for the bearing capacity of the rectangular section of the SSRC eccentric compression columns can be obtained [43]:

$$\begin{cases} N = f_c bx + \sigma_s' A_s' - \sigma_s A_s, \\ Ne = f_c bx\left(h_0 - \dfrac{x}{2}\right) + \sigma_s' A_s'(h_0 - a_s'). \end{cases} \tag{5}$$

The theoretical value of the ultimate bearing capacity of stainless steel bar concrete eccentric pressure specimens under two constitutive models can also be obtained, as demonstrated in Table 6.

4.3. Comparative Analyses. In this experiment, eight stainless steel bar eccentric concrete column bearing capacity

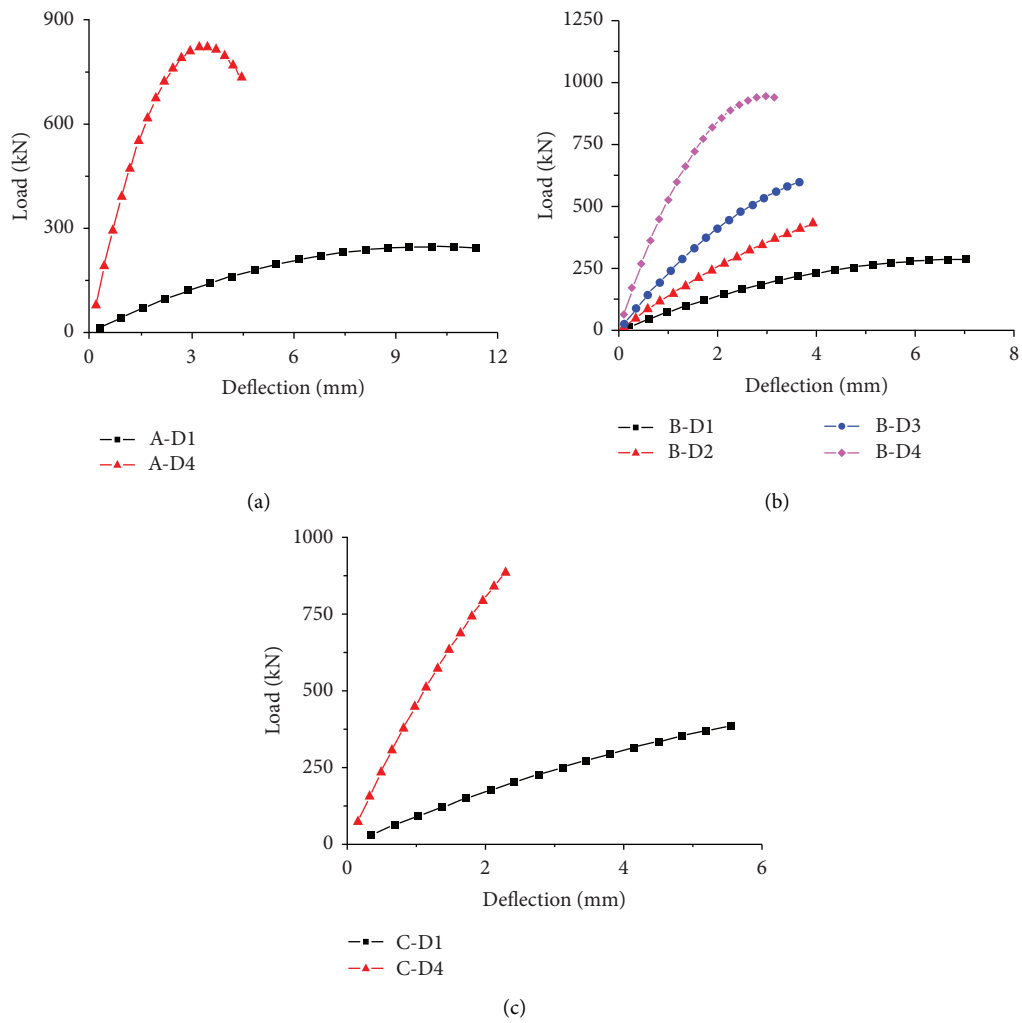

Figure 10: Comparison of the influence of eccentricity on the load-deflection curve.

Table 4: Main test data.

Specimen number	e_0/h_0	N_u (kN)	ε_s' (10^{-6})	ε_s (10^{-6})	Failure pattern
A-D1	0.913	242.2	−1195.05	6152.23	Large eccentricity
A-D4	0.228	807.2	−2422.90	384.45	Small eccentricity
B-D1	0.922	302.1	−1251.09	4183.15	Large eccentricity
B-D2	0.691	440.5	−1850.98	2983.35	Large eccentricity
B-D3	0.461	625.4	−2657.56	1707.61	Small eccentricity
B-D4	0.230	952.0	−2775.89	279.73	Small eccentricity
C-D1	0.941	353.5	−1166.36	1724.76	Large eccentricity
C-D4	0.235	1032.0	−1877.59	−16.99	Small eccentricity

Note: N_u represents the maximum bearing load of the specimen, and ε_s' and ε_s represent the strain of compression stainless steel and tension stainless steel bars, respectively, when the threshold load is reached. In this table, negative values represent compression and positive values represent tension.

tests were carried out and the experimental values were compared with the calculated theoretical values. The comparison results are shown in Table 6. Through comparative analysis, it can be seen that the ultimate bearing capacity of the stainless steel bar concrete column's eccentric load-bearing capacity failure specimen is similar to the theoretical calculation results of the stainless steel bar constitutive model. Considering the convenience of this calculation and verification, the steel constitutive model in China's current code is used to carry out the calculation. However, the calculation of the load-bearing capacity of the stainless steel bar eccentric compression member is more appropriate. Subsequently, China's normative model is revised to render the calculation results more relevant and provides a safety reserve. Formulas (6) and (7) are used to revise the standard model, and the revised results are shown in Table 7. It can be

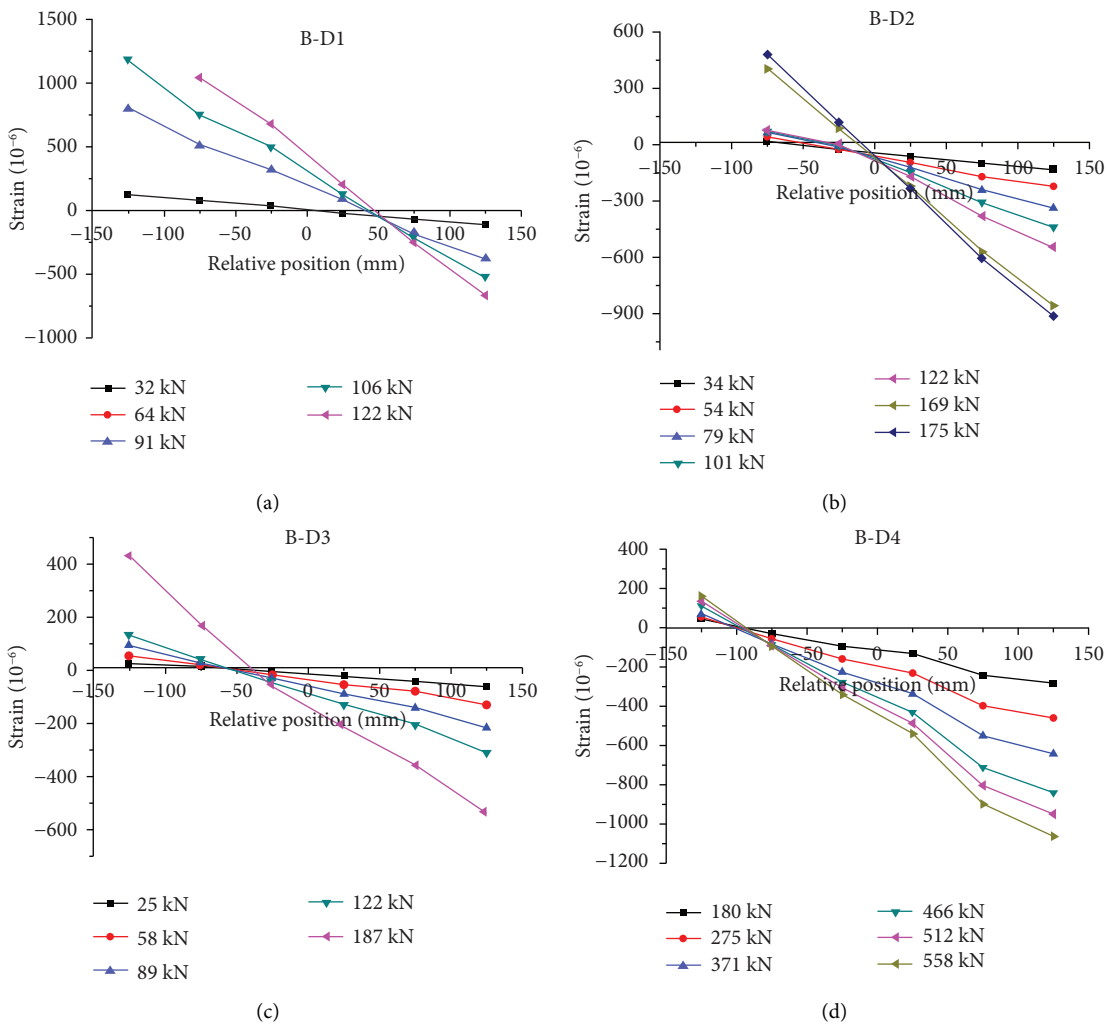

Figure 11: Strain-load relationship diagram of concrete.

Table 5: Mechanical properties of stainless steel bars.

$\varepsilon_{0.2}$	$\sigma_{0.2}$	ε_u	σ_u	E_s
0.0061	605 MPa	0.276	797 MPa	151 GPa

Table 6: Mechanical indexes of stainless steels.

Specimen number	Ultimate bearing capacity, N_u/kN			Failure pattern
	Rasmussen model	Standard model	Test value	
A-D1	249.51	263.15	242.2	Large eccentricity
A-D4	856.08	850.84	807.2	Small eccentricity
B-D1	337.02	284.23	302.1	Large eccentricity
B-D2	438.28	415.78	440.5	Large eccentricity
B-D3	745.62	730.30	625.4	Small eccentricity
B-D4	979.74	964.62	952.0	Small eccentricity
C-D1	640.03	633.03	653.5	Large eccentricity
C-D4	1093.04	1084.65	1032.0	Small eccentricity

Table 7: Comparison of the calculated value and test value of load-bearing capacity of the revised standard mode.

Specimen number	Ultimate bearing capacity N_u/kN		Ratio of test to calculated value
	Revised specification model	Test value	
A-D1	263.15	242.2	1.0865
A-D4	805.97	807.2	0.9985
B-D1	284.23	302.1	0.9408
B-D2	415.78	440.5	0.9439
B-D3	684.01	625.4	1.0937
B-D4	915.27	952.0	0.9614
C-D1	633.03	653.5	1.7958
C-D4	1025.77	1032.0	0.9940

seen in Table 7 that the error between the theoretical calculation value and the test value of the modified stainless steel eccentric compression specimen's bearing capacity is small. Within a reasonable range, formulas (6) and (7) can be used to modify the standard model.

For small eccentric compression members, when calculating the bearing capacity, the formula for calculating the strength of the eccentric compression concrete column is shown in (6). To complete the calculation, formula (6) is added to formula (5) and the small eccentric compression of the stainless steel is calculated. The theoretical calculated bearing capacity of the compression test piece is shown in Table 7.

$$f_c = 0.76 f_{cu} - \alpha. \tag{6}$$

For large eccentric compression members, the following calculation formula is used when calculating the bearing capacity to obtain the calculated theoretical bearing capacity value of SSRC columns, under large eccentric compression. The calculation results are shown in Table 7.

$$\begin{cases} N = f_c bx + \beta\left(\sigma_s' A_s' - \sigma_s A_s\right), \\ Ne = f_c bx\left(h_0 - \dfrac{x}{2}\right) + \sigma_s' A_s'\left(h_0 - a_s'\right). \end{cases} \tag{7}$$

Here, $\alpha = 1.5$ and $\beta = 0.8$.

5. Conclusions

In this paper, eight stainless steel bar compression components are fabricated and tested. Based on the test results, the mechanical properties of the SSRC column are analyzed and the calculation formula of the bearing capacity of the SSRC eccentric compression members is proposed. The factors affecting the bearing capacity of the SSRC column are analyzed. The main conclusions are as follows:

(1) The failure mode of SSRC eccentric compression column in the ultimate state is the same as that of the ordinary concrete column. When large eccentric compression member destruction occurs, the concrete in the compression zone is crushed. However, the stainless steel bars in the compression zone did not yield, whereas the stainless steel bars in the tensile zone did. The lateral deflection of the specimen is relatively large, and it displayed characteristics of ductile failure. In the case of small eccentric compression member failure, the stainless steel bars near the loading point yielded, while the stainless steel bars furthest from the loading point did not. The lateral deflection of the specimen is relatively small, which indicates that it is a brittle failure.

(2) The deflection-load curve of the eccentric compression column of stainless steel bars can be more or less divided into the following three stages: linear elastic stage, nonlinear ascending stage, and descent stage. Compared with small eccentricity, the descending section of the large eccentricity compression member is relatively gentle and the ductility of the specimen is superior. In the case of large eccentric compression—when the specimens are in the same load—the smaller the reinforcement ratio, the greater the deflection. In the case of small eccentric compression, the change in reinforcement ratio of the longitudinal stainless steel bars has little effect on the deflection of the specimens. When other conditions are comparable, the deflection corresponding to the ultimate load of the SSRC column rises with the increase in eccentricity and the load-deflection curve is gentler.

(3) The strain distribution of the mid-span section of the SSRC column with small eccentric pressure is consistent with the assumption of the plane section along the height, which can be theoretically calculated according to the plane section assumption.

(4) The Rasmussen model and the current model, adopted with the Chinese specifications, are the two types of stainless steel reinforcement constitutive models currently most commonly used. The formula of the specification model is simple and easy to calculate, allowing for the modification of the specification model. According to the comparison of the revised and test results, the conclusions indicate that the correction formula can be used in the stainless steel bearing capacity calculation for reinforced concrete eccentric pressure column. The calculated results are representative of the test values.

Although this paper has done a lot of research on the mechanical properties of SSRC eccentric pressure members, because of the complexity of SSRC structure and the discrete nature of the concrete material test, there are still many problems to be solved: (1) Explore the size effect of concrete structure on SSRC to solve whether the construction of large-volume SSRC can be used to analyze the current relevant theories. (2) Search the suitable type of concrete structure in which the strength of stainless steel bars can play out to the greatest extent. (3) Carry out the experimental research about the flexural, shear, and fatigue resistance of stainless steel reinforced concrete structure. For the application and development of stainless steel bars in practical engineering, more comprehensive research and comparison are needed.

Data Availability

The data used to support the findings of this study are available from the corresponding author upon request.

Conflicts of Interest

The authors declare that there are no conflicts of interest regarding the publication of this paper.

Acknowledgments

This research was funded by the National Natural Science Foundation of China, under grant number 51679220.

References

[1] J. Zhang, C. Li, and X. Zheng, *Research on Stainless Steel Reinforcement Concrete Structure*, People's Communications Press, Beijing, China, 2015.

[2] H. Geng, *Experimental Study on Mechanical Properties of Stainless Steel Reinforcement and Structure for Bridge*, Zhengzhou University, Zhengzhou, China, 2013.

[3] J. Wang, "Research on the causes of steel bar corrosion and anti-corrosion design in concrete," *Concrete*, no. 8, pp. 41-42, 2008.

[4] G. J. Van den Berg and A. H. Liang, "Study on SSRC," *Architectural Technology*, vol. 31, no. 2, p. 105, 2000.

[5] J. Wang, *Study on Bonding Properties of Stainless Steel Reinforcement to concrete*, Zhengzhou University, Beijing, China.

[6] B. Hu, *Research on Compression Performance of FRP Constrained concrete Columns*, Hefei University of Technology, Hefei, China, 2010.

[7] G. Zhang and M. Wu, "Application and development of SSRC," *Journal of Foshan University of Science and Technology (Natural Science Edition)*, vol. 24, no. 2, pp. 10–13, 2006.

[8] G. Zhang, Y. Xu, and Z. Ding, "Experimental study on flexural performance of SSRC beams," *Railway Construction*, no. 2, pp. 13–15, 2008.

[9] G. Zhang, F. Zhao, and Z. Zhang, "Experimental study on seismic behavior of SSRC beams," *China Railway Science*, vol. 31, no. 5, pp. 35–40, 2010.

[10] J. Huang, *Experimental Study on Fatigue Behavior of SSRC Bridge Beams*, Guangdong University of Technology, Guangdong, China, 2013.

[11] G. Zhang, C. Wang, and J. Huang, "Nonlinear analysis on SSRC columns under low-cyclic load," *Applied Mechanics and Materials*, vol. v256-259, pp. 588–591, 2013.

[12] Y. Xu, *Experimental Study on Mechanical Properties of SSRC Beams*, South China University of technology, Guangdong, China, 2007.

[13] H. Yuan, Y. Wang, and Y. Shi, "Preliminary study and application prospect of SSRC," *Architectural Science*, vol. 27, no. 5, pp. 101–105, 2011.

[14] H. Geng, *Experimental Study on Mechanical Properties of Stainless Steel Bars and Members for Bridges*, Zhengzhou University, Zhengzhou, China, 2013.

[15] L. Chen, Y. Qu, and Y. Tang, "Critical chloride concentration of stainless steel reinforcement," *Corrosion & Protection*, vol. 35, no. 5, pp. 446–449, 2014.

[16] C. Li, W. He, and J. Lu, "Bonding performance between stainless steel reinforcement and concrete," *Highway Communication Technology*, vol. 33, no. 12, pp. 15–20, 2016.

[17] H. Wang, J. Ling, and X. Sun, "Experimental study on corrosion resistance of carbon steel bars and stainless steel bars in simulated concrete pored fluid," *West China Communications Science and Technology*, no. 2, pp. 66–69, 2018.

[18] Y. Zhou, D. Zou, and H. Wang, "Corrosion law of carbon steel stainless steel connection in concrete simulation solution," *Concrete*, no. 1, 2018.

[19] C. Xu, Y. Yuan, and B. Lu, "Anchorage design and reliability analysis of duplex stainless steel bars and concrete," *Journal of Shenyang Jianzhu University (Natural Science Edition)*, vol. 35, no. 3, pp. 445–452, 2019.

[20] P. Borges, E. Moreno, A. Acosta, A. Knudsen, O. Rincon, and M. Madrid, *Inspecting a Half-century Reinforced concrete Pier Made with Stainless Steel Reinforcement in Mexico*, 2002.

[21] Z. Zhang and Q. Zheng, *Corrosion Resistant Stainless Steel Bars*, Foreign bridges, Punjab, India, 1997.

[22] X. Xu, *Research Trends of Stainless Steel Bars Abroad*, Shandong building materials, Shandong, China, 2000.

[23] D. McDonld, M. Sherman, and D. Pfeier, "Stainless steel reinforcing as corrosion protection," *Concrete International*, vol. 17, no. 5, 1995.

[24] L. Bertolini, P. Pedeferri, and T. Pastore, "Stainless steel in reinforced concrete structures," in *Proceedings of the 2nd International Conference under Severe Conditions, v01*, Tromso, Ed., pp. 21–24pp. 21–, Rome, Italy, June 1998.

[25] C. Abreu, M. Cristobal, M. Montemor, and X. Novoa, "Galvanic coupling between carbon steel and austenitic stainless steel in alkaline media," vol. 47, no. 13, pp. 2271–2279, 2002.

[26] H. Castro, C. Rodriguez, F. J. Belzunce, and A. F. Canteli, "Mechanical properties and corrosion behaviour of stainless steel reinforcing bars," *Journal of Materials Processing Technology*, vol. 143-144, pp. 134–137, 2003.

[27] G. Blanco, A. Bautista, and H. Takenouti, "EIS study of passivation of austenitic and duplex stainless steels reinforcements in simulated pore solutions," *Cement and Concrete Composites*, vol. 28, no. 3, pp. 212–219, 2006.

[28] K. Milan, N. Pavel, and B. Martin, "Threshold chloride concentration for stainless steels activation in concrete pore solutions," *Cement and Concrete Research*, vol. 40, no. 3, pp. 431–436, 2010.

[29] C. Hansson, M. Islam, and B. Bergsma, "Chloride induced corrosion behavior of stainless steel and carbon steel reinforcing bars in sound and cracked concrete," *Corrosion Houston Tx*, vol. 69, no. 3, pp. 303–312, 2013.

[30] M. Gastaldi and L. Bertolini, "Effect of temperature on the corrosion behaviour of low-nickel duplex stainless steel bars

in concrete," *Cement and Concrete Research*, vol. 56, pp. 52–60, 2014.

[31] E. Medina, J. M. Medina, A. Cobo, and D. M. Bastidas, "Evaluation of mechanical and structural behavior of austenitic and duplex stainless steel reinforcements," *Construction and Building Materials*, vol. 78, pp. 1–7, 2015.

[32] L. Gardner, Y. Bu, P. Francis, N. R. Baddoo, K. A. Cashell, and F. McCann, "Elevated temperature material properties of stainless steel reinforcing bar," *Construction and Building Materials*, vol. 114, pp. 977–997, 2016.

[33] Y. Bu and L. Gardner, "Finite element modelling and design of welded stainless steel I-section columns," *Journal of Constructional Steel Research*, vol. 152, pp. 57–67, 2019.

[34] C. Bemfica, L. Carneiro, E. N. Mamiya, and F. C. Castro, "Fatigue and cyclic plasticity of 304L stainless steel under axial-torsional loading at room temperature," *International Journal of Fatigue*, vol. 125, pp. 349–361, 2019.

[35] H. Wang, *Application And Discussion Of Stainless Steel Reinforcement In Bridge Construction At Home And Abroad*, 2016.

[36] N. Ireland, *Use Of Stainless Steel Reinforcement In Highway Structures*, Stationery Office, London, UK, 2001.

[37] D. V. V al and M. G. Stewart, "Life-cycle cost analysis of reinforced concrete structures in marine environments," *Structural Safety*, vol. 25, no. 4, pp. 343–362, 2003.

[38] N. Frank and P. Smith, "Stainless steel reinforcement for concrete construction," in *Proceedings of the 12th Middle East Conference and Exhibition*, Rome, Italy, June 2008.

[39] A. Cope, Q. Bai, A. Samdariya, and S. Labi, "Assessing the efficacy of stainless steel for bridge deck reinforcement under uncertainty using Monte Carlo simulation," *Structure and Infrastructure Engineering*, vol. 9, no. 7, pp. 634–647, 2013.

[40] A. Younis, U. Ebead, S. Judd, and S. Judd, "Life cycle cost analysis of structural concrete using seawater, recycled concrete aggregate, and GFRP reinforcement," *Construction and Building Materials*, vol. 175, pp. 152–160, 2018.

[41] Dalian University of technology, *Hydraulic Reinforced concrete Structure*, China Water & Power Press, Beijing, China, 4th edition, 2012.

[42] J. Ye and G. Li, *Principles of Structural Design*, China Communication Press, Beijing, China, 4th edition, 2018.

[43] D. Mao, *Study on Mechanical Behavior of 500 MPa Reinforced concrete Compression Members*, Zhengzhou University, Zhengzhou. China, 2008.

[44] B. Li, *Strength and Ductility of Reinforced Concrete and Frames Constructed Using High- Strength Concrete*, University of Canterbury, Christchurch, New Zealand, 1994.

[45] C. Ma, X. Li, and L. Wang, "Stress analysis of steel reinforced high strength concrete eccentrically loaded columns," *Journal of Shenyang Architecture University (Natural Science Edition)*, vol. 22, no. 3, pp. 388–392, 2006.

[46] J. Pan, W. Wang, and X. Jin, "Study on characteristics of FRP confined reinforced concrete short columns under eccentric load," *China Civil Engineering Journal*, vol. 38, no. 2, pp. 46–50, 2005.

[47] Q. Wang and G. Zhao, "Experimental study on ductility of high strength concrete columns," *Journal of building structure*, vol. 16, no. 4, pp. 22–31, 1995.

[48] P. H. Chuang and S. K. Kong, "Strength of reinforced concrete columns," *Journal of Structural Engineering*, vol. 124, no. 9, pp. 992–998, 1998.

[49] X. Sun, X. Fang, and L. Guan, *Mechanics of Materials*, Higher Education Press, Beijing, China, 5th edition, 2009.

[50] K. J. R. Rasmussen, "Full-range stress-strain curves for stainless steel alloys," *Journal of Constructional Steel Research*, vol. 59, no. 1, pp. 47–61, 2003.

Hindawi
Advances in Civil Engineering
Volume 2021, Article ID 9422352, 15 pages
https://doi.org/10.1155/2021/9422352

Research Article

Impact of Addition of Banana Fibres at Varying Fibre Length and Content on Mechanical and Microstructural Properties of Concrete

Rodgers B. Mugume, Adolph Karubanga, and Michael Kyakula

Department of Civil and Environmental Engineering, Kyambogo University, Kampala, P.O. Box, 1, Kyambogo, Uganda

Correspondence should be addressed to Rodgers B. Mugume; rmugume@kyu.ac.ug

Received 14 April 2021; Accepted 30 September 2021; Published 8 October 2021

Academic Editor: Rahul V. Ralegaonkar

This experimental study aimed at investigating the impact of addition of banana fibres on the mechanical (compression, splitting tension, and flexure) and microstructural (microscopic morphology and Energy Dispersive X-ray Spectroscopy) properties of concrete. Concrete mixes comprising of banana fibres of varying fibre lengths (40, 50, and 60 mm) and fibre contents (0.1, 0.2, 1.0, 1.5, and 2.5%) were assessed. Addition of banana fibres to concrete was observed to significantly impact on compressive strength only at lower fibre contents of up to 0.25% for all fibre lengths. Fibre length had no significant impact on compressive strength at lower fibre contents of up to 0.25%, but shorter fibres were observed to perform better than longer ones at higher dosages more than 0.25%. Increase in fibre content positively impacted on tensile strength of concrete at relatively lower fibre dosages of up to 1%. Similarly, fibre length impacted on tensile strength of concrete at lower fibre contents of up to 1% and, longer fibres were observed to be more effective than shorter ones. Addition of banana fibres generally did not greatly contribute to flexural strength of concrete but had a marginal impact only when shorter fibres were used at lower fibre dosages. Also, microstructure of concrete was improved through better bonding between the fibres and the matrix and reduction in porosity of the matrix, which resulted in improved mechanical properties of the composite. Banana fibres further contributed to changes in phases of the composite structure of Banana fibre-reinforced concrete (BFRC) through a reduction in its interplanar spacing and lattice structure. For optimal purposes, addition of banana fibres should be limited to a maximum of 1% fibre content preferably using shorter fibre lengths. Further research to improve flexural strength of BFRC to meet minimum technical requirements is required before it can be considered for structural applications.

1. Introduction

Concrete is one of the most widely used material in the construction industry because it offers good strength and durability properties, and its primary constituents are readily available and cheap [1–3]. Despite its numerous advantages, concrete is also well known to have several weaknesses, such as a low tensile strength capacity that is significantly lower than its higher capacity to resist compressive loading, brittleness, low postcracking capability, and low fracture resistance [4–10]. This makes it highly susceptible to large tensile or flexural stress-induced damages that often lead to cracking in concrete, which in turn negatively impacts on its strength and durability [6, 11, 12].

Recently, natural fibres have been advanced as an alternative reinforcing material to conventional synthetic fibres owing to their environmental and economic benefits [13–20]. Natural fibres are readily available, biodegradable, cheaper, and recyclable, and they have been observed to have high tensile and flexural strengths as well as low elongation at break, hence rendering them widely accepted in construction industry [21–24]. Elbhiery et al. [20] compared and summarised the mechanical properties of various plant fibres and E-glass. However, studies conducted on the performance of natural fibres have

pointed to durability-related problems, such as their inability to deal with external damage due to moisture absorption, biological microorganisms, sulphate, or chloride attack, as well as internal damage mainly because of compatibility issues between fibres (due to presence of organic substances such as waxes, lignin, and pectin) and alkaline-cement paste environment [13, 15, 25–29]. Nonetheless, the benefits associated with the utilization of natural fibres in reinforcing concrete outweigh the disadvantages; besides, corrective measures can be undertaken to mitigate the likely shortcomings through fibre surface modification and/or treatments [30, 31].

Also, limited studies have been conducted on utilization of some natural fibres, such as banana, sisal, hemp, coconut, and jute fibres, among others as reinforcing materials in concrete [19, 20]. Banana fibres are a good prospect because they can easily be extracted from banana pseudostems, which are otherwise often left to rot in plantations in form of an agricultural waste. Studies conducted on Banana fibres have indicated that they possess good performance properties, are environment friendly, are less expensive, and are readily available, and thus, it can be utilized to improve mechanical properties of concrete [9, 10, 14, 20, 32–35]. However, studies carried out have majorly been concentrated on a single fibre length while investigating the fibre content [7, 9, 10, 34–36]. Furthermore, limited research has been conducted on the impact of banana fibres on microstructure of concrete. Microstructure of fibre-reinforced concrete comprises aggregates, bulk cementitious matrix, and the interfacial transition zone as well and the fibre-matrix interfacial zone [37]. It is important to study the microstructure of concrete in order to develop a better understanding of the relationship between a specific microstructural feature and a distinct physical, chemical, or engineering property of the material [38, 39]. Scanning Electron Microscope (SEM) is mostly utilized to investigate and examine microstructural characteristics of concrete [40, 41]. Most studies on microstructure of concrete have mainly concentrated on sisal, eucalyptus, coconut, sugarcane, and basalt fibres but not banana fibres [8, 40, 42, 43]. A study on the effect of banana fibres on microstructure by Humphrey [7] focused on the application of the fibres in mortar but not concrete. Therefore, the purpose of this experimental study is to investigate the influence of different banana fibre lengths and fibre contents on the mechanical and microstructural properties of concrete. Findings of the study will provide a better understanding of the properties of banana fibres as well as the impact of varying fibre lengths and contents on the mechanical and microstructural properties of concrete.

2. Materials and Methods

2.1. Materials

2.1.1. Cement. Portland cement (CEM I 42.5 N) conforming to ASTM C150 [44] was used in all mixes. Chemical composition and the physical and mechanical properties of cement are given in Tables 1 and 2, respectively.

2.1.2. Aggregates. Coarse and fine aggregates used were crushed granite stone and river sand, respectively. The particle size distribution and physical properties of the aggregates complied with ASTM C33 [45] and are shown in Figure 1 and Table 3, respectively.

2.1.3. Banana Fibres. Banana fibres used were obtained by manually scrapping them from the banana sheath of the harvested pseudostems and then cut into different sizes. To deal with the durability shortcomings associated with organic substances that are found in natural fibres, such as waxes, lignin, and pectin, fibres were first treated by immersion in 5% sodium hydroxide solution for 60 minutes at room temperature. Thereafter, fibres were thoroughly washed with tap water for a minimum of 10 minutes to remove the hemicellulose, lignin, and wax surrounding the cellulose. This process is known to exposes cellulose and increase surface roughness of the fibres, as well as improving their interfacial bonding strength [46]. Cut banana fibres as well as their geometry and mechanical characteristics are shown in Figure 2 and Table 4, respectively. Also, the microscopic morphology of fibres observed by Scanning Electron Microscope (SEM) are shown in Figure 3.

2.2. Mix Proportions. Normal strength concrete mixes of C20/25 class were prepared using OPC (Ordinary Portland Cement) and crushed stone with the maximum nominal size of 19 mm. Some parameters of the mix proportion were kept constant for all mixes: W/C of 45%, water content of 192 kg/m^3, and sand to aggregate ratio (s/a) of 50%. Addition of banana fibres of different lengths and volume fractions was the main differentiation of the mixes. Three fibre lengths of 40 mm, 50 mm, and 60 mm were used in this experimental study and applied at varying volume fractions by weight of cement of 0.1%, 0.25%, 1.0%, 1.5%, and 2.5%. The mix design methods were used in conformity with the ACI standards [47, 48]. Mix proportions and banana fibre quantity of concrete per cubic meter are given in Tables 5 and 6, respectively.

2.3. Sample Preparation. Mixing process of concrete was in conformity with the ACI standards [47, 48] and involved pouring of aggregates, sand, and cement into an electrically operated mechanical mixer. Specifically, for only banana fibre-reinforced concrete, manual dispersion of the fibres into the mixer was done followed by dry mixing for 60 seconds. Thereafter, water was added into the mixer, and the ingredients were further mixed for 90 seconds. Dry mixing was necessitated in Banana Fibre-Reinforced Concrete (BFRC) to ensure good fibre dispersion, which resulted in a homogeneous composite and circumvented the balling effect, which would otherwise lead to the formation of fibre balls during mixing of concrete.

Concrete test specimens for compressive strength, split tensile strength, and flexural strength were all cast in triplicate as shown in Table 7, resulting in a total of 144 samples. After casting, the specimens were cured in air for 24 hours

Table 1: Chemical composition of cement.

Chemical composition	SiO_2	CaO	Fe_2O_3	MgO	Al_2O_3	SO_3	LOI	I.R
Percentage (%)	22.86	65.08	4.07	1.95	5.05	2.41	1.12	1.33

Table 2: Physical and mechanical properties of cement.

Type	Blaine fineness (0.08 mm) % (m^2/g)	Specific surface area (m^2/g)	Standard consistency	Soundness (mm)	Setting time (min)		Compressive strength (MPa)	
					Initial	Final	2 d	28 d
CEM I 42.5 N	2.2	349.9	27.8	0.5	154	293	20.9	48.1

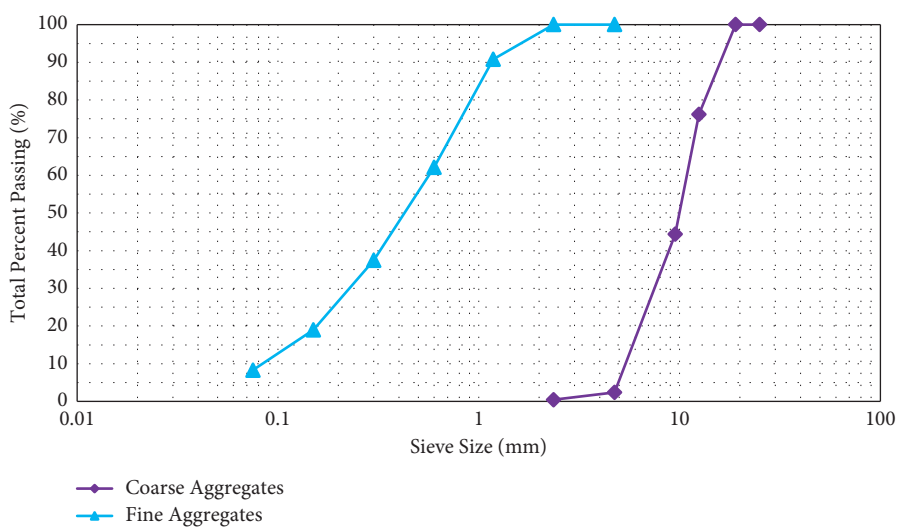

Figure 1: Particle size distribution of coarse and fine aggregates.

Table 3: Physical properties of aggregates.

Material properties	Coarse aggregate	Fine aggregate
Type	Crushed	River sand
Maximum size (mm)	19	4.75
Fineness modulus, FM	2.86	—
Water absorption (%)	0.61	0.37
Apparent density (g/m^3)	2800	2850
Mica content (%)	0.0	—
Fines < 0.075 mm (%)	2.74	—
Flakiness index (%)	—	9.5
Elongation index (%)	—	11.6

and thereafter demolded, immersed in a water tank, and cured at temperature of 20 ± 2°C for 28 days.

2.4. Test Method. Compressive and splitting tensile strength tests were performed in accordance with BS EN 12390-3 [49] and ASTM C496/C496M–17 [50], respectively. A Universal Testing Machine (UTM) with a 3000 kN maximum capacity was used at the loading rate of 0.6 MPa/s for compressive strength and 0.7 to 1.4 MPa/min for splitting tensile strength with the test setups as shown in Figures 4 and 5 , respectively. The maximum applied loads at failure were used to compute the compressive and tensile strengths using equation (1 and 2), respectively.

$$f_c = \left(\frac{P}{bd}\right), \tag{1}$$

where f_c is the compressive strength, MPa; P is the maximum applied load indicated by the testing machine, N; b and d are the average width and depth of specimen, mm.

$$f_t = \left(\frac{2P}{\pi l d}\right), \tag{2}$$

where f_t is the tensile strength, MPa; P is the maximum applied load indicated by the testing machine, N; l and d are the average length and diameter of specimen, mm.

Flexural tests under three-point loading were carried on a UTM with a capacity of 2500 kN at a loading rate of 0.1 mm/min in accordance with ASTM C293/C293M-16 [51] and the test setup is shown in Figure 6. The maximum applied load obtained at failure was used to calculate the flexural strength using equation (3).

$$f_f = \left(\frac{3Pl}{2bd^2}\right), \tag{3}$$

where f_f is the flexural strength, MPa; P is the maximum applied load indicated by the testing machine, N; b and d are the average width and depth of specimen, mm; and l is the span length of test specimen, mm.

Figure 2: Cut banana fibres.

Table 4: Geometry and mechanical characteristics of banana fibres.

Fibre parameter	Property
Stiffness (mm)	56.8
Weight (g)	56.8
Linear mass density (g/m)	1953
Diameter (μm)	102.82
Breaking strength (gf)	142.17
Breaking elongation (%)	3.22
Tensile strength (MPa)	167.89

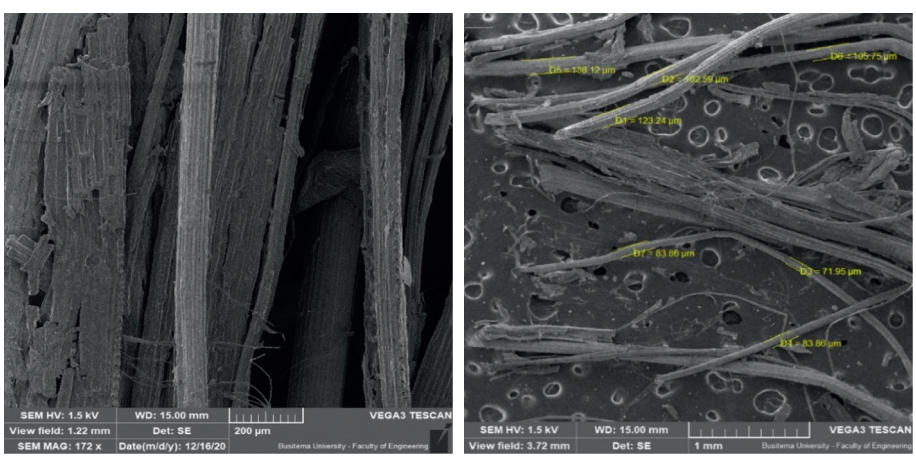

Figure 3: Images of banana fibre microstructure and diameter.

Microscopic morphology to determine general morphology was carried out on samples using a Variable Pressure Scanning Electron Microscope in accordance with ASTM standards [52, 53], and the test setup is shown in Figure 7. Also, Energy Dispersive X-ray Spectroscopy (EDS/XRD) to identify relative intensities at different diffraction angles within the composite was conducted on powdered samples in accordance with ASTM standards [53], and the test setup is shown in Figure 8.

3. Results and Discussion

3.1. Mechanical Properties. Mechanical properties of compressive, splitting tensile, and flexural strengths of Plain concrete (i.e. without fibres) and Banana Fibre-Reinforced Concrete (BFRC) mixes were determined, and the results are presented. For BFRC mixes, fibre lengths and contents were varied as follows: fibre lengths (40, 50, and 60 mm) and fibre contents (0.1, 0.2, 1.0, 1.5, and 2.5%).

Table 5: Mixture proportions.

Grade	Aggregates (mm)	W/C	Materials quantity (kg/m^3)			
			Water	Cement	Coarse aggregates	Fine aggregates
C20/25	19	0.45	192	444	1166	709

Table 6: Quantity of fibres for various mixes.

Fibre content (%)	0.0	0.1	0.25	1.0	1.5	2.5
Fibre quantity (kg/m^3)	0.0	0.44	1.11	4.44	6.66	11.1

Table 7: Concrete specimens prepared for testing.

Parameter	Plain concrete	BFRC	Dimension (mm)
Compressive strength	3	45*	150 × 150 × 150 mm cubes
Split tensile strength	3	45*	200Ø × 300 mm cylinders
Flexural strength	3	45*	100 × 100 × 350 mm beams

*5 (Fibre content) × 3 (Fibre length) × 3 (replicates) = 45 samples.

Figure 4: Compressive strength test setup.

3.1.1. Compressive Strength. Compressive strengths of Plain concrete ($f_{c(\text{Plain})}$) and BFRC ($f_{c(\text{BFRC})}$) as well as the compressive strength reinforced ratio ($f_{c(\text{BFRC})}/f_{c(\text{Plain})}$) at varying fibre lengths and contents are shown in Figure 9. It was clearly observed in Figure 9 that compressive strength values decreased with increasing fibre content at all fibre lengths. A similar behavior was observed in other previous studies conducted on fibre-reinforced concrete [54–56]. Xiong et al. [55] reported that compressive strength of concrete containing recycled carbon fibre-reinforced polymer (RCFRP) fibres decreased from 54.89 to 49.09 MPa when the fibre content was increased from 0.5 to 1.5%. A reduction in compressive strength is attributed to increase in porosity of the concrete matrix as a result of the addition of fibres, creating large contents of pores and microcracks at the matrix-fibre interface. Furthermore, reduction in compressive strength with increasing fibre content is likely to be associated with the effect of fibres on Interfacial Transition Zones (ITZs) and voids in concrete. It is expected that the more the amount of fibres, the more the ITZs will be created in concrete, which in turn negatively affects the compressive strength. Also, suggestions have been advanced that addition of fibres in concrete can restrict the lateral dilation instigated by Poisson effect when subjected to axial compression [57].

However, as shown in Figure 9(b), additional of fibres up to 0.25% resulted in higher compressive strength values in BFRC compared with Plain concrete, whereas an opposite trend was observed with fibre contents above 0.25%. Increase in compressive strength of BFRC in comparison with Plain concrete at increasing fibre content up to 0.25% was thought to result from the reinforcing action of fibres, which leads to the loads generated being shared between the fibres and concrete [2, 16]. Also, incorporation of banana fibres in concrete alters its failure mode from a brittle to plastic failure and hence mitigating the formation and propagation of cracks. Similar results were observed by other researchers who reported that fibres control microcrack formation and lead to the delay in failure and hence increasing the ultimate strength and strongly contribute in the load carrying capacity of the postpeak phase [58–60]. It has also been suggested that incorporating fibres in concrete enables it to resist extra compressive stress by blocking and redirecting the cracks [61]. Above 0.25% fibre content, the lower strength values of BFRC compared with Plain concrete can

(a) (b)

Figure 5: Splitting tensile strength testing. (a) Splitting tensile strength test setup. (b) Failure mode of concrete under splitting tension.

(a) (b)

Figure 6: Flexural strength testing. (a) Flexural strength test setup. (b) Failure mode of concrete under bending.

be attributed to the large quantity of fibres/excessive fibre content in the concrete having an adverse effect on compressive strength. Similar results were observed by other researchers [7, 9, 10, 34–36, 62–64] with Humphrey [7] noting that large quantity of fibres in the mortar produced voids and created nonuniform distribution within the composite, which led to reduced compressive strength.

In relation to fibre length, shorter fibres exhibited higher compressive strength values compared with longer fibres for BFRC containing fibre content over 0.25%. However, it should be noted that for all BFRC mixes with fibre content above 0.25%, only concrete containing shorter 40 mm fibres at 1% fibre content had higher compressive strength values compared with Plain concrete. This finding indicated that for optimal purposes, the banana fibre content should be limited to a maximum of 1% preferably using shorter fibres instead of longer ones. However, the effect of fibre length was not clear for BFRC containing fibre content up to 0.25% because longer 60 mm fibres showed marginally lower compressive strength values than shorter 40 mm fibres but distinctly higher values compared with shorter 50 mm fibres. The above clearly shows that for compressive strength of BFRC, the amount of fibres used is predominant compared with the fibre dimension/length when lower fibre contents are applied while the fibre dimension/length is predominant to the amount of fibres when higher fibre contents are applied.

3.1.2. Splitting Tensile Strength. Splitting tensile strengths of Plain concrete ($f_{t(\text{Plain})}$) and BFRC ($f_{t(\text{BFRC})}$) as well as the splitting tensile strength reinforced ratio ($f_{t(\text{BFRC})}/f_{t(\text{Plain})}$) at varying fibre lengths and contents are shown in Figure 10. It was generally observed in Figure 10 that increase in fibre content up to 1% resulted in increase in splitting tensile strength values of BFRC with the exception of concrete with 60 mm length that experienced a drop in strength when fibre content was increased from 0.25% to 1%. However, it was observed that beyond 1% of fibre content, all BFRC mixes exhibited a drop in strength values with increasing fibre content. A similar behavior of an initial increase in tensile strength up to a certain amount of fibre content and thereafter experiencing a drop with further increase in fibre content has been observed in another study [58]. Wu et al. [58] observed that for all fibres used (i.e. polypropylene, glass, and basalt fibres), splitting tensile strength of apricot shell concrete (ASC) significantly increased when the fibre content was increased from 0.25 to 0.50% but then dropped when the fibre content was increased from 0.5 to 0.75%. Increase in strength of BFRC up to 1% can be attributed to the bridging action of the fibres across the cracks inside the concrete matrix, which in turn inhibits crack propagation due to load sharing. Also, as already discussed, incorporation of banana fibres in concrete alters its failure mode from a brittle to plastic failure especially as the fibre content

(a) (b)

Figure 7: Microscopic morphology testing using a scanning electron microscope. (a) Variable SEM equipment. (b) Sample preparation for SEM.

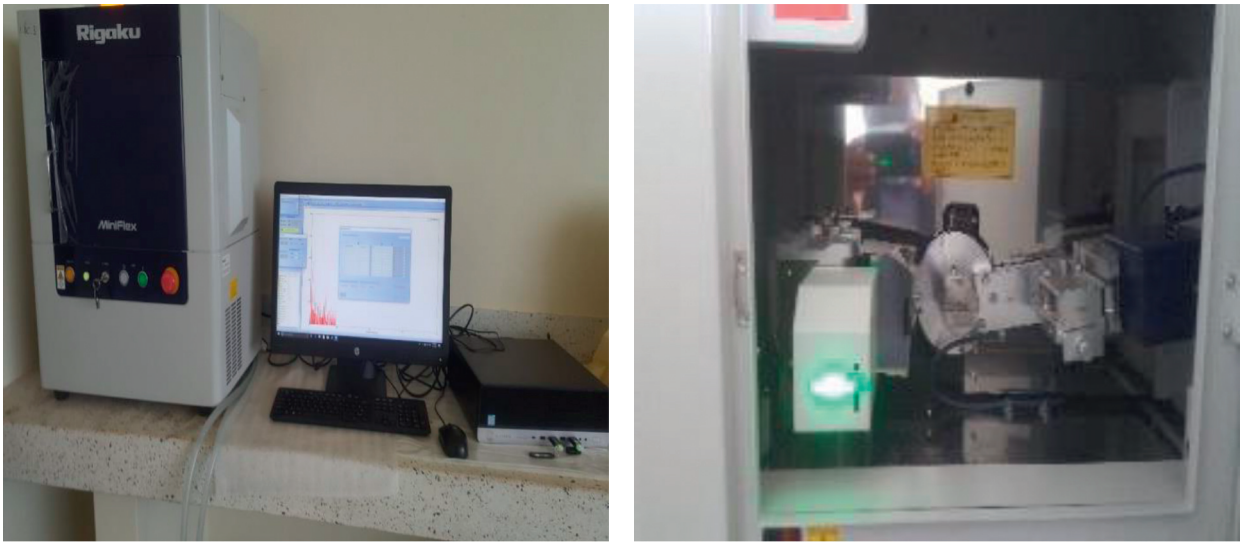

(a) (b)

Figure 8: Energy dispersive X-ray spectroscopy testing.

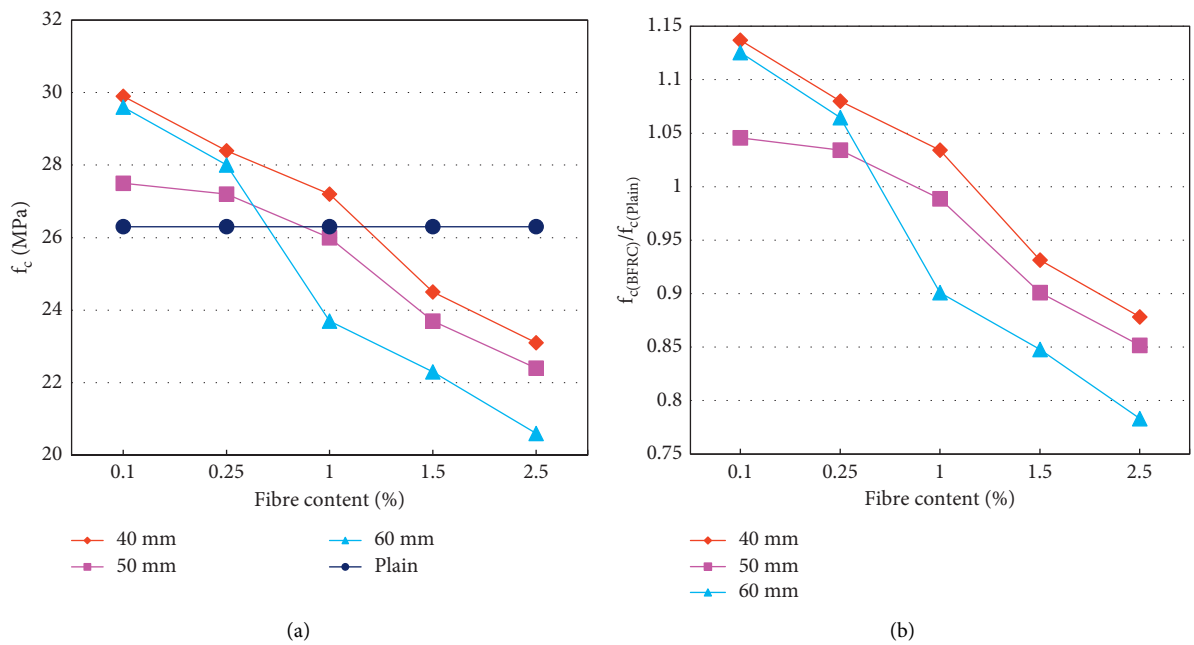

Figure 9: Effect of fibre length and fibre content on compressive strength of concrete. (a) Compressive strength. (b) Compressive strength reinforced ratio.

increases because fibres adequately inhibit the formation and propagation of cracks as well as limiting the confluence of cracks and adsorbing more destructive energy in the end [59]. Similar results were observed by other researchers who reported that addition of fibres had a significant improvement in tensile strength because they slowed down crack propagation, thereby enhancing mechanical strength of concrete [16, 58, 65, 66]. A drop in tensile strength of BFRC beyond 1% of fibre content can be attributed to excessive amount of fibre content in the concrete, which end up having an adverse effect on the strength of concrete as was similarly observed for compressive strength.

In relation to fibre length, BFRC having longer fibres exhibited higher tensile strength values compared with that having shorter fibres up to 1% of fibre content, except for BFRC having 60 mm length fibres at 1% fibre content. A similar effect of fibre length was observed when comparing plain and BFRC up to 1% fibre content. As shown in Figure 10(b), BFRC with longer fibre lengths of 60 and 50 mm exhibited better performance in comparison with Plain concrete, whereas strength values of BFRC with 40 mm length fibres were lower than those of Plain concrete. Longer fibres are expected to have contributed more in the mitigation of the pull-out effect of fibres compared with shorter fibres, thus preventing cracking and crack propagation [67]. The above phenomenon is therefore responsible for BFRC having longer fibres showing higher tensile strength values compared with that having shorter fibres up to 1% of fibre content.

However, although tensile strength was decreasing with increasing fibre content for all BFRC mixes containing fibre content above 1%, BFRC with shorter fibres exhibited higher tensile strength values compared with that containing longer fibres. This could be related to the cumulative amount of fibres in concrete, with longer fibres resulting in excessive amount of fibres at higher fibre dosage, which significantly diminish its performance due to the fibre curling and clustering. Furthermore, longer fibres are known to result in difficulty of dispersion of fibres during the mixing process [34]. Nonetheless, all BFRC mixes with fibre content above 1% exhibited lower strength values in comparison with Plain concrete. The above clearly shows that for tensile strength of BFRC, longer fibres performed better than shorter fibres up to 1% fibre content, with an opposite trend noticed above 1% fibre content. This phenomenon is more pronounced at the extreme ends of fibre dosage (i.e. 0.1% and 2.5%).

3.1.3. Flexural Strength. Flexural strengths of Plain concrete ($f_{f(\text{Plain})}$) and BFRC ($f_{f(\text{BFRC})}$) as well as the flexural strength reinforced ratio ($f_{f(\text{BFRC})}/f_{f(\text{Plain})}$) at varying fibre lengths and contents are shown in Figure 11. It was generally observed in Figure 11 that except for BFRC containing 40 mm length fibres at a dosage of 0.25%, flexural strengths of all BFRC mixes were lower in comparison to Plain concrete. The above observation indicated that addition of banana fibres generally does not greatly contribute to flexural strength of concrete but only has marginal impact when shorter fibres are used at lower fibre dosage. Similar results were observed by other researchers who reported that when compared with Plain concrete, addition of fibres had no significant impact on the flexural strength and stiffness of fibre-reinforced concrete [20, 68, 69]. This insignificant impact on flexural strength of BFRC could be attributed to banana fibres not providing the composite structure with a better capacity to resist high flexural deformations because of the loss of homogeneity and increased porosity caused by fibre addition. However, the general trend indicated that flexural

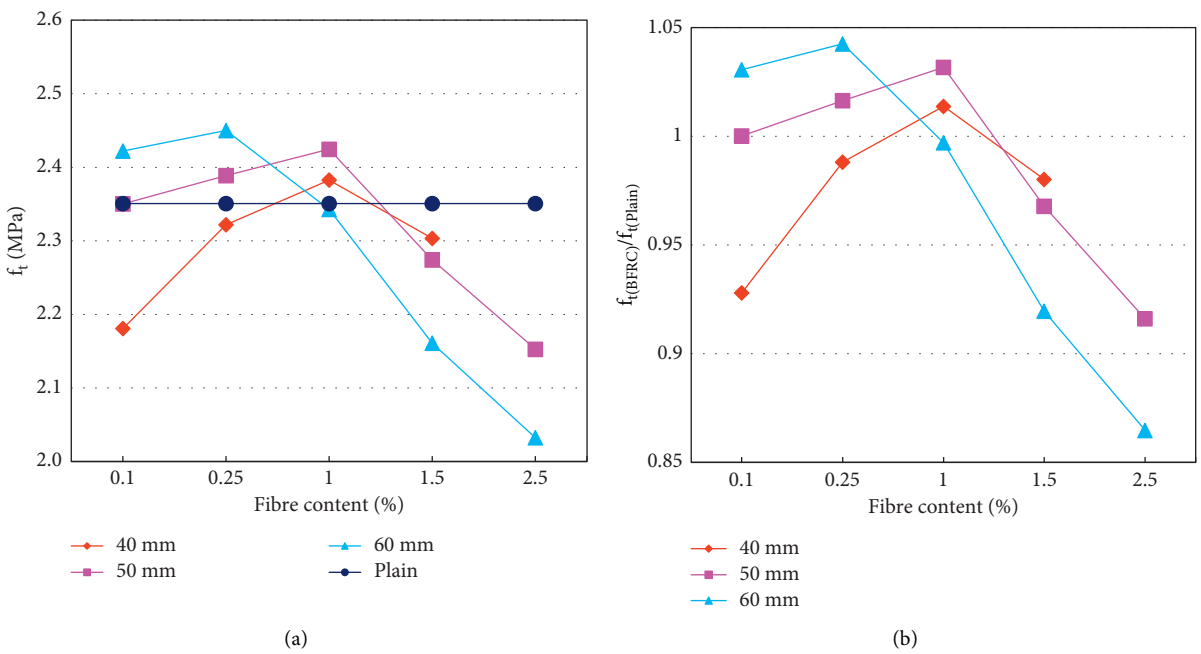

Figure 10: Effect of fibre length and fibre content on split tensile strength of concrete. (a) Splitting tensile strength. (b) Splitting tensile strength reinforced ratio.

strength of BFRC containing shorter fibres increased and peaked at a fibre content ranging between 0.25% and 1.0% before dropping with increasing fibre content. Contrastingly, the flexural strength of all BFRC mixes containing longer fibres decreased with increasing fibre content. This is similar to the results for splitting tensile strength of BFRC containing longer fibres at high-fibre dosage and is related to the difficulty of dispersion of longer fibres during the mixing process [34].

The above observed insignificant impact of banana fibres on flexural strength of BFRC is a critical disadvantage for their practical application in the construction industry in relation to the service deflection limits provided for in most technical specifications and codes of practice. Therefore, more research on how to improve the flexural strength of BFRC to meet the minimum technical requirements is paramount before banana fibres can be considered for structural applications in construction industry.

3.2. Microstructural Properties

3.2.1. Concrete Morphology under SEM. Concrete morphology was aimed at understanding the effect of the fibres on the interfacial transition zones (ITZs), microcracks, and their propagation in the matrix between fibre-cement paste and aggregate-cement paste. Microscopic morphology of Plain concrete and BFRC samples observed using SEM is shown in Figures 12 and 13, respectively. As shown in Figure 12, it was observed that Plain concrete exhibited a porous morphology with varying sizes, had normal setting, and the ITZ was identified between bulk paste-aggregate composite of approximately 50 μm [37], even though it was not clear. High porosity observed can be attributed to initial water absorption, which affected the rate of hydration. The above findings are similar to those from another study [43]. However, BFRC exhibited larger rectangular voids or pores within the matrix with clearly defined boundaries as shown in Figure 13. Furthermore, a clear ITZ was observed between fibres and paste ranging between 3.23 and 5.89 μm, and the fibres could be readily identified.

Furthermore, microcracks were observed within the composite of Plain concrete compared with BFRC, where no clear microcracks were observed. This could be attributed to the addition of the fibres, which alleviated bridged against the formation of the microcracks and prevented them from further propagation. This is consistent with results for the mechanical properties of compressive, splitting tensile, and flexural strengths of the concrete mixes already discussed. Furthermore, the fibres were observed to be surrounded by cement paste, which also has a bearing on improving the matrix strength resulting from a stress transfer mechanism between the matrix and reinforced fibres. This coupled with its resistance against tensile stresses generated by applied loads helped to maintain the microstructure intact by resisting crack propagation. Therefore, it can be concluded that the incorporation of fibres improved the microstructure of concrete through better bonding between the fibres and the matrix as well as a reduction in the size of ITZ and consequently the porosity of the matrix by filling its pores, which ultimately resulted in improved mechanical properties of the composite as observed from the test results.

3.2.2. Energy Dispersive X-Ray Spectroscopy (EDS/XRD). Energy Dispersive X-ray Spectroscopy (EDS/XRD) was used to characterize samples prepared from Plain concrete and BFRC. Data were collected in the 2θ range between 3° and 80°

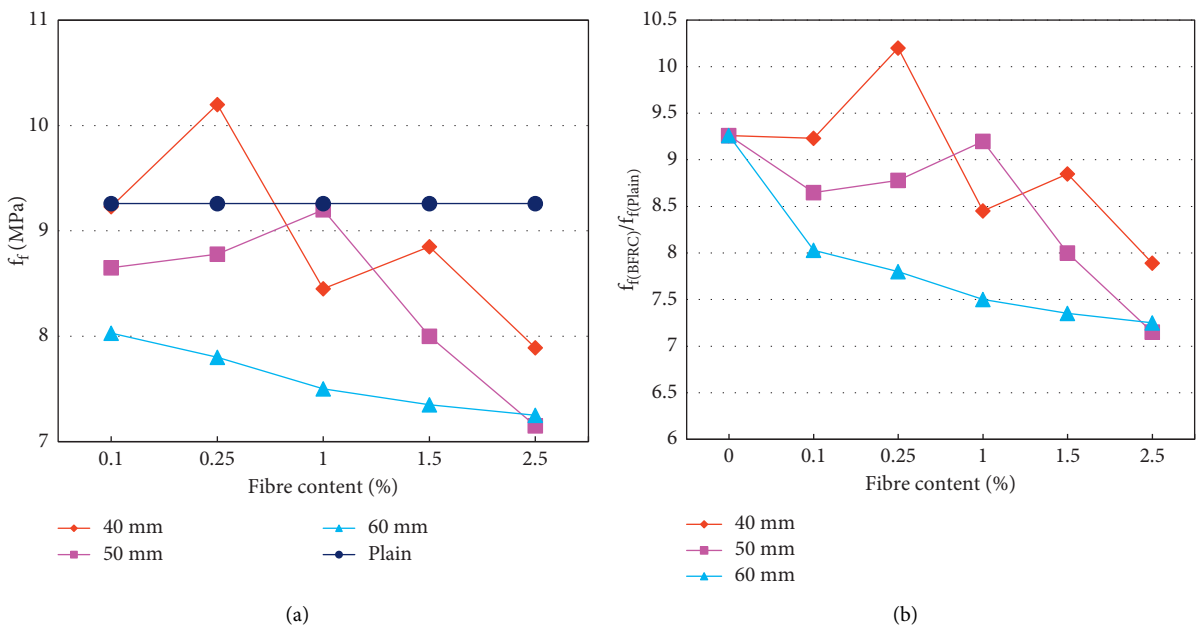

Figure 11: Effect of fibre length and fibre content on flexural strength of concrete. (a) Flexural strength. (b) Flexural strength reinforced ratio.

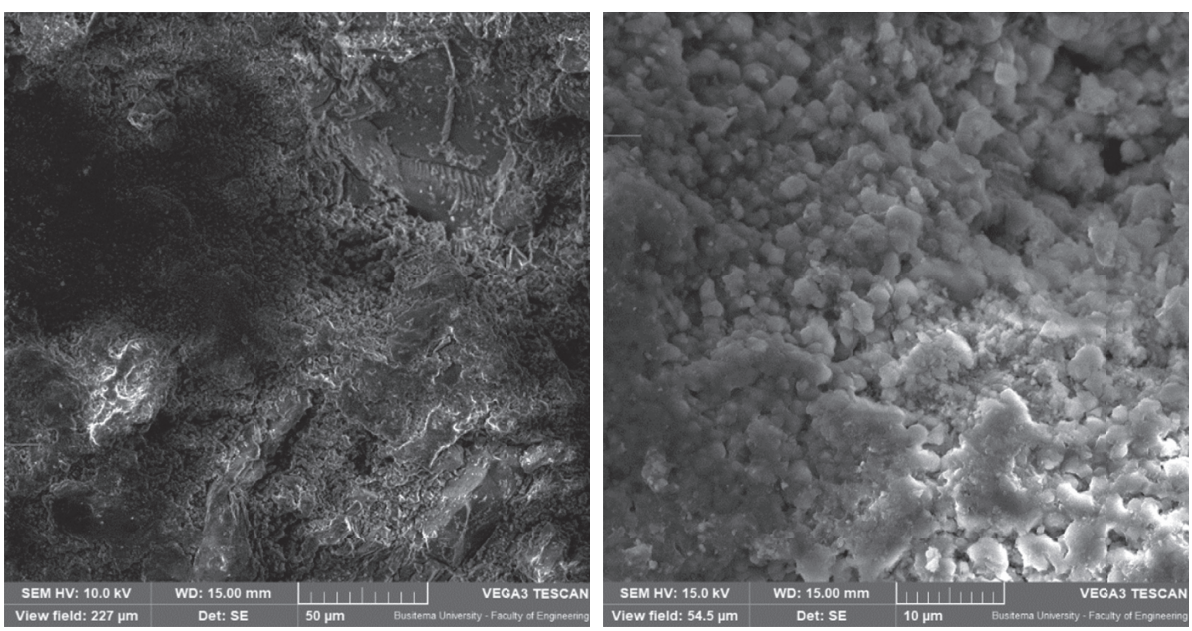

Figure 12: SEM morphology for plain concrete.

with a step size of 0.02° and a counting time of 0.06 sec./step. The XRD characteristic patterns of Plain concrete and BFRC samples at different diffraction angles and intensities that appear as peaks are shown in Figures 14 and 15 , respectively. It was observed that both Plain concrete and BFRC exhibited different peaks at different diffraction angles combined with sharp peaks, and higher characteristic peaks were achieved at 2θ range between 3° and 6° for both Plain concrete and BFRC as shown in Figures 14(b) and 15(b), respectively. As shown in Figure 14, the maximum characteristic peak intensity for Plain concrete was 13 counts occurring at a diffraction angle (2θ) of 4.28 with other similar corresponding peaks as follows: (3.04, 12.00), (3.14, 12.00), (3.28, 11.00), (3.68, 10.00), and (4.14, 9.00). For BFRC as shown in Figure 15, the maximum characteristic peak intensity observed was higher than that of Plain concrete at 25 counts occurring at an angle (2θ) of 3.04 with other similar corresponding peaks as follows: (3.00, 12.00), (3.06, 18.00), (3.16, 12.00), (3.28, 17.00), (3.82, 15.00), (3.94, 14.00), (4.26, 9.00), (4.42, 17.00), (5.72, 7.00), and (5.74, 10.00). Therefore, the patterns

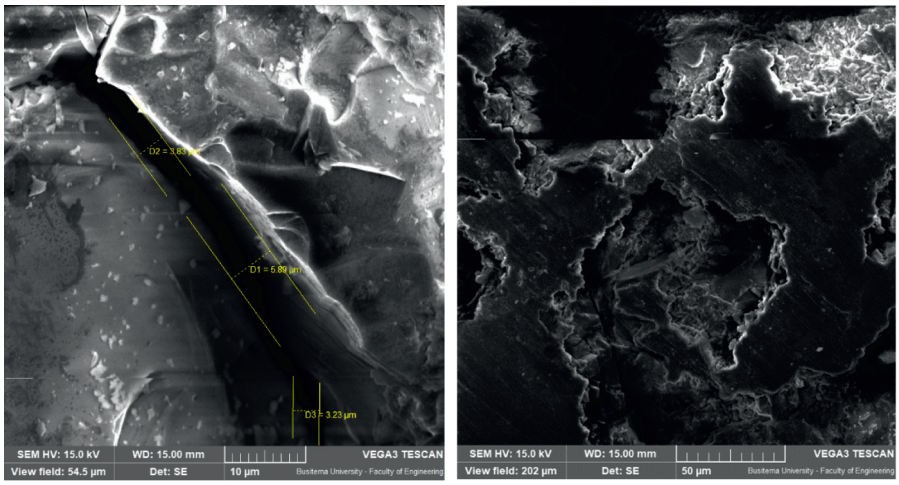

Figure 13: SEM morphology for banana fibre-reinforced concrete (BFRC).

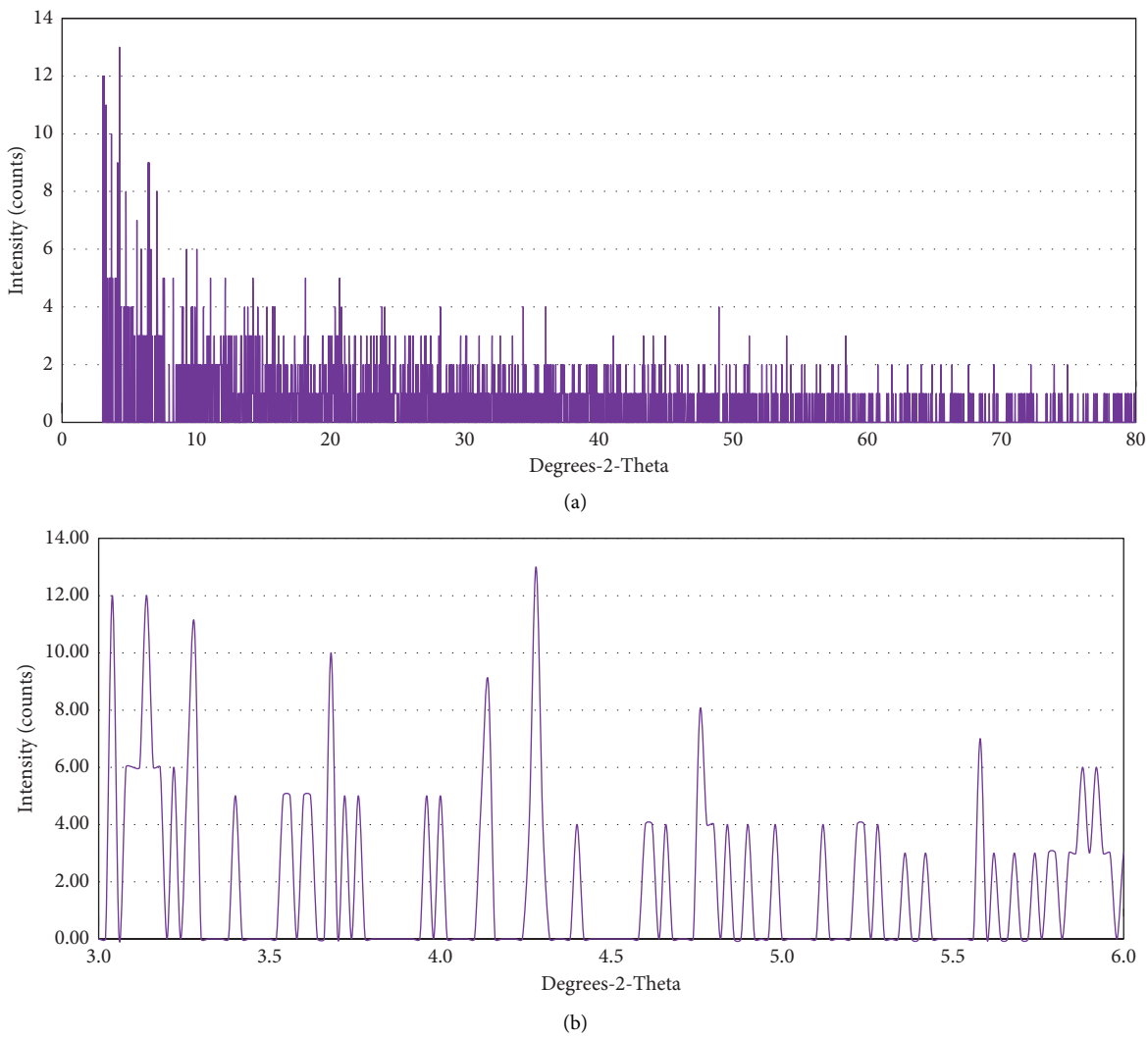

Figure 14: XRD micrographs for plain concrete. (a) Characteristic patterns in the 2θ range between 3° and 80°. (b) Higher characteristic peaks in the 2θ range between 3° and 6°.

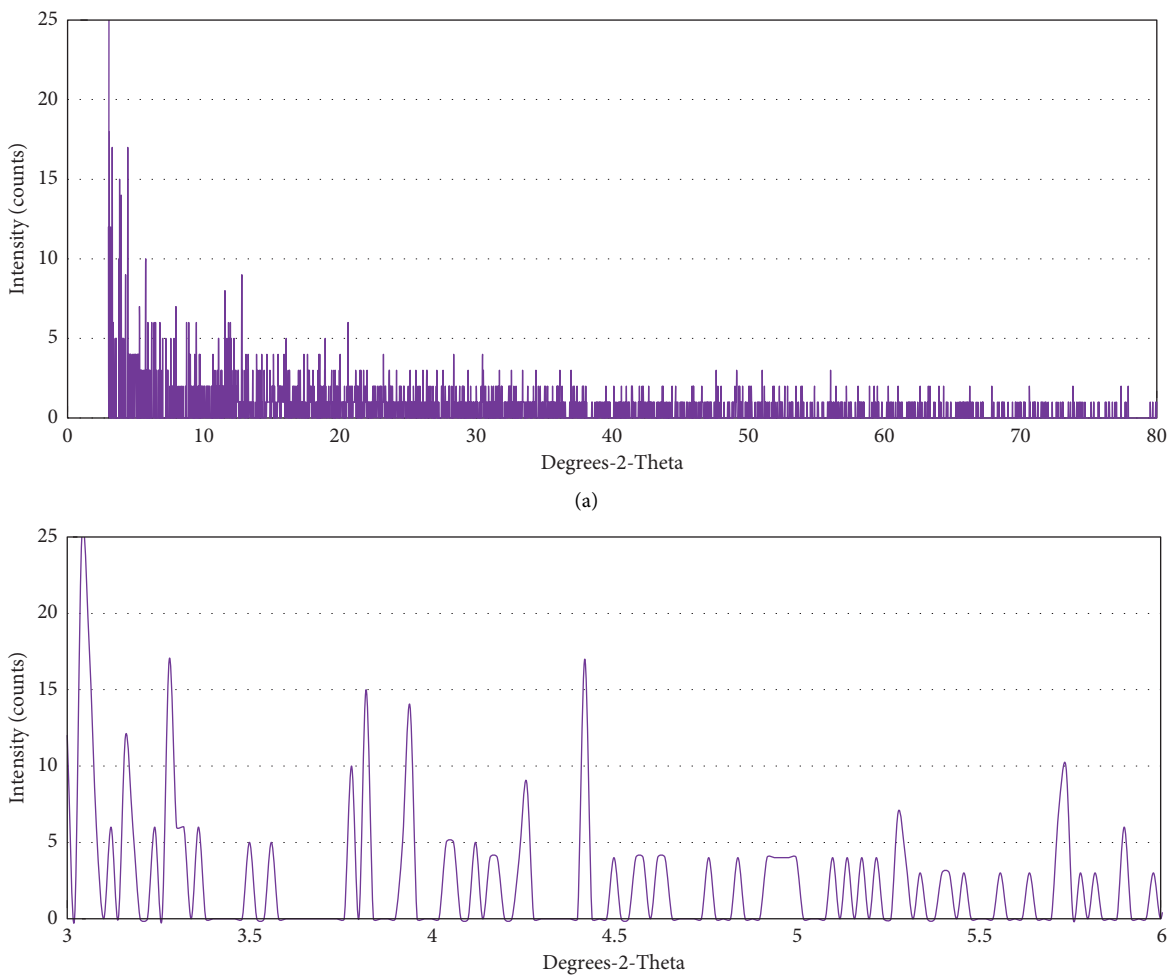

Figure 15: XRD micrographs for BFRC. (a) Characteristic patterns in the 2θ range between 3° and 80°. (b) Higher characteristic peaks in the 2θ range between 3° and 6°.

displayed for BFRC are greater in intensity than those for Plain concrete. It was further observed that there were variations in the shape of the peak intensities that were obtained. The higher peak intensities at a lower position (angle) indicated maximum interplanar spacing within the crystal structure, with the highest peaks for Plain concrete and BFRC having interplanar spacing (d) calculated as 206 Å and 29 Å, respectively, while the calculated lattice constant was 357 Å, and 50 Å meters, respectively. This indicated that the fibres contributed to changes in phases of the composite structure of the BFRC because the incorporation of fibres resulted in a reduction in the interplanar spacing and lattice structure of concrete.

4. Conclusions

This experimental study aimed at investigating the impact of addition of banana fibres on the mechanical and microstructural properties of concrete. Concrete mixes comprising banana fibres of varying fibre lengths (40, 50, and 60 mm) and fibre contents (0.1, 0.2, 1.0, 1.5, and 2.5%) were assessed against mechanical (compression, splitting tension, and flexure) and microstructural (microscopic morphology and Energy Dispersive X-ray Spectroscopy) properties. Based on the analysis carried out, the following conclusions can be drawn.

(1) Addition of banana fibres to concrete only significantly imparts on compressive strength at lower fibre contents of up to 0.25% for all fibre lengths because higher compressive strength was observed in BFRC compared with Plain concrete. However, there is no significant impact of fibre length on compressive strength at lower fibre contents of up to 0.25%. Impact of fibre length only becomes more pronounced at higher dosages above 0.25%, where BFRC with shorter fibre length perform better than that with longer ones.

(2) Increase fibre content only positively imparts on tensile strength of concrete at relatively lower fibre dosages of

up to 1%. Similarly, a significant impact of fibre length on tensile strength of concrete was observed at lower fibre contents of up to 1% with longer fibres noticed to be more effective compared with shorter ones, whereas an opposite trend was noticed above 1% fibre content. This phenomenon is more pronounced at the extreme ends of fibre dosages (i.e. 0.1% and 2.5%).

(3) Addition of banana fibres generally did not greatly contribute to flexural strength of concrete but had a marginal impact only when shorter fibres were used at lower fibre dosages. Contrastingly, the flexural strength of all BFRC mixes containing longer fibres decreased with increasing fibre content.

(4) Incorporation of banana fibres in concrete improved its microstructure through better bonding between the fibres and the matrix as well as a reduction in the size of ITZ and consequently the porosity of the matrix by filling its pores, which ultimately resulted in improved mechanical properties of the composite.

(5) Banana fibres contributed to changes in phases of the composite structure of the BFRC because their incorporation resulted in a reduction in the interplanar spacing and lattice structure of BFRC.

(6) For optimal purposes, addition of banana fibres should be limited to a maximum of 1% fibre content preferably using shorter fibres instead of longer ones. Further research on how to improve the flexural strength of BFRC to meet the minimum technical requirements is required before banana fibres can be considered for structural applications in construction industry.

Data Availability

The data used to support the findings of this study are included within the article.

Conflicts of Interest

The author declares that there is no conflict of interest regarding the publication of this paper.

Acknowledgments

The authors acknowledge that this study was partly based on a study by Adolph Karubanga under the supervision of Rodgers B Mugume and Michael Kyakula. The authors acknowledge the laboratories at Busitema University and Makerere University whose staff and facilities were used to carry out some of the tests. Their assistance throughout this study is greatly appreciated.

References

[1] L. Zhang, J. Zhao, C. Fan, and Z. Wang, "Effect of surface shape and content of steel fiber on mechanical properties of concrete," *Advances in Civil Engineering*, vol. 2020, Article ID 8834507, 11 pages, 2020.

[2] P. Zhang, H. Song, N. Serina, and H. Xu, "Fiber-reinforced concrete with application in civil eng," *Advances in Civil Engineering*, vol. 2018, Article ID 1698905, 4 pages, 2018.

[3] K. Ravi, C. Selin, and V. Ramasamy, "Effect of fibers in concrete composites," *International Journal of Applied Engineering Research*, vol. 10, no. 0973-4562, pp. 419–430, 2015.

[4] P. Zhang, S. Fu, K. Zhang, and T. Zhang, "Mechanical properties of polyvinyl alcohol fiber-reinforced concrete composite containing fly ash and nano-SiO2," *Science of Advanced Materials*, vol. 10, no. 6, pp. 769–778, 2018.

[5] A. S. Sayyad and S. V. Patankar, "Effect of steel fibres and low calcium fly ash on mechanical and elastic properties of geopolymer concrete composites," *Indian Journal of Materials Science*, vol. 2013, Article ID 357563, 8 pages, 2013.

[6] Aci 207.2R-95, *Effect of Restraint, Volume Change, and Reinforcement on Cracking of Mass Concrete*, American Concrete Institute, Farmington Hills, MichiganMI, USA, 2002.

[7] D. Humphrey, "Influence of plantain pseudostem fibres and lime on the properties of cement mortar," *Advances in Materials Science and Engineering*, vol. 2020, Article ID 4698603, 9 pages, 2020.

[8] A. Tehmina, S. Nasir, and M. F. Nuruddin, "Effect of chopped basalt fibers on the mechanical properties and microstructure of high performance fiber reinforced concrete," *Advances in Materials Science and Engineering*, vol. 2014, Article ID 587686, 14 pages, 2014.

[9] K. Chandramouli, N. Pannirselvam, D. V. NagaSaiPardhu, and V. Anitha, "Experimental investigation on banana fibre reinforced concrete with conventional concrete," *International Journal of recent Technology and Engineering*, vol. 7, no. 6S, 2019.

[10] A. Dhawan, N. Gupta, R. Goyal, and K. K. Saxena, "Evaluation of mechanical properties of concrete manufactured with fly ash, bagasse ash and banana fibre," *Materials Today*, vol. 44, 2020.

[11] A. M. Neville, *Properties of Concrete*, Pearson Education Limited, Edinburgh, UK, 5th edition, 2011.

[12] Aci 224R-01, *Control of Cracking in Concrete Structures*, American Concrete Institute, Farmington Hills, MI, USA, 2001.

[13] S. Mukhopadhyay and R. Fangueiro, "Physical modification of natural fibers and thermoplastic films for composites - a review," *Journal of Thermoplastic Composite Materials*, vol. 22, no. 2, pp. 135–162, 2009.

[14] Z. Li, X. Wang, and L. Wang, "Properties of hemp fibre reinforced concrete composites," *Composites Part A: Applied Science and Manufacturing*, vol. 37, no. 3, pp. 497–505, 2006.

[15] P. K. Mallick, *Fiber Reinforced Composites- Materials Manufacturing and Design*, Taylor & Francis Group, London, UK, 3rd edition, 2008.

[16] B. Mobasher, *Mechanics of Fiber and Textile Reinforced Cement Composites*, CRC Press- Taylor & Francis group, London, UK, 2012.

[17] M. Chandrasekar, M. R. Ishak, S. M. Sapuan, Z. Leman, and M. Jawaid, "A review on the characterisation of natural fibres and their composites after alkali treatment and water absorption," *Plastics, Rubber and Composites*, vol. 46, no. 3, pp. 119–136, 2017.

[18] B. Koohestani, A. K. Darban, P. Mokhtari, E. Yilmaz, and E. Darezereshki, "Comparison of different natural fiber treatments: a literature review," *International journal of Environmental Science and Technology*, vol. 16, no. 1, pp. 629–642, 2019.

[19] R. Ahmad, R. Hamid, and S. Osman, "Physical and chemical modifications of plant fibers for reinforcement in cementitious composites," *Advances in Civil Engineering*, vol. 2019, Article ID 5185806, 18 pages, 2019.

[20] A. Elbhiery, O. Elnawawya, M. Kassemb, A. Zahera, N. Uddinc, and M. Mostafac, "Performance of concrete beams reinforced using banana fiber bars," *Case Studies in Construction Materials*, vol. 13, pp. 1–13, 2020.

[21] X. Xiong, S. Z. Shen, L. Hua et al., "Finite element models of natural fibers and their composites: a review," *Journal of Reinforced Plastics and Composites*, vol. 37, no. 9, pp. 617–635, 2018.

[22] K. Liu, H. Takagi, and Z. Yang, "Evaluation of transverse thermal conductivity of Manila hemp fiber in solid region using theoretical method and finite element method," *Materials & Design*, vol. 32, no. 8-9, pp. 4586–4589, 2011.

[23] H. Wang, Y.-P. Lei, J.-S. Wang, Q.-H. Qin, and Y. Xiao, "Theoretical and computational modeling of clustering effect on effective thermal conductivity of cement composites filled with natural hemp fibers," *Journal of Composite Materials*, vol. 50, no. 11, pp. 1509–1521, 2015.

[24] H. Wang, Q.-H. Qin, and Y. Xiao, "Special n -sided Voronoi fiber/matrix elements for clustering thermal effect in natural-hemp-fiber-filled cement composites," *International Journal of Heat and Mass Transfer*, vol. 92, pp. 228–235, 2016.

[25] F. T. Wallenberger and W. E. Norman, *Natural Fibers, Plastics and Composites*, Springer Science and Business media, LLC, New York, NY, USA, 2nd edition, 2004.

[26] A. K. Mohanty, M. Misra, and L. T. Drzal, *Natural Fiber–Rubber Composites and Their Applications*, Taylor & Francis, London, UK, 1st edition, 2005.

[27] D. B. Klemm, P. T. Heinze, U. Heinze, and W. Wagenknecht, *Comprehensive Cellulose Chemistry; Volume 1: Fundamentals and Analytical Methods*, Wiley VCH, Weinheim, Germany, 1st edition, 1999.

[28] H. E. Gram, *Durability of Natural Fibers in Concrete*, Swedish Cement and Concrete Research Institute, Stockholm, Sweden, 1983.

[29] A. M. M. Edeerozey, H. M. Akil, A. B. Azhar, and M. I. Z. Ariffin, "Chemical Modification of kenaf fibers," *Materials Letters*, vol. 61, no. 10, pp. 2023–2025, 2007.

[30] P.-C. Aitcin and S. Mindess, *Sustainability of Concrete*, Taylor & Francis e-Library, London, UK, 1st edition, 2011.

[31] T. Y. Girijappa, M. S. Rangappa, J. Parameswaranpillai, and S. Siengchin, "Natural fibers as sustainable and renewable resource for development of eco-friendly composites: a comprehensive review: 10.3389/fmats.2019.00226," *Polymeric and Composite Materials*, vol. 6, no. 226, p. 14, 2019.

[32] H. Savastano, P. G. Warden, and R. S. P. Coutts, "Brazilian waste fibres as reinforcement for cement-based composites," *Cement and Concrete Composites*, vol. 22, no. 5, pp. 379–384, 2000.

[33] J. A. O. Barros, F. D. A. Silva, and R. D. Toledo Filho, "Experimental and numerical research on the potentialities of layered reinforcement configuration of continuous sisal fibers for thin mortar panels," *Construction and Building Materials*, vol. 102, no. 1, pp. 792–801, 2016.

[34] S. Mukhopadhyay and B. Bhattacharjee, "Influence of fibre dispersion on compression strength of banana fibres reinforced concrete," *Journal of Industrial Textiles*, vol. 45, no. 5, pp. 957–964, 2016.

[35] D. Prasannan, S. Nivin, K. R. Raj, S. Giridharan, and M. Elavivekan, "Comparative study of banana and sisal fibre reinforced concrete with conventional concrete," *International Journal of Pure and Applied Mathematics*, vol. 118, no. 20, pp. 1757–1765, 2018.

[36] K. J. Ellen, M. R. Mondoringin, and H. Manalip, "Basic behaviour of natural banana stem fiber reinforced concrete under uniaxial and biaxial tensile stress," *International Journal of GEOMATE*, vol. 14, no. 44, pp. 166–175, 2018.

[37] K. P. Mehta and P. J. M. Monteiro, *Concrete: Microstructure, Properties and Materials*, McGraw-Hill, London, UK, 3rd edition, 2006.

[38] D. Brandon and W. D. Kaplan, *Microstructural Characterization of Materials*, John Wiley & Sons, Chichester, West Sussex, UK, 2nd edition, 2008.

[39] A. Bentur and S. Mindess, *Fibre Reinforced Cementitious Composites*, Taylor & Francis, London, UK, 2nd edition, 2007.

[40] K. M. Nemati and P. Stroeven, "Stereological analysis of micromechanical behavior of concrete," *Materials and Structures*, vol. 34, no. 8, pp. 486–494, 2001.

[41] J. I. Goldstein, D. E. Newbary, J. R. Michael, N. W. Ritchie, J. H. Scott, and D. C. Joy, *Scanning Electron Microscopy and X-Ray Microanalysis*, Springer, New York, NY, USA, 2018.

[42] H. Savastano Jr, P. G. Warden, and R. S. P. Coutts, "Microstructure and mechanical properties of waste fibre-cement composites," *Cement and Concrete Composites*, vol. 27, no. 5, pp. 583–592, 2005.

[43] M. Sivaraja, Kandasamy, N. Velmani, and M. S. Pillai, "Study on durability of natural fibre concrete composites using mechanical strength and microstructural properties," *Bulletin of Materials Science*, vol. 33, no. 6, pp. 719–729, 2010.

[44] Astm C150/C150M - 20, *Standard Specification for Portland Cement*, ASTM International, West Conshohocken, PA, USA, 2020.

[45] Astm C33/C33M-18, *Standard Specification for Concrete Aggregates*, ASTM International, West Conshohocken, PA, USA, 2018.

[46] K. L. Pickering, M. G. A. Efendy, and T. M. Le, "A review of recent developments in natural fibre composites and their mechanical performance," *Composites Part A: Applied Science and Manufacturing*, vol. 83, no. 83, pp. 98–112, 2016.

[47] Aci 211.1-91, *Standard Practice for Selecting Proportions for Normal, Heavyweight, and Mass Concrete*, American Concrete Institute, Farmington Hills, MI, USA, 2002.

[48] Aci 544.1R-96, *Report on Fiber Reinforced Concrete*, American Concrete Institute, Farmington Hills, MI, USA, 2002.

[49] Bs En 12390-3, *Testing Hardened concrete. Compressive Strength of Test Specimens*, British Standard Institution, London, UK, 2009.

[50] Astm C496/C496M–17, *Standard Test Method for Splitting Tensile Strength of Cylindrical Concrete Specimens*, ASTM International, West Conshohocken, PA, USA, 2017.

[51] Astm C293/C293M-16, *Standard Test Method for Flexural Strength of Concrete (Using Simple Beam with Center-Point Loading*, ASTM International, West Conshohocken, PA, USA, 2016.

[52] Astm- C856-95, *Standard Practice for Petrographic Examination of Hardened Concrete*, ASTM International, West Conshohocken, PA, USA, 1998.

[53] Astm C1723-16, *Standard Guide for Examination of Hardened Concrete Using Scanning Electron Microscopy*, ASTM International, West Conshohocken, PA, USA, 2016.

[54] S. T. Tassew and A. S. Lubell, "Mechanical properties of glass fiber reinforced ceramic concrete," *Construction and Building Materials*, vol. 51, pp. 215–224, 2014.

[55] C. Xiong, T. Lan, Q. Li, H. Li, and W. Long, "Study of mechanical properties of an eco-friendly concrete containing

recycled carbon fiber reinforced polymer and recycled aggregate," *Materials*, vol. 13, no. 20, p. 4592, 2020.

[56] M. Mastali, A. Dalvand, and A. Sattarifard, "The impact resistance and mechanical properties of the reinforced self-compacting concrete incorporating recycled CFRP fiber with different lengths and dosages," *Composites Part B: Engineering*, vol. 112, pp. 74–92, 2017.

[57] B. Han and T.-Y. Xiang, "Axial compressive stress-strain relation and Poisson effect of structural lightweight aggregate concrete," *Construction and Building Materials*, vol. 146, pp. 338–343, 2017.

[58] F. Wu, Q. Yu, C. Liu, H. J. H. Brouwers, L. Wang, and D. Liu, "Effect of fibre type and content on performance of bio-based concrete containing heat-treated apricot shell," *Materials and Structures*, vol. 53, no. 6, p. 137, 2020.

[59] M. Khan and M. Cao, "Effect of hybrid basalt fiber length and content on properties of cementitious composites," *Magazine of Concrete Research*, vol. 73, no. 10, pp. 1–42, 2019.

[60] T. Plagué, C. Desmettre, and J.-P. Charron, "Influence of fiber type and fiber orientation on cracking and permeability of reinforced concrete under tensile loading," *Cement and Concrete Research*, vol. 94, pp. 59–70, 2017.

[61] P. S. Song, S. Hwang, and B. C. Sheu, "Strength properties of nylon- and polypropylene-fiber-reinforced concretes," *Cement and Concrete Research*, vol. 35, no. 8, pp. 1546–1550, 2005.

[62] C. X. Qian and P. Stroeven, "Development of hybrid polypropylene-steel fibre-reinforced concrete," *Cement and Concrete Research*, vol. 30, no. 1, pp. 63–69, 2000.

[63] J. Gao, W. Sun, and K. Morino, "Mechanical properties of steel fiber-reinforced, high-strength, lightweight concrete," *Cement and Concrete Composites*, vol. 19, no. 4, pp. 307–313, 1997.

[64] C. Scheffler, S. L. Gao, R. Plonka et al., "Interphase modification of alkali-resistant glass fibres and carbon fibres for textile reinforced concrete II: water adsorption and composite interphases," *Composites Science and Technology*, vol. 69, pp. 905–912, 2009.

[65] Y. V. Lipatov, S. I. Gutnikov, M. S. Manylov, E. S. Zhukovskaya, and B. I. Lazoryak, "High alkali-resistant basalt fiber for reinforcing concrete," *Materials & Design*, vol. 73, pp. 60–66, 2015.

[66] B. Wei, H. Cao, and S. Song, "Degradation of basalt fibre and glass fibre/epoxy resin composites in seawater," *Corrosion Science*, vol. 53, no. 1, pp. 426–431, 2011.

[67] R. F. Zollo, "Fiber-reinforced concrete: an overview after 30 years of development," *Cement and Concrete Composites*, Elsevier Science ltd, vol. 19, no. 2, pp. 107–122, 1997.

[68] L. Bei-xing, C. Ming-xiang, C. Fang, and L. Lu-ping, "The mechanical properties of polypropylene fiber reinforced concrete," *Journal of Wuhan University of Technology-Materials Science Edition*, vol. 19, no. 3, pp. 68–71, 2004.

[69] A. M. Alhozaimy, P. Soroushiad, and F. Mirza, "Mechanical properties of polypropylene fiber reinforced concrete and the effects of pozzolanic materials," *Cement and Concrete Composites*, vol. 18, 1996.

Hindawi
Advances in Civil Engineering
Volume 2021, Article ID 6839627, 13 pages
https://doi.org/10.1155/2021/6839627

Research Article

From Topology Optimization to Complex Digital Architecture: A New Methodology for Architectural Morphology Generation

Kangqiang Lin,[1] Yongpeng He,[2] Yang Yang,[3] and Lei Xiong[1]

[1]*School of Architecture and Applied Art, Guangzhou Academy of Fine Arts, Guangzhou 511400, China*
[2]*Department of Architecture and Civil Engineering, University of Bath, Bath BA1 3BZ, UK*
[3]*Department of Civil Engineering and Transportation, South China University of Technology, Guangzhou, China*

Correspondence should be addressed to Lei Xiong; kmt20005@gmail.com

Received 9 May 2021; Accepted 13 July 2021; Published 5 October 2021

Academic Editor: Rahul V. Ralegaonkar

Owing to the capacities of generating structural configuration with both reasonable mechanical properties and high material utilization, topology optimization has been widely adopted in engineering design. Although numerous architects have tried to apply topology optimization tools to assist architectural morphology design in practical projects, topology optimization, like other quantitative analysis techniques, has not been systematically incorporated into the architectural morphology design. In this study, by integrating topology optimization toolsets and parametric design theory, combined with multiattribute decision-making analysis, a design method is proposed that could efficiently obtain several architectural structural architectural morphologies with both structural rationality and aesthetic rules and complete the evaluation and performance ranking of alternatives. In this study, the essential architectural application scenarios are divided into surface application scenarios and volumetric application scenarios, and the possible variation range of topology optimization parameters of architectural application scenarios is defined. By iteratively adjusting the influence parameters, diverse results of structural morphology are obtained. It is found that small changes in optimization parameters will bring great differences in topological results. Such a sensitive relationship can be utilized to generate a set of rational topological structures, and these topological results can be regarded as alternatives for architectural morphology design. For the performance evaluation and ranking analysis of alternatives, the application of FANP-TOPSIS multiattribute decision-making model is put forward in this study. The case study shows that this decision-making analysis model is efficient, convenient, and applicable in the architectural morphology design. The results of this study can provide new ideas and key references for scholars and architects in the field of architecture to explore the process and method of architectural morphology design and other related issues.

1. Introduction

Developments in construction industry design software and the maturity of related manufacturing techniques over the past two decades have led to the construction of buildings with complex and eye-catching appearance [1]. Whilst many have received praise and are considered to be iconic landmarks for their region, others are criticized for the lack of harmony between their architectural design and structural considerations. The challenge therefore remains to obtain satisfying designs that can simultaneously embrace architectural operational functions and aesthetic appealing effects, as well as maintaining rational structural performance [2]. Inspired by structural morphology (Rene Motro, an anthology of structural morphology), which involves form, forces, material, and structures and aiming at developing a structural system with harmony synthesis of these four aspects, architectural morphology is defined by extending the connotation of structural morphology, which simultaneously deals with structural performance, architectural functions, and aesthetical requirement, aiming at developing an architectural system with a balance between these factors.

Topology optimization, a mathematical method to optimize material distribution in a given area according to given conditions and objective index, has attained its popularity in civil engineering and architectural design

owing to its potential to generate rational and aesthetic-artistic morphology [3]. Topology optimization was initially developed for applications in aeronautic and mechanical engineering [4], where the design space represents a continuum of material, and even small savings in weight are significant, for example, by saving fuel on thousands of journeys and/or saving material on thousands of mass-produced products. Amongst the many topology optimization methods that have been developed, common approaches include the solid isotropic material with penalization (SIMP) method [5–7], the (bidirectionally) evolutionary structural optimization (ESO or BESO) method [8, 9], level set methods [10–12], the moving morphable components (MMC) method [13, 14], and the independent continuous mapping (ICM) [15] method. Many of these approaches have been adopted for the application to the architectural morphology problem domain. For the design of bracing systems for high-rise buildings, Beghini et al. [16] proposed a topology optimization framework to integrate architecture and engineering. The generation of optimized shell- and large-scale spatial structures was investigated by Ohmori [17], who developed an extended ESO method, whereas Peng [18] applied the ICM method to designs of dendriform structures with hierarchical topologies similar to tree branches.

Whilst a wide range of literature can be found relating the application of topology optimization methods to architectural design, there still exist a number of gaps that necessitate further investigation, which this paper address. Firstly, researchers usually focus on a particular type of application scenario, such as beams, walls, or large-scale spatial structures, whereas a comprehensive study of how to use topology optimization to generate architectural morphology across many different application scenarios is still missing. Additionally, the relationship between the inputs to a topology optimization and the resulting morphology has not been investigated in detail. This lack of understanding of the sensitivity of the outputs to the inputs is one of the main obstacles preventing the architects from using topology optimization tools in practice. Thirdly, little research has been carried out to discuss and compare the topology and morphology of optimized architectural design from topology optimization in the perspective of aesthetic.

This paper first extracts and classifies the most common architectural scenarios based on their geometrical features and structural properties. It then derives the key parameters that affect the topological results and discusses their relative impact on these results. A methodology combining parametric modelling and topology optimization is then adopted for architectural morphology generation. By making use of the sensitive relationship between the resulting topology and the input parameters for optimization, a single solution, or a cluster of solutions, can be obtained. They are viewed as potential candidates for building designs, thus solving the problem of architectural morphology generation. Finally, a numerical case is adopted to compare morphology of different optimized shell results and provides some basic aesthetic evaluation from architect's perspective.

The outline of this article is as follows. In Section 1, the context of the study and the required background knowledge is presented. In Section 2, the morphology generation procedure is proposed, and the influential parameters are identified. The essential architectural application scenarios are classified in Section 3, along with a discussion on how the influential parameters relate to each architectural application. Section 4 assesses the relationship between optimization parameters and the topological results for each classification, and in Section 5, the specific example of the morphology generation of a shell structure is investigated. Finally, Section 6 highlights the conclusions of the work and discusses the implications for morphology generation in practice.

2. Morphology Generation Methodology

Topology optimization of structure generally involves the addition, subtraction, or elimination of material from within a design domain. Through iterative adjustment of material, the optimal topology, representing the force flow within the domain, will gradually emerge. In addition to having the best mechanical performance, it is often the case that the obtained topology is also highly aesthetic. This successful combination of engineering and art is therefore viewed as a desirable candidate for architectural morphology design. However, there is no guarantee that the configuration produced though topology optimization would always be suitable for direct employment in the next design stage, and usually some modification is necessary, which can be achieved by adjusting the influential parameters.

Before considering how to adjust the influential parameters accordingly, a method for solving the problem of architectural morphology generation via topology optimization is introduced below, and the parameters that play key roles in determining the resulting morphology are considered.

2.1. Influential Parameters. In this paper, topology optimization is used to generate architectural morphology; therefore, the optimization parameters for topology optimization of different structures and structural members are also used as the parameters for morphology generation of them. Some additional parameters are required for the topology optimization, such as load scenarios, boundary conditions, and material properties, which are not directly related to the morphology.

The first parameter to be considered, the design domain, is represented by a geometry with planar or spatial features. This is usually defined based on consideration of architectural functions, such as space division, people-flow, light, and ventilation requirements. For example, it can be a wall with openings representing doors and windows, a hemispherical shell with holes on the top representing skylights, or a trimmed solid box representing an entire building. It should be noted that, during the optimization process, only materials in the design domain can be removed, retained, or reintroduced. This means that the optimal topology can only be made up of material within the design domain. In this

way, the design domain, on the one hand, provides space for the morphology to change but, on the other hand, constrains the scope of that variation. Therefore, this essential relationship between the design domain and the resulting optimal topology makes the design domain one of the most dominant parameters that influences the optimization results of original structures.

The second consideration is the different loading scenarios on original structures. The purpose of topology optimization is to generate structural configuration with best mechanical performance under the external loads. The loads acting on buildings include gravity, live-, wind-, and snow-load, as well as concentrated (point) forces applied at certain positions to represent specific objects. With a small change in external loads, major variation of optimal topology can occur, since it is the mechanical response of the structure under these loads that determines the evolutionary direction of the optimization process.

Boundary conditions are the third parameter to consider. For buildings, boundary conditions usually include pin-supports, roller-supports, or fixed-supports. These supports can be present at specific discrete points, applied continuously along lines or curves, or even distributed across an entire surface. The boundary condition specifies the positions where the structure transfers its external loads to the foundations. Therefore, slight variations in boundary conditions also introduce significant changes in the optimization results.

Material properties also need to be carefully defined, and it is often the case that there will be more than one type of material being used within one architectural design of buildings or any specific structural members. For example, many high-rise buildings are constructed from steel beams, columns and decks, with a reinforced concrete slab poured on the deck in-situ to make a composite floor system. Specifying different material properties in different areas of a building can have a significant effect on its structural response, and hence its optimal topology. However, architectural morphology generation is usually carried out at an early stage of architectural design, at which point it is usually considered acceptable for only one material to be used for topology optimization. It is also a common assumption during early stage design that only linear elastic deformation would occur within the structure. In this case, the optimal topology for one material is also the optimal topology for another material. Therefore, for the purpose of this paper, the difference in the topology optimization results caused by the variation of materials can be assumed to be negligible.

Besides the optimization initialization parameters outlined above, the formulation of the topology optimization itself also involves the defining of parameters that have an impact on the results. Generally, the formulation of a topology optimization problem requires the definition of objective functions and constraint functions. The objective functions use objective index or performance index as dependent variable and input parameters as independent variable, and objective index or performance index is what researches want to maximize or minimize, for example, maximizing overall structure stiffness. Besides, researchers can use the constraint functions to apply specific geometric or mechanical constraint to optimized structures, such as minimum/maximum feature size [19, 20] and symmetry and pattern repetition [21]. These two kinds of functions are usually determined based on consideration of mechanical properties or geometric features of the design of original structure and can involve measures of deformation, stress, stability, material volume, etc. The influential parameters introduced above are classified into two categories as summarized in Table 1.

2.2. Morphology Generation Procedure. In this paper, the authors employ topology optimization as the method for generating candidates for architectural morphology designs, by changing the influential parameters listed in Table 1. The adopted procedure is shown in Figure 1, and a detailed explanation is given as follows:

(1) Define the formulation parameters (objective- and constraint functions)

(2) Define the initialization parameters (design domain, load, boundary conditions, and material properties)

(3) Use the parameters defined in Steps (1) and (2) to solve the topology optimization subproblem

(4) Evaluate the topology produced by Step (3). If satisfied, output the result; if not, return to Step (1) or (2) and modify the parameters accordingly

There are various options available to solve the topology optimization problem in Step (3). One approach is to implement source code, such as those introduced in Wei et al. [22]. The code solves minimum compliance problem, which maximizes overall structure stiffness under limited material usage. However, most users will choose to apply off-the-shelf software that provides the topology optimization functions, for example, one of the many plugins for Rhino/Grasshopper, such as TopOpt [23] and Ameba [24]. This kind of software is widely used in parametric model generation of optimized architecture. Additionally, some commercial Finite Element software packages have built-in Topology Optimization functionality, such as Altair Inspire [25] and OptiStruct [26]. This kind of software is adopted in vast range of engineering product design.

This study uses the three analysis techniques in the multiattribute decision-making method to build an evaluation analysis model to evaluate the obtained topological results. Firstly, the fuzzy Delphi method (FDM) is used to extract the design elements, which can have an important influence on the satisfaction of obtained topological results. This technology has been widely used in planning and evaluation research in related fields such as regional governance, community management, and landscape architecture [27, 28]. Compared with the traditional Delphi, the advantages of introducing the fuzzy technique include (i) reducing the number of surveys, (ii) the opinions of experts being expressed completely, (iii) the expert being relatively rational and in line with demand, and (iv) being economical in terms of time and cost. Secondly, regarding the

Table 1: Influential parameters for architectural morphology generation.

Influential parameters	Parameters for initialization of optimization problem	Design domain Load scenario Boundary condition Material property
	Parameters for formulation of optimization problem	Objective function Constraint function

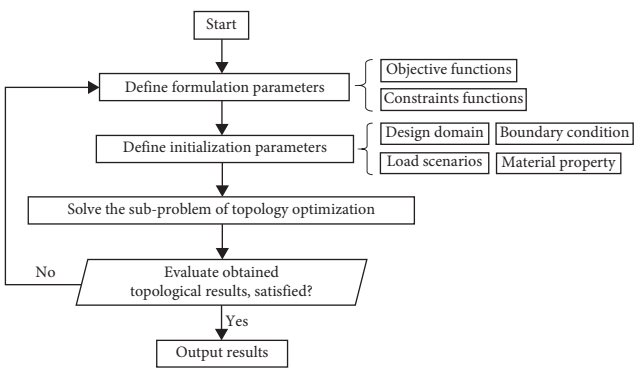

Figure 1: Morphology generation procedure.

clarification of the priority of the dimension layer, this study will apply the analytic hierarchy process (AHP) that has been widely used in related research to train the relative weight between the evaluation elements (dimension/elements). The application of this analysis technique relies on expert domain knowledge, through pairwise comparison between elements, to clarify stakeholders' considerations of the relative importance of elements. Finally, The Technique for Order of Preference by Similarity to Ideal Solution (TOPSIS) is used to sort and select the performance of several obtained topological results. This analysis technique was proposed by Hwang and Yoon [29]. The basic idea is that the closer to the positive ideal solution, the better; on the contrary, the farther away from the negative ideal solution, the better.

The FDM used in this study is to integrate expert opinions by means of "double triangular fuzzy number" [30], and to test whether expert cognition shows a consistent convergence effect by "grey zone verification method." The concrete steps are as follows:

Step (F1): The "most conservative cognitive value" and the "most optimistic cognitive value" given by all experts to each element i are statistically analyzed, and the extreme value outside "2 times standard deviation" is eliminated. Then, the minimum value C_L^i, geometric mean value C_M^i, maximum value C_U^i in the remaining "most conservative cognitive value," and the minimum value O_L^i, geometric mean value O_M^i and maximum value O_U^i in the "most optimistic cognitive value" are calculated, respectively.

Step (F2): Based on the calculation results of Step (F1), the three-angle fuzzy number $C^i = (C_L^i, C_M^i, C_U^i)$ of the "most conservative cognition" and the three-angle fuzzy number $O^i = (O_L^i, O_M^i, O_U^i)$ of the "most optimistic cognition" for each evaluation element i are calculated, respectively.

Step (F3): Testing whether the experts' opinions present a consistent convergence effect can be judged by the following ways.

(1) If there is no overlap between the two triangular fuzzy numbers, i.e., $C_U^i \le O_L^i$, it will be indicated that the opinion interval value of each expert has a consensus section, and the opinion tends to be within this consensus section, so the "consensus value" G_U^i of this evaluation element i can be calculated by

$$G_U^i = \frac{C_M^i + O_M^i}{2}. \tag{1}$$

(2) If there is an overlap between the two triangular fuzzy numbers, i.e., $C_U^i > O_L^i$, and the grey area $Z^i = C_U^i - O_L^i$ of the fuzzy relationship is smaller than the range $M^i = O_M^i - C_M^i$ between the "geometric mean of optimistic cognition" and "geometric mean of conservative cognition" for the evaluation criterion by the expert, it means that although there is no consensus section for each expert's opinion interval value, the two experts who gave extreme opinions (the most conservative expert of the optimistic cognition and the optimistic expert of the conservative cognition) do not differ too much from other experts in opinions and led to divergent opinions. Then, the "consensus value" G_U^i of this evaluation element i can be calculated by

$$G_M^i = \frac{O_M^i \times C_U^i - O_L^i \times C_M^i}{\left(O_M^i - O_L^i\right) + \left(C_U^i - C_M^i\right)}. \tag{2}$$

(3) If $C_U^i > O_L^i$ and $Z^i = C_U^i - O_L^i$ is larger than $M^i = O_M^i - C_M^i$, it means that there is no consensus section for each expert's opinion interval value, and the two experts who gave extreme opinions (the most conservative expert of the optimistic cognition and the optimistic expert of the conservative cognition) differ too much from other experts in opinions and led to divergent opinions. Therefore, it is necessary to carry out a new round of questionnaires and repeat steps one to three until all the evaluation items have reached convergence, and the corresponding "consensus value" is obtained.

The AHP is a comprehensive framework that is suitable for situations when people make multiobjective, multicriterion, and multisector decisions with or without certainty for any number of alternatives. The technique procedures to gain the weights are described as follows:

Step (A1): Compare the relative importance of factors pairwise and obtain an $n \times n$ pairwise comparison matrix, where n means the number of element.

Step (A2): Check the logical judgment consistency using the consistency index (C.I.) and consistency ratio (C.R.). The C.I. value is defined as C.I. = $(\lambda_{\max} - n)/(n-1)$, where $\lambda_{\max}$ is the largest eigenvalue of the pairwise comparison matrix. The C.R. value is defined as C.R. = C.I./R.I., where R.I. is a random index decided by the value of n. (The R.I. values corresponding to $n = 1, 2, \ldots, 10$ are 0, 0, 0.58, 0.9, 1.12, 1.24, 1.32, 1.41, 1.45, and 1.49, respectively.) In general, the values of C.I. and C.R. should be less than 0.1 or reasonably consistent.

Step (A3): Use the normalized eigenvector of the largest eigenvalue $\lambda_{\max}$ as the factor weights.

TOPSIS (technique for order preference by similarity to an ideal solution) method is presented in Chen and Hwang [31], with reference to Hwang and Yoon [29]. The TOPSIS procedure consists of the following steps.

Step (T1): Calculate the normalized decision matrix. The normalized value n_{ij} is calculated by

$$n_{ij} = \frac{x_{ij}}{\sqrt{\sum_{i=1}^{m} x_{ij}^2}}, \quad i = 1, \ldots m, \; j = 1, \ldots n. \tag{3}$$

Step (T2): Calculate the weighted normalized decision matrix. The weighted normalized value v_{ij} is calculated as

$$v_{ij} = w_{ij} n_{ij}, \quad i = 1, \ldots m, \; j = 1, \ldots n. \tag{4}$$

where w_{ij} is the weight of the $i-$th attribute, and $\sum_{i=1}^{m} w_j = 1$.

Step (T3): Determine the positive ideal and negative ideal solution.

$$\begin{aligned} A^+ &= \{v_1^+, \ldots, v_n^+\} \\ &= \left\{ \left(\frac{\max_j v_{ij}}{i \in I} \right), \left(\frac{\min_j v_{ij}}{i \in J} \right) \right\}, \\ A^- &= \{v_1^-, \ldots, v_n^-\} \\ &= \left\{ \left(\frac{\min_j v_{ij}}{i \in I} \right), \left(\frac{\max_j v_{ij}}{i \in J} \right) \right\}. \end{aligned} \tag{5}$$

The intention of using (5) is to calculate the maximum and minimum score of each criterion in each alternative.

Step (T4): Calculate the separation from the positive ideal solution, given as

$$d_i^+ = \left\{ \sum_{j=1}^{n} \left(v_{ij} - v_j^+ \right)^2 \right\}^{1/2}, \quad i = 1, \ldots, m. \tag{6}$$

Similarly, the separation from the negative ideal solution is given as

$$d_i^- = \left\{ \sum_{j=1}^{n} \left(v_{ij} - v_j^- \right)^2 \right\}^{1/2}, \quad i = 1, \ldots, m. \tag{7}$$

Step (T5): Calculate the relative closeness to the ideal solution. The relative closeness of the alternative A_i with respect to A^+ is defined as

$$R_i = \frac{d_i^-}{\left(d_i^+ + d_i^-\right)}, \quad i = 1, \ldots, m. \tag{8}$$

Since $d_i^- \geq 0$ and $d_j^+ \geq 0$ then, clearly, $R_i \in [0, 1]$.

Step (T6): According to the calculation of R_i value, the performance ranking of alternative cases can be obtained, and the higher the R_i value is, the higher the ranking order is.

3. Classification of Architectural Application Scenarios

In order to carry out the above procedure, it is important to know the allowable range within which each parameter (design domain, load scenario, and boundary condition) for such architectural application scenarios can vary. Since the range will depend to a large extent on the specific problem being investigated, it is necessary to divide the potential problems into subclasses and then address each in turn to determine suitable ranges.

3.1. Essential Architectural Application Scenarios. The two criteria for classification of problem scenarios adopted by the authors are the scenarios' force mechanisms and geometrical features, and typical scenarios are summarized in Table 2. For those scenarios, where the force mechanisms are constrained much within two dimensions, i.e., the forces are generally flowing within one plane, they are classified as surface application scenarios. Shells are included in this group, because the influence of their third dimension (thickness) is negligible to the other two dimensions, and under external load, the force within the shell can be viewed as flowing within its mid-surface. Scenarios that transfer load in three dimensions are classified as volumetric applications. They include joints (where forces do not generally lie in a single plane), multifloor buildings, and spatial structures. Of course, there are other ways of categorizing architectural application scenarios, and there are other scenarios that are not explicitly considered within this paper. However, the classification adopted here is sufficient to assess the likely limits for the modelling parameters across a suitably wide range of architectural scenarios.

3.2. Optimization Parameters. Based on the classification above, the ranges of influential parameters for morphology generation can be investigated. Since morphology generation usually takes place during early design stage, the parameters that formulate the topology optimization problem

Table 2: Essential architectural applications scenarios.

Surface application scenarios	Beams and arches Walls Shell structures
Volumetric application scenarios	Joints Multi-storey buildings Spatial structures

(objective functions and constraints functions) can remain unchanged. Additionally, it is usually structural stiffness and material volume that attract most attention in design optimization; therefore, it is reasonable to adopt the structural stiffness and material volume as objective and constraint, respectively.

In the following study, only the parameters for initialization of the optimization problem (the design domain, load and boundary condition) are investigated. The material property is omitted here, because, during the conceptual stage, it is sensible to assign only one type of material to the entire design domain, as discussed above. However, the effects of different combinations of materials on the topological results should still be borne in mind [32].

3.2.1. Parameters for Beams/Arches. Beams or arches can be characterized by their length to height ratio. They usually have a span around ten times larger than their height, which makes bending moments the dominant action. The common optimization parameters for beams/arches are summarized in Table 3, but of course many other parameters exist, and the approach proposed in this paper would be equally applicable to their investigation.

In terms of its design domain, it can be a rectangle, with or without a tapered or curved upper edge. Common load scenarios include distributed load acting along the top-, middle-, or bottom edge, or concentrated point load acting at some point along the span. Supports might be pinned, rolled, or (rotationally) fixed, generally positioned at the two ends of the beam/arch. The main difference between a beam and an arch is whether or not the supports resist the horizontal movement, with an arch able to thrust horizontally into the supports, and a beam not. Additionally, there may be several supports along the length of a continuous beam.

3.2.2. Parameters for Walls. The common optimization parameters for wall are summarized in Table 4, where the span-height ratio of a wall is much closer to unity. A wall might be supported at its two lower corners, or fully supported along its lower edge. Compressive loads usually dominate the design of wall, and gravity load is often the main source. However, in high-rise buildings, a wall's height can be significant compared to its span, and the lateral load generated by wind pressure can be the dominant scenario.

3.2.3. Parameters for Shells. The common optimization parameters for shells are summarized in Table 5, where shells have a span of tens or hundreds of their thickness. The shell can be hemispherical, cylindrical, saddle-shaped, or

Table 3: Parameters for beam/arch.

Parameters	Potential varying ranges
Design domain	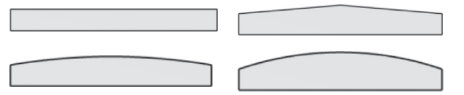
Load scenario	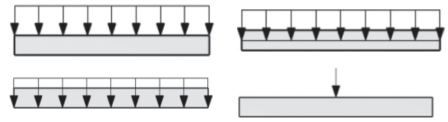
Boundary condition	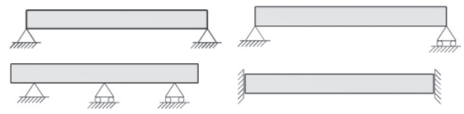

completely freeform. The most common loads acting on shells are out-of-plane loads such as gravity or area-distributed, but they can also resist loads in a horizontal plane, be they in a single direction or twisting-loads inducing a moment. Shells are usually supported around their lower edge, either at discrete points via pinned- or (rotationally) fixed-supports or continually around the edge.

3.2.4. Parameters for Joints. Joints usually occur at the intersection of several different components (usually beams), and their common optimization parameters are summarized in Table 6. The design domain for a joint can be a polygonal geometry, where the incoming members lie in a plane, or a solid sphere for fully 3D joints. The loads acting at joint are the forces transferred in from the surrounding components. During topology optimization, one of its edges or its surfaces usually is assumed totally fixed [33].

3.2.5. Parameters for Multistorey Buildings. The common optimization parameters for multistorey buildings are summarized in Table 7. Their design domain can be a regular solid geometry or a collection of several such geometries. The loads acting on them are usually gravity-based, but horizontal forces can also become dominant for high-rise buildings. Common boundary conditions include point-supports at the corners, edge-supports along the bottom edges, or full rotational restraint across their whole lower surface.

3.2.6. Parameters for Large-Scale Spatial Structures. The common optimization parameters for large-scale spatial structures are summarized in Table 8. Their design domain is similar to multistorey buildings, the difference being that the span of a spatial structure is usually much larger than its height, the exact opposite of a multistorey building. The loads and common boundary conditions are the same as those of multistorey buildings.

4. Relationship between Optimization Parameters and Topological Results

In this section, the beam/arch category is first chosen as the focus of a benchmark case-study to investigate the

Table 4: Parameters for walls.

Design domain	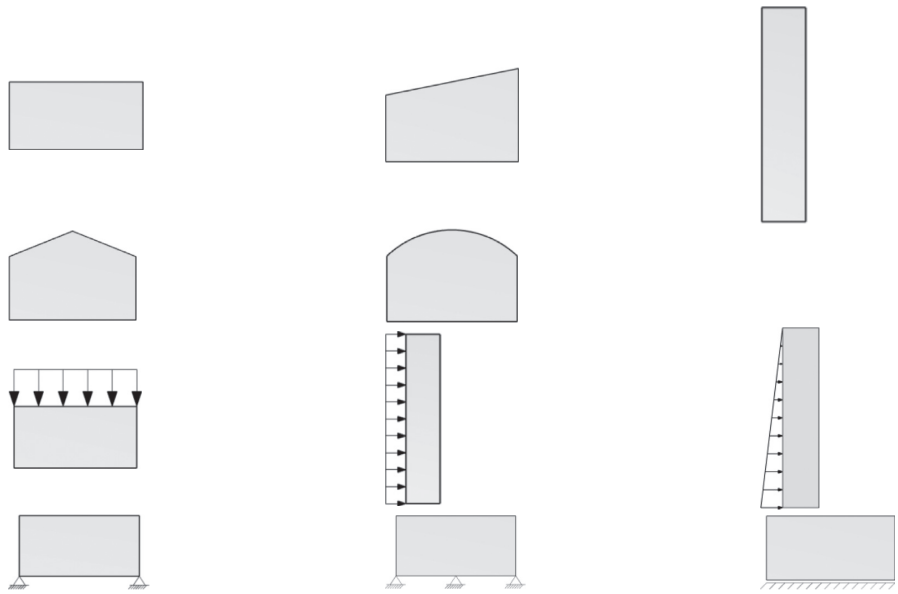		
Load scenario			
Boundary condition			

Table 5: Parameters for shells.

Design domain	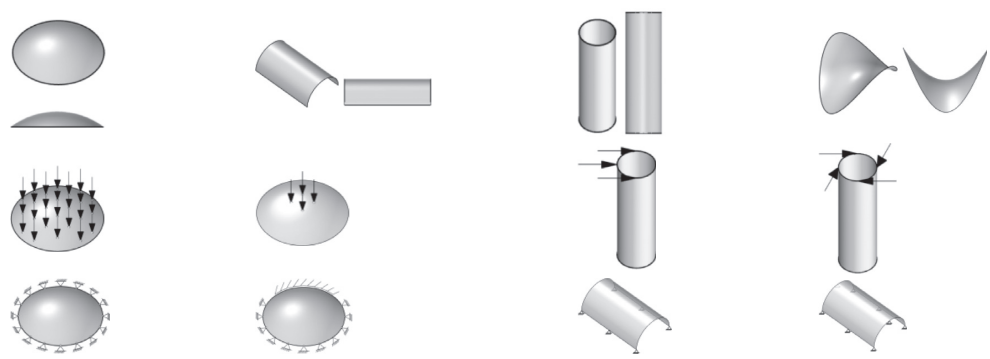			
Load scenario				
Boundary condition				

Table 6: Parameters for joint structures.

Design domain	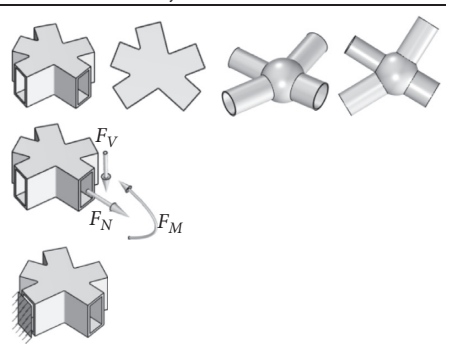
Load scenario	
Boundary condition	

relationship between the optimization parameters and the topological results. The extension of the approach to the morphology generation of shell structures is then discussed.

The relationship is investigated by conducting a parametric study on the different input parameters and assessing their effect on the topology optimization results. As a benchmark, typical optimization parameters are first assumed, and then variations around these benchmark values are analyzed and their effect quantified.

4.1. Benchmark Example. A rectangular surface with a span of 10 m and a height of 1 m is selected as the design domain for the benchmark study. Its boundary condition is two pinned supports at the lower two corners, and it has a uniformly distributed load acting along the top edge. To ensure that the load remains unchanged during topology optimization, a very thin layer of material that directly sustains the load is kept along the top edge during the whole optimization process. Strain energy is selected herein as the objective to be minimized, as it is commonly used in optimization to reflect the global flexibility of structure [7]. Steel is adopted as the material for the whole structure, and the material volume is constrained to be 30% of the material volume in the initial design.

The topologies at three different optimization iterations are shown in Table 9. The form of a single long-spanning arch emerged at the very start of the solution process and is unmistakable by the 50th iteration. The hierarchical

Table 7: Parameters for multistorey buildings.

Design domain	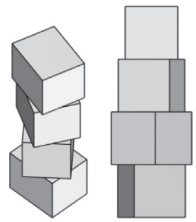
Load scenario	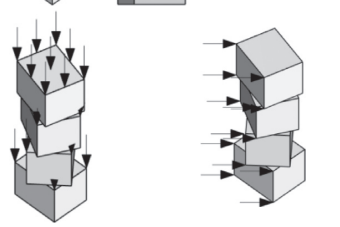
Boundary condition	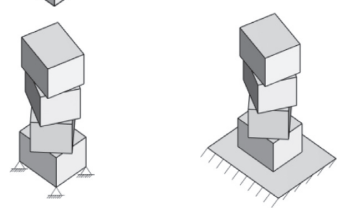

Table 8: Parameters for large-scale spatial structures.

Design domain	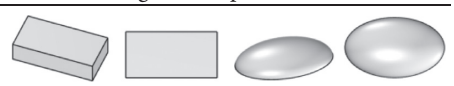
Load scenario	
Boundary condition	

branches reaching out from the main arch to the top edge gradually become more delicate as the iterations progress, and more material is removed. The resulting topology at iteration 150 explicitly symbolizes the force-paths but displays a discrete and organic geometry; thus, it can be viewed as a combination of mechanical rationality and architectural aesthetics.

4.2. Extended Examples. To investigate the influence of the optimization parameters on the obtained topological results, the topology optimization was run a number of times, each with different combinations of optimization parameters. The topological results were compared with the benchmark example in Table 9 to demonstrate these influences.

4.2.1. Design Domains. The top edge of the rectangular surface was curved in two different scales, and the topological results are shown in Table 10 (Rows 1 and 2). Comparison with the benchmark example shows that the morphologies are very similar, with the largest difference being the curvature of the arch, which adjusts to match the design domain.

Table 9: Topological result of typical beam/arch.

Sketch of optimization parameters	Iteration	Topological results
	50	
	100	
	150	

Table 10: Topological result of extended examples of beam/arch.

No.	Sketch of optimization parameters	Topological results	Notes
1			Design domain
2			Design domain
3			Load scenario
4			Load scenario
5			Load scenario
6			Boundary condition
7			Boundary condition
8			Volume constraint

4.2.2. Load Scenarios. The load acting along the top edge is first moved to the mid-line, then to the bottom edge, and finally changed to be a concentrated force acting at the midpoint of the top edge. The topological results are shown in Rows 3–5 of Table 10, respectively. When the load remains a uniformly distributed line load, the main structural system remains an arch, even when the line acts at a different position vertically. As the load moves downward, the secondary branches connecting to the main arch adjust automatically to transfer load from the points of application to the arch. These geometrical changes result in corresponding mechanical changes, since the forces in branches switch from compression to tension.

Concentrating the load into a point (Table 10 Row 5) converts the arch into a truss and allows the removal of material from other areas.

4.2.3. Boundary Conditions. Two kinds of boundary conditions are considered. One is simply supported at the left and right lower corners, and the other is clamped along the left and right edges. The corresponding optimization results are shown in Table 10 (Rows 6 and 7).

When one support of the benchmark is changed to a roller and no longer provides horizontal restraint (Table 10 Row 6), material is retained along the bottom edge, acting as a tension tie to prevent the relative displacement of the two supports. Another change is that, without the horizontal thrust

resistance of the supports, the structure represents a bowstring beam structure [34] rather than an arch. With fully fixed-supports available along the two edges (Table 10 Row 7), the obtained topology again represents a bowstring beam; however, its depth is roughly 1/5 of the span, and this can be mapped to the inflection points of its bending moment.

4.2.4. Material Volume Fraction. By varying the target volume fraction of material, different topological results are generated. Row 8 of Table 10 is obtained from a volume fraction of 50%. Comparison with the benchmark example shows little difference, but when more material is retained, most of it goes into thickening the arch.

4.2.5. Discussion. The influence of the four types of optimization parameters (design domain, load scenario, boundary condition, and material volume fraction) is investigated in this section. It can be concluded that the topological results are very sensitive to the optimization parameters, and slight changes in one parameter can result in a large difference to the obtained topology. Therefore, it is justified to demonstrate that this sensitive relationship can be used to generate a wide variety of optimal topologies, and amongst them, the best architectural design can be chosen.

5. Morphology Generation of Shells

Shells have been widely adopted as efficient solutions for covering large spaces, and the practical implementation of shells can be seen in exhibition pavilions, sports and entertainment venues, and transportation interchanges, to name a few. Famous examples include the Palazzetto Dello Sport by Pier Luigi Nervi in Rome, or Los Manantiales Restaurant by Felix Candela in Mexico [35]. However, within a fully continuous shell, there is generally some material that is not needed to transfer load to the supports, and it can therefore be removed. Topology optimization is adopted here as the approach to determine where to remove material from a shell. In this section, a truncated sphere shell is adopted for investigation, and the morphology generation results of this geometry are presented below.

5.1. Benchmark Example. We selected the stadium roof structure as a fixed functional requirement, and it is located in Guangzhou with a subtropical climate. The geometry considered here is a trimmed sphere, with a span of 60 m and a height of 10 m, as shown in Figure 2. It is pin-supported at 16 equally spaced points around the bottom edge. As in Section 4, steel is adopted as the material, strain energy is used as the objective function, and the material fraction target is 30% of the initial design domain. Only a uniformly distributed surface load is considered acting vertically. The load is first applied on an identical shell that has an extremely high stiffness. The load is then transferred to the topology optimization model by defining a tie-constraint between these two geometries. Since the load, geometry, and boundary conditions are all symmetric, a 1/4 substructure model is adopted for the topology optimization process, whilst the full model is used for visualization by mirroring the submodel along the two planes of symmetry.

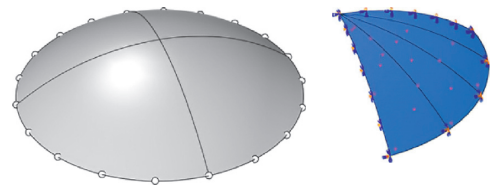

(a) (b)

Figure 2: Optimization parameters of spherical shell. (a) Whole structure. (b) 1/4 substructure.

The optimization of this geometry was carried out in Abaqus/Tosca [24]. The topologies at six different iteration steps are shown in Figures 3 and 4. Only cells with a density of 0.3 or greater are displayed to improve clarity. The main structural system has started to emerge by the 40th iteration, after which the hierarchical branches between main arches and rings gradually appear and become more and more delicate.

A modification to the geometry was made by introducing several holes into the design domain (see Figure 5). The holes can be viewed as a reflection of the architectural requirements, for example, roof-lighting or ventilation functions. Optimization of this new geometry is also carried out using the same optimization parameters.

The topologies at six different optimization iterations are shown in Figures 6 and 7. The main difference between this case and the one without holes is seen near the apex, where a small ring appears instead of a fully filled circle. The main structures reaching out from the supports also change from Y- to V-shapes, and the bottom ring moves up slightly. It can be concluded that the holes in the design domain have led to obvious changes in the topological results. However, these changes appear as adaptations of the original topology and remain aesthetically acceptable, which demonstrates the applicability of the proposed methodology.

5.2. Evaluation Example. The result of structural form generation basically conforms to the engineering aesthetic law of structural rationality, but the diversified result selection is mainly for the evaluation of architects. From the perspective of the law of formal beauty, we asked experts in the industry to discuss the shape of the shell structure and summarize 5 important evaluation factors. Based on it, the study uses a 9-point Likert scale for the expert questionnaire, which was sent to 37 experts. All of the experts interviewed had master's degrees or above, among which 12 had received doctoral degrees in architecture and related fields, and a total of 28 had more than 5 years of work experience of architectural design. A total of 32 valid questionnaires were finally collected, and the data was analyzed by the AHP method. The relative significance degrees among the five evaluation elements are shown in Table 11, and the opinions of the experts passed the test of consistency (CI = 0.087; CR = 0.078).

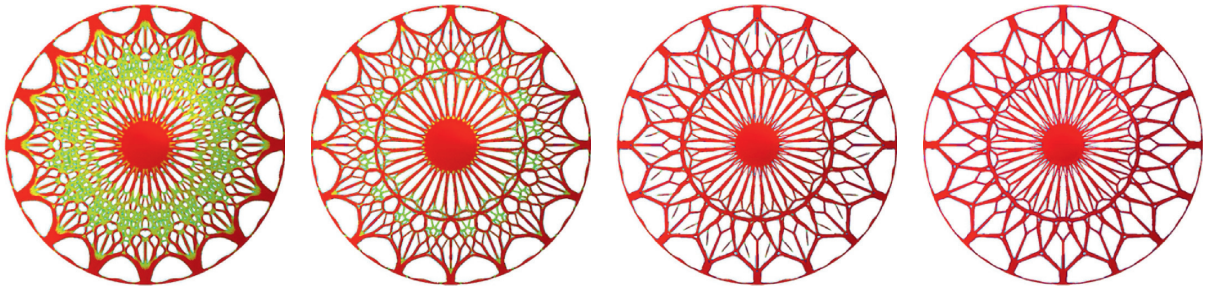

(a) (b) (c) (d)

Figure 3: Optimization results of a spherical shell (project view). (a) 40th iteration. (b) 60th iteration. (c) 80th iteration. (d) 95th iteration.

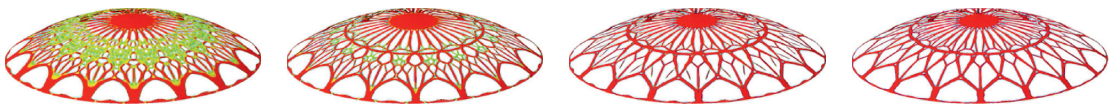

(a) (b) (c) (d)

Figure 4: Optimization results of a spherical shell (isometric view). (a) 40th iteration. (b) 60th iteration. (c) 80th iteration. (d) 95th iteration.

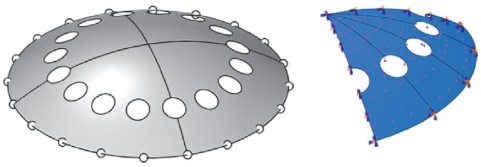

(a) (b)

Figure 5: Optimization parameters of spherical shell. (a) Whole structure. (b) 1/4 substructure.

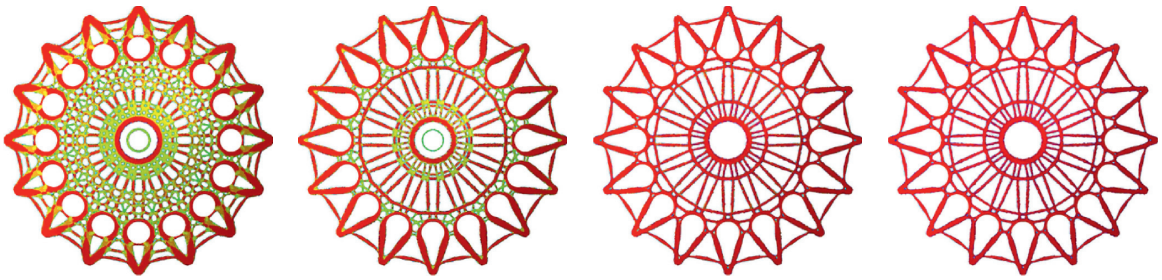

(a) (b) (c) (d)

Figure 6: Optimization results of a spherical shell with predefined holes (project view). (a) 40th iteration. (b) 60th iteration. (c) 80th iteration. (d) 95th iteration.

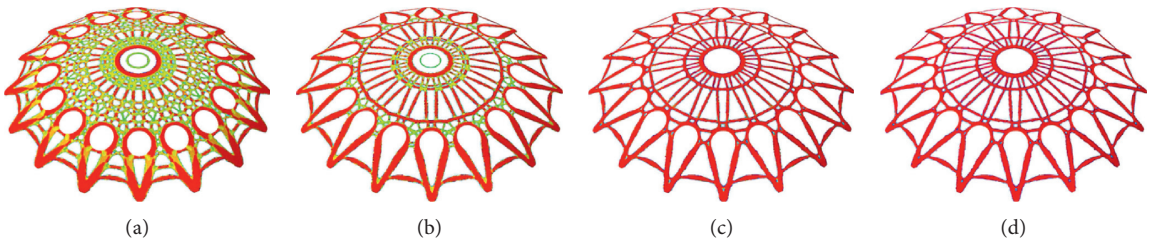

(a) (b) (c) (d)

Figure 7: Optimization results of a spherical shell with predefined holes (isometric view). (a) 40th iteration. (b) 60th iteration. (c) 80th iteration. (d) 95th iteration.

Table 11: Description of evaluation methods and relative weight.

Evaluation factors	Descriptions	Weights
Rhythmicity (E_1)	The constituent elements of the form offers an arrangement of structured repetition and alternation, bringing a visual aesthetics of continuity	0.131
Proportionality (E_2)	The size and quantity of each constituent element of the form meet a certain scale, conveying a sense of beauty	0.398
Balance (E_3)	The constituent elements of the form maintain a visual balance of forces	0.118
Layering (E_4)	Whether the constituent elements of the form convey a sense of layering, and show the varying characteristics of different layer	0.071
Concordance (E_5)	Whether the constituent elements of the form are in harmony with each other, creating a relatively coherent sense of form	0.282

Table 12: Performance ranking of evaluated cases.

No.	Evaluation examples	Evaluation factors								
		E_1	E_2	E_3	E_4	E_5	d_i^+	d_i^-	R_i	Rank
C1	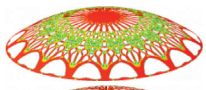	0.236	0.190	0.201	0.238	0.332	0.154	0.036	0.188	8
C2	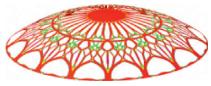	0.368	0.301	0.362	0.508	0.382	0.102	0.074	0.420	4
C3	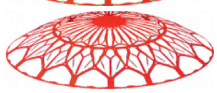	0.350	0.328	0.315	0.414	0.396	0.092	0.080	0.465	3
C4	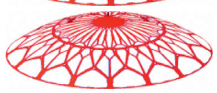	0.426	0.297	0.375	0.310	0.350	0.105	0.067	0.391	5
C5		0.512	0.486	0.418	0.293	0.452	0.029	0.144	0.833	2
C6		0.299	0.547	0.400	0.429	0.415	0.030	0.156	0.837	1
C7		0.289	0.256	0.358	0.285	0.216	0.138	0.033	0.195	7
C8		0.266	0.278	0.354	0.258	0.205	0.133	0.040	0.230	6

Then, with the eight shell structure forms obtained by topological optimization in the previous part of this paper as evaluation cases, the study applies TOPSIS method to evaluate the performance of each case and rank the cases based on experts' aesthetic experience. The performance evaluation questionnaire was designed on a scale of 0–10 and administered to a group of experts who had previously completed the AHP questionnaire. A total of 35 valid questionnaires were collected, and the results of the performance evaluation analysis are shown in Table 12.

According to the performance evaluation analysis, case C6 is the best solution among the eight shell structure forms, while the rest are C5, C3, C2, and C4 in order, and the worst solution in performance is C1. The study applies the AHP-TOPSIS model to integrate the subjective opinions of experts. After obtaining several structural forms that have structural rationality and conform to aesthetic laws, the study constructs an evaluation system to clarify the performance ranking of different structural forms. In summary, this study integrates the topology optimization tool kit and parametric design

theory with a MADM model to construct a process model that goes from the generation to the performance evaluation of structural forms of architecture. With the application of topology optimization and parametric design concepts, architects have access to a diverse selection of solutions. These solutions are consistent with structural rationality and a certain degree of engineering aesthetics. However, in real situations, the evaluation and ranking of structural design solutions generally requires a clear evaluation objective or perspective based on group decisions of stakeholders. The case evaluation in this section is conducted in the context of structural form aesthetics. In short, the evaluation and ranking of each design case is done based on the aesthetics of the form as the evaluation objective. However, a more theoretical and applied value is proposed in this study, which includes topology optimization, parametric modelling, and multiattribute decision-making process of building structure design. It covers the form of generation to evaluation and selection of structural design solutions.

6. Conclusions

In this study, by integrating topology optimization toolsets and parametric design theory, combined with multiattribute decision-making analysis, a method of morphology generation for architectural design is proposed. The design method could efficiently obtain several architectural structural morphologies with both structural rationality and aesthetic rules and complete the evaluation and selection of several alternatives through multiattribute decision-making. At the level of morphology generation, based on the load-bearing mechanism and geometrical features, the essential architectural application scenarios are classified into two groups in this study, namely, surface application scenarios (including beam/arch, wall, and shell) and volumetric application scenarios (including joints, multistorey buildings, and spatial structures). On this basis, the possible variation range of the optimization parameters (design domain, load scenario, and boundary condition) for such architectural application scenarios is determined. This will provide architects with direct guidance when applying topology optimization toolsets and parametric design theories to architectural morphology generation. On the other hand, by analyzing the relationship between the optimization parameters and the topological results, with the beam/arch application scenario as an example, it is proved that this sensitive relationship can be used to generate a cluster of alternatives for architectural morphology design. In addition, the morphology generation of shells is investigated through two different design domains, one with and one without holes. The organic, discrete, and mechanically rational topological results demonstrate the applicability and efficiency of the proposed methodology.

In order to clarify the whole process from architectural morphology generation to scheme evaluation and selection by the design method, the FAHP-TOPSIS model is applied to complete the performance ranking and selection of evaluation cases by taking 8 topological methodology generation results as evaluation cases, as well as the principle of architectural form, as the basic evaluation criteria in this study. In the future, scholars and architects can apply this design method in related studies, formulate corresponding evaluation objectives in specific realistic situations, and also complete the performance evaluation and ranking of several topological results by relying on expert experience. Even when the improvement of the design scheme after the evaluation ranking is discussed, DANP technology can be used to replace AHP technology in the future multiattribute decision-making model, so as to clarify the interaction relationship between the criteria under the proposed evaluation objectives, which is helpful in exploring the improvement strategy of different schemes from a systematic and dynamic perspective. In the follow-up study, a nonadditive performance analysis technique may be used tentatively instead of the TOPSIS technique used in this study. Therefore, the TOPSIS method used in this study to assess performance levels in the case studies is an additive method. However, circumstances in practice may often be nonadditive, and thus follow-up research may use nonadditive methods to assess performance more closely approximating actual circumstances.

Data Availability

The data used to support the findings of this study are included in the article.

Conflicts of Interest

The authors declare no conflicts of interest.

Acknowledgments

The authors are grateful to all the medical staff and designers who took part in this study. The authors would like to thank Lei Xiong, the research assistant, for all the hard work and effort put in to make the questionnaire survey a success. The authors are also immeasurably grateful to the alumni association of the Environmental Art Design, School of Architecture and Applied Art, Guangzhou Academy of Fine Arts, for the support during the research. This study was funded by the art projects supported by National Social Science Foundation (project number: 18BG08). This work was also supported by the Guangdong Philosophy and Social Sciences "Thirteenth Five-Year" Plan 2020 Annual Disciplinary Co-construction Project "Multi-attribute Decision Analysis and Activation Strategy Research on Cultural Heritage Blocks in Guangfu Region Based on AOD Concept" (project number: GD20XYS41).

References

[1] I. Dobritsyna, "Discreteness in the architecture of the 21st century," in *Proceedings of the 3rd International Conference on Art Studies: Science, Experience, Education (ICASSEE 2019)*, pp. 34–38, Moscow, Russia, November 2019.

[2] B. Kolarevic, *Architecture in the Digital Age: Design and Manufacturing*, Spon Press, New York, NY, USA, 2003.

[3] D. Lauriola, "Combining efficiency and aesthetics through the integration of structural topology optimization in architecture," M. S. thesis, Technical University of Cartagena, Cartagena, Spain, 2017.
[4] J.-H. Zhu, W.-H. Zhang, and L. Xia, "Topology optimization in aircraft and aerospace structures design," *Archives of Computational Methods in Engineering*, vol. 23, no. 4, pp. 595–622, 2016.
[5] M. P. Bendsoe, "Optimal shape design as a material distribution problem," *Structural Optimization*, vol. 1, no. 4, pp. 193–202, 1989.
[6] G. Rozvany, "The SIMP method in topology optimization-theoretical background, advantages and new applications," in *Proceedings of the 8th Symposium on Multidisciplinary Analysis and Optimization*, Long Beach, CA, USA, September 2000.
[7] O. Sigmund, "A 99 line topology optimization code written in matlab," *Structural and Multidisciplinary Optimization*, vol. 21, no. 2, pp. 120–127, 2001.
[8] Y. M. Xie and G. P. Steven, "A simple evolutionary procedure for structural optimization," *Computers & Structures*, vol. 49, no. 5, pp. 885–896, 1993.
[9] X. Huang and Y. M. Xie, "Convergent and mesh-independent solutions for the bi-directional evolutionary structural optimization method," *Finite Elements in Analysis and Design*, vol. 43, no. 14, pp. 1039–1049, 2007.
[10] J. A. Sethian and A. Wiegmann, "Structural boundary design via level set and immersed interface methods," *Journal of Computational Physics*, vol. 163, no. 2, pp. 489–528, 2000.
[11] M. Y. Wang, X. Wang, and D. Guo, "A level set method for structural topology optimization," *Computational Methods in Applied Mathematics*, vol. 192, no. 7, pp. 227–246, 2003.
[12] G. Allaire, F. Jouve, and A.-M. Toader, "Structural optimization using sensitivity analysis and a level-set method," *Journal of Computational Physics*, vol. 194, no. 1, pp. 363–393, 2004.
[13] X. Guo, "Doing topology optimization explicitly and geometrically—a new moving morphable components based framework," *Journal of Applied Mechanics*, vol. 81, no. 8, Article ID 081009, 2014.
[14] W. Zhang, J. Yuan, J. Zhang, and X. Guo, "A new topology optimization approach based on moving morphable components (MMC) and the ersatz material model," *Structural and Multidisciplinary Optimization*, vol. 53, no. 6, pp. 1243–1260, 2016.
[15] Y. Sui and X. Peng, "The ICM method with objective function transformed by variable discrete condition for continuum structure," *Acta Mechanica Sinica*, vol. 22, no. 1, pp. 68–75, 2006.
[16] L. L. Beghini, A. Beghini, N. Katz, W. F. Baker, and G. H. Paulino, "Connecting architecture and engineering through structural topology optimization," *Engineering Structures*, vol. 59, pp. 716–726, 2014.
[17] H. Ohmori, "Computational m," *International Journal of Space Structures*, vol. 26, no. 3, pp. 269–276, 2011.
[18] X. Peng, "Structural topology optimization method for morphogenesis of dendriforms," *Open Journal of Civil Engineering*, vol. 6, no. 4, pp. 526–536, 2016.
[19] O. Sigmund, "Morphology-based black and white filters for topology optimization," *Structural and Multidisciplinary Optimization*, vol. 33, no. 4–5, pp. 401–424, 2007.
[20] J. K. Guest, "Imposing maximum length scale in topology optimization," *Structural and Multidisciplinary Optimization*, vol. 37, no. 5, pp. 463–473, 2009.
[21] Y. Liu, Z. Li, P. Wei, and W. Wang, "Parameterized level-set based topology optimization method considering symmetry and pattern repetition constraints," *Computer Methods in Applied Mechanics and Engineering*, vol. 340, pp. 1079–1101, 2018.
[22] P. Wei, Z. Li, X. Li, and M. Y. Wang, "An 88-line MATLAB code for the parameterized level set method based topology optimization using radial basis functions," *Structural and Multidisciplinary Optimization*, vol. 58, no. 2, pp. 831–849, 2018.
[23] Food4Rhino, Topopt [Online]. Available:, Accessed on, 2021.
[24] Food4Rhino, Ameba [Online]. Available:, Accessed on, 2021.
[25] CAD Software Direct, Cad & 3D sales [Online]. Available:, Accessed on, 2021.
[26] Altair, Optimization-enabled structural analysis [Online]. Available:, Accessed on, 2021.
[27] Y. Wang and G.-T. Yeo, "Intermodal route selection for cargo transportation from korea to central asia by adopting fuzzy Delphi and fuzzy ELECTRE I methods," *Maritime Policy & Management*, vol. 45, no. 1, pp. 3–18, 2018.
[28] V. Assumma, M. Bottero, and R. Monaco, "Landscape economic attractiveness: an integrated methodology for exploring the rural landscapes in Piedmont (Italy)," *Land*, vol. 8, no. 7, p. 105, 2019.
[29] C. L. Hwang and K. Yoon, *Methods for Multiple Attribute Decision Making*, Springer, Berlin, Germany, 1981.
[30] T. B. Jeng, *Fuzzy assessment model for maturity of software organization in improving its staff's capability*, Ph.D. dissertation, National Taiwan University of Science and Technology, Taibei, Taiwan, 2001.
[31] S. J. Chen and C. L. Hwang, *Fuzzy Multiple Attribute Decision Making: Methods and Applications*, Springer-Verlag, Berlin, Germany, 1992.
[32] K. Tajs-Zielińska and B. Bochenek, "Topology optimization-engineering contribution to architectural design," *IOP Conference Series Materials Science and Engineering*, vol. 23, no. 4, Article ID 082057, 2017.
[33] H. Seifi, A. Rezaee Javan, S. Xu, Y. Zhao, and Y. M. Xie, "Design optimization and additive manufacturing of nodes in gridshell structures," *Engineering Structures*, vol. 160, pp. 161–170, 2018.
[34] M. Saitoh and A. Okada, "The role of string in hybrid string structure," *Engineering Structures*, vol. 21, no. 8, pp. 756–769, 1999.
[35] S. Adriaenssens, P. Block, D. Veenendaal, and C. Williams, *Shell Structures for Architecture: Form Finding and Optimization*, Routledge, New York, NY, USA, 2014.

Hindawi
Advances in Civil Engineering
Volume 2021, Article ID 4482887, 9 pages
https://doi.org/10.1155/2021/4482887

Research Article

A Study on the Effect of Hollow Tubular Flange Sections on the Behavior of Cold-Formed Steel Built-Up Beams

Balaji Shanmugam,[1] **Manikandan Palanisamy**,[2] **Paul O. Awoyera**,[3] **Senthilnathan Chinnasamy**,[1] **and Mahalakshmi Subramaniam**[1]

[1]*Department of Civil Engineering, Kongu Engineering College, Perundurai 638060, Tamil Nadu, India*
[2]*Department of Civil Engineering, Sona College of Technology, Salem 636005, Tamil Nadu, India*
[3]*Department of Civil Engineering, Covenant University, PMB 1023, Ota, Nigeria*

Correspondence should be addressed to Balaji Shanmugam; er.shbalaji@gmail.com

Received 30 June 2021; Accepted 2 September 2021; Published 27 September 2021

Academic Editor: Rahul V. Ralegaonkar

This paper deals with a study conducted on flexural behavior of cold-formed steel built-up I-beams with hollow tubular flange sections. There were two types of test sections, namely, built-up sections that were assembled with either stiffened or unstiffened channels coupling back-to-back at the web and a hollow tubular rectangular flange at the top and bottom of the web to form built-up I-beam. The flexural behavior along with the strength and failure modes of the built-up sections was examined using the four-point loading system. Nonlinear finite element (FE) models were formulated and validated with the experimental test results. It was observed that the developed FE models had precisely predicted the behavior of built-up I-beams. Further, the verified FE models were used to conduct a detailed parametric study on cold-formed steel built-up beam sections with respect to thickness, depth, and yield stress of the material. The flexural strength of the beams was designed using the direct strength method as specified in American Iron and Steel Institute (AISI) for the design of cold-formed steel structural members and was compared with the experimental results and the failure loads predicted from FE models. Since the results were not conservative, a new customized design equation had been mooted and delineated in the study for determining the flexural strength of cold-formed steel built-up beams with hollow tubular flange sections.

1. Introduction

Cold-formed steel (CFS) sections have been transformed as inherent elements in the construction and building industry due to CFS products that have a larger strength to weight ratio, enhanced stiffness, mass production, and speedy and simple installation [1, 2]. With the advent of aluminum/zinc coating, the applications of CFS sections have become widespread across the world. The CFS built-up sections commonly have single or double symmetric shapes with stiffening lips on flanges and unstiffened or stiffened webs.

Quite a large number of investigations have been carried out in the recent past on the behavior and design of CFS beams under different loading conditions. Wang et al. [3] have optimized the cross-sectional shapes of CFS beams and beam-columns by considering the axial load and the bending moment for a single-symmetric section. Yuan et al. [4] and Moen and Schafer [5] have investigated the buckling behavior of CFS beams with holes in the web. Wang and Young [6] have studied the behavior of CFS built-up section beams with different screw arrangements. Ma et al. [7] also have suggested design equations for CFS tubular beams. However, it is observed that CFS hollow flange built-up sections are structurally more competent than the usual open channel sections [8]. The flexural performance of conventional built-up sections can be enhanced by means of hollow flange sections as a large amount of mass is placed away from the strong section axis [9].

In early 1990s, the hollow flange beams with better buckling capacities for their distinct shape were first

introduced in Australia [10]. Besides, these sections performed well against distortional buckling because of the existence of rigid hollow flange sections at the top and bottom of the web. The cold-formed hollow flange steel section is believed to have the benefits of both hot-rolled and conventional CFS sections [11]. There are only a few research studies that have been carried out on the behavior of rectangular [12–16] and triangular hollow flange sections [17–19]. Keerthan et al. [2] have suggested the equations of design to predict the web crippling capacity of hollow flange beam sections.

The hollow flange CFS sections are usually fabricated either by cold-forming a single steel sheet to a preferable shape or by merely connecting three steel elements. The former process is quite complicated compared with the latter because the hollow flange elements are well-connected (top and bottom of the web) and secured by means of rivet/screw or spot welding. In addition, the latter with different grades and thickness can be used for T-section (web and flange) [8]. Furthermore, the residual stresses and initial geometric imperfections which differ from common hot-rolled and CFS may be introduced if the sections are fabricated by cold-forming a single sheet [2].

In the present investigation, an effort has been made to explore the flexural behavior of CFS hollow tubular flange built-up I-beam sections. The beam consists of both stiffened and unstiffened channels that are connected back-to-back so as to form a web and a flange at the top and the bottom. Nonlinear FE models are developed for the proposed sections using FEA software ANSYS to confirm the results of the experimental test. A detailed parametric study is performed using the FE model with respect to material factors such as yield stress, section thickness, and depth of the beam. As per the citations of the AISI standard [20], using direct strength method (DSM), the estimated strength of the beams is compared with the experimental results and the failure load prediction from FE models.

2. Experimental Study

2.1. Hollow Tubular Flange I-Beam Sections. The beams were fabricated in two stages; initially, the channel sections were made by cold-forming a single sheet using press-braking process and then the two channel sections were connected together (back-to-back) with structural bolts to form the web of the I-section. Later on, the rectangular hollow tubular cold-rolled sections were linked above and beneath the web by self-threaded screws. Both the web and the flange were made up of steel with 1.6 mm thickness, and the geometries were attached so as to satisfy the standards given in the DSM of CFS design as shown in Figure 1. The fasteners were fixed both in the web and the flange at a uniform spacing of 140 mm. The spacing of the fasteners was designed by considering the spacing requirements of AISI specifications [20]. The nominal diameter of the screw and the bolt was 4.8 mm and 10 mm, respectively. The position of the fasteners across the cross section of the beam is shown in Figure 2. The study was conducted in two test series, wherein stiffened and unstiffened web sections were examined with three different web aspect ratios (web length to web depth) such as 6, 7.5, and 10 per test series. The beam length was 1500 mm, and the specimens were labeled so that the web (stiffened or unstiffened) and the depth of the beam could easily be identified. For instance, the label with USW 300 denotes the unstiffened web specimen with the overall depth of 300 mm. The details of the test specimens are shown in Table 1. The material properties are determined by the tensile coupon test, and the average values that are recorded in the test are presented in Table 2. Those properties were used in the later part of the study for numerical investigation and strength calculation.

2.2. Test Set-Up and Instrumentation. A four-point flexural loading system was employed for testing the specimens. The ends of the beams were placed on a roller and pinned support, respectively, so as to provide a simply supported condition. The distance between the supports was 1400 mm. The test was conducted with the loading frame of 1000 kN. Three linear variable displacement transducers (LVDTs) were utilized to measure the in-plane vertical displacements; one at the midspan section of the beam and the other two under the loading points. One of the LVDTs is used to measure the lateral deformation of the web at midspan section as shown in Figure 3. A number of strain gauges are instrumented across the cross section as shown in Figure 4 at the midspan of the beam to record the longitudinal strains. Initially, a trivial load was applied on the beam to allow the loading and support arrangement to adjust uniformly on the bearings. The load was applied gradually by a hydraulic jack and monitored by a load cell. The entire set-up was associated to a data acquisition system where the load, displacement, and strain readings were recorded at even intervals throughout the test. As the test was employed to examine the in-plane deformation under the load, restraints were provided to prevent out-of-plane movement at the supports and at the loading points. Additionally, steel cushion plates of 6 mm thickness were placed at the loading and at the supports to avoid stress concentration in those points.

3. Numerical Investigation

A nonlinear FE analysis has been carried out using ANSYS software to predict the performance of the proposed hollow flange built-up sections. Four nodded SHELL 181 elements (with midline offset option) were used to model the beam section and the steel bearings at the supports and at the loading points. Based on the limitations of the model, a 10 mm mesh size was brought into the proposed study. For modeling the connections (Figure 5), coupling option was used [21–23]. As suggested by Manikandan et al. [24], two types of analyses, namely, eigenvalue buckling analysis and static nonlinear buckling analysis were employed. Eigenvalue buckling analysis was used to find the buckling loads and the corresponding buckling modes of the beam, whereas the material and geometric nonlinearity were included in the

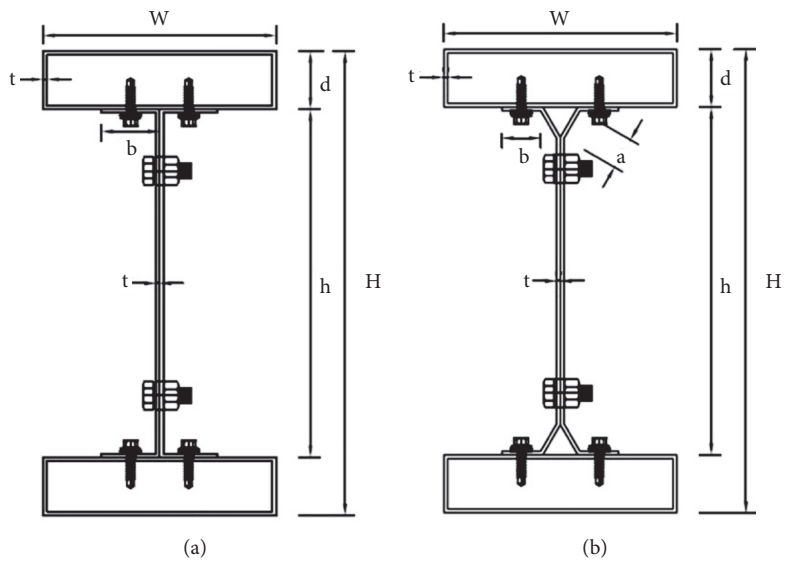

Figure 1: Section geometries: (a) unstiffened beam section; (b) stiffened beam section.

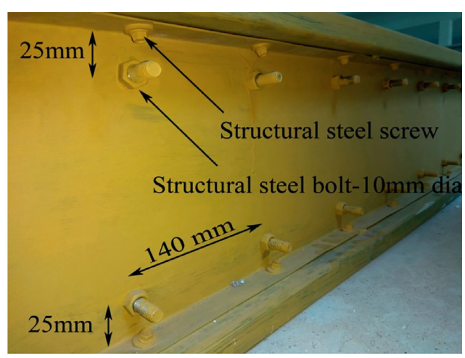

Figure 2: Longitudinal profile indicating the location of fasteners.

Table 1: Specimen details.

Specimen	Length (mm)	Section dimensions						
		w (mm)	d (mm)	t (mm)	a (mm)	b (mm)	h (mm)	H (mm)
200 USW	1500	100	25	1.6	—	25	150	200
250USW	1500	100	25	1.6	—	25	200	250
300USW	1500	100	25	1.6	—	25	250	300
200SW	1500	100	25	1.6	17.5	17.5	150	200
250SW	1500	100	25	1.6	17.5	17.5	200	250
300SW	1500	100	25	1.6	17.5	17.5	250	300

Table 2: Material properties.

Young's modulus (N/mm^2)	Ultimate tensile strength (N/mm^2)	% elongation	Yield strength (N/mm^2)
2×10^5	310	15.5	220

nonlinear buckling analysis. However, the residual stress and the effect of cold-forming operation were excluded in the analysis. For the material of nonlinearity, bilinear stress-strain curve was adopted [25]. As the geometric imperfection was not calculated in the experimental program, a value of $L/1000$ which was suggested by Xu et al. [22] and Kankanamge and Mahendran [26] was brought into the static nonlinear buckling analysis. A complete FE model of a hollow flange beam section with bearing plates (at loading points and supports) is shown in Figure 6.

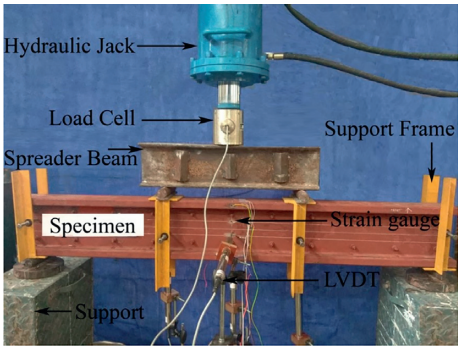

Figure 3: Test set-up and instrumentation.

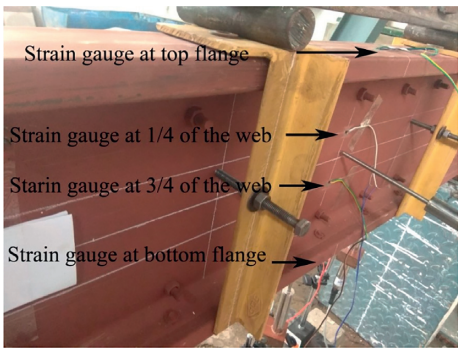

Figure 4: Position of strain gauges for strain measurements.

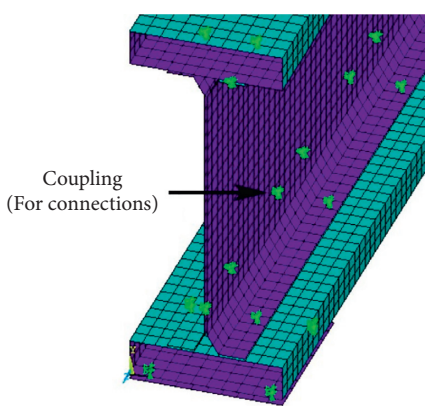

Figure 5: Connections in the FE model.

4. Theoretical Investigation

The values from experimental (M_{EXP}) and numerical investigations (M_{ANSYS}) were compared with the flexural strength (M_{DSM}) computed from the direct strength method (DSM) using AISI specifications [20] for CFS structural members. As stated in DSM, the nominal flexural strength was the least which was considered for the buckling loads (lateral torsional, local, and distortional) and the corresponding values were calculated.

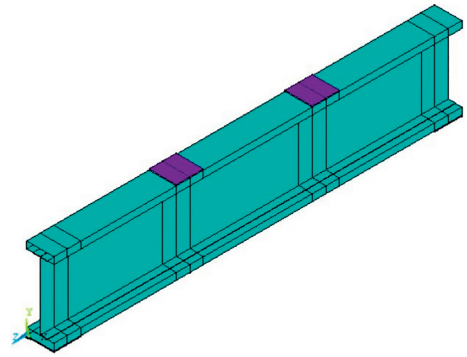

Figure 6: FE model with bearing plates at the supports and loading points.

5. Results and Discussion

The results obtained from experimental investigation, FE analysis, and design strength of DSM are reported in Table 3. The load-deflection response of unstiffened beam sections is shown in Figure 7. As a part of the experimental investigation, longitudinal strains were recorded for all the specimens using the strain gauge mounted at different locations of the beam. For instance, the variations in longitudinal strain along with the depth of the beam at midspan for 250USW section are shown in Figure 8. The bottom flange and the lower part of the web (bottom three-forth height of the web) had demonstrated a fairly linear increase in the positive strain (due to tension) for every raise in the load, whereas the top flange and the upper part of the web (top three-fourth height of the web) had indicated a fairly linear increase in the negative strain (due to compression). Nevertheless, the variation of strain in the web section at the supports was found to be absolutely nonlinear.

Invariably, the sections with the depths of 200 and 250 mm had failed due to flexural buckling, and with further increase in the load, the local buckling occurs in the tension flange of the beams. However, for 300 mm depth, due to the effect of slender web, the failure was initiated by the local buckling of the web section, and the further increase in the load had resulted in web buckling at the supports. On account of the specimen dimensions, the detected failure modes of the beam were localized at the end sections of the beam, where the moment was almost zero. This behavior is illustrated in Figures 9 and 10, which clearly demonstrates that the sections cannot handle the localized shear failure. The figures indicate that the results of the experiment are well-matched with those of the numerical study.

The stiffened web interrupted the premature buckling of the flange. However, it is observed that the web stiffeners are closer to the flange that led to the premature bucking of web at the supports as shown in Figures 11 and 12. The web buckling has more control over the load carrying the capacity of beams when compared with the flange buckling. If the web stiffeners are close to the flange (i.e., at flange-web junction), their effectiveness get decreased. Therefore, the present study has found that the load carrying the capacity of

Table 3: Comparison of results.

Specimen	Ultimate load (kN)			M_{EXP}/M_{ANSYS}	M_{EXP}/M_{DSM}	M_{ANSYS}/M_{DSM}	Failure mode
	M_{EXP}	M_{ANSYS}	M_{DSM}				
200 USW	14.74	15.78	9.79	0.93	1.51	1.61	FLB + GB
250 USW	12.99	14.35	10.92	0.91	1.19	1.31	FLB + GB
300 USW	9.68	9.98	11.96	0.97	0.81	0.83	WLB + GB
200 SW	8.96	9.51	6.28	0.94	1.43	1.51	FLB + GB
250 SW	10.78	10.15	7.83	1.06	1.38	1.30	FLB + GB
300 SW	11.14	11.62	8.70	0.96	1.28	1.34	WLB + GB

FLB: flange local buckling; WLB: web local buckling; and GB: global buckling.

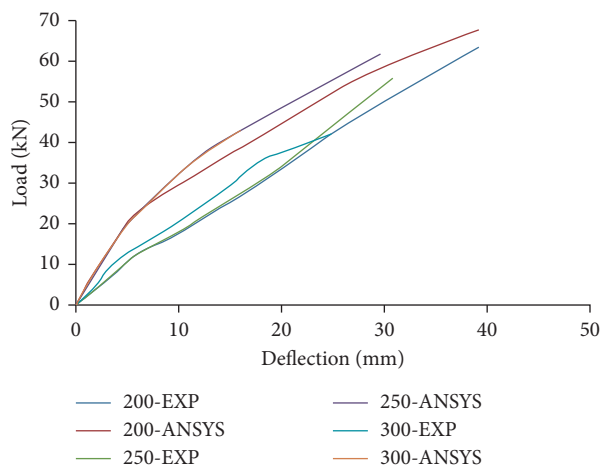

Figure 7: Load-deflection response of unstiffened beam sections.

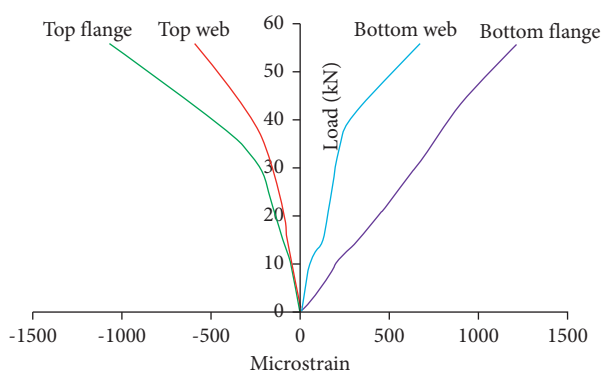

Figure 8: Variations in longitudinal strain along the depth of the beam at midspan for 250USW section.

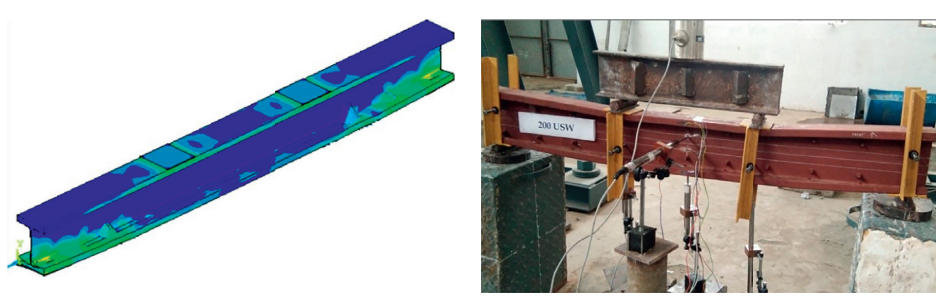

(a) (b)

Figure 9: Failure mechanism of (unstiffened) 200USW beam section: (a) ANSYS; (b) experimental.

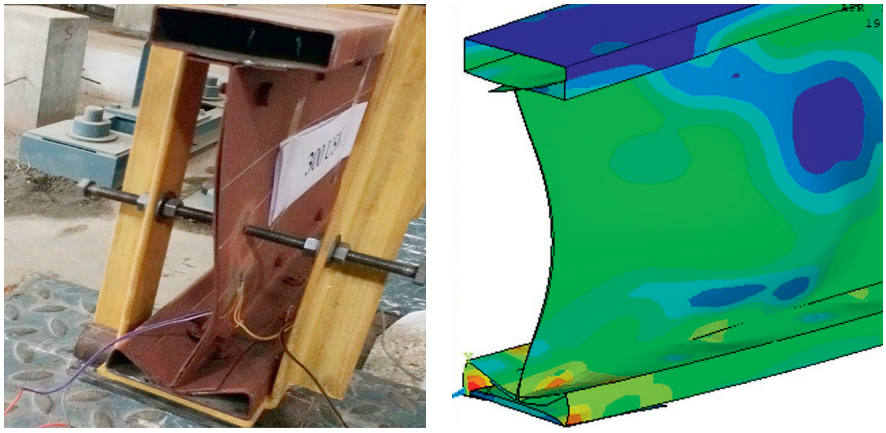

(a) (b)

Figure 10: Failure mechanism of (unstiffened) 300USW beam section: (a) experimental; (b) ANSYS.

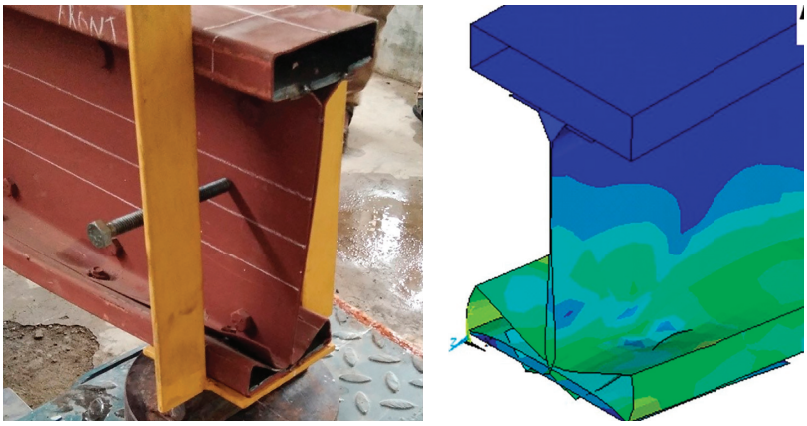

(a) (b)

Figure 11: Failure mechanism of (stiffened) 200SW beam section: (a) experimental; (b) ANSYS.

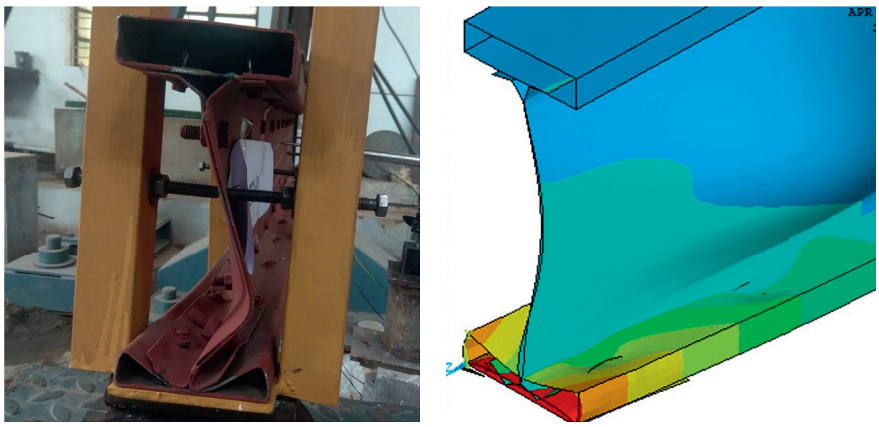

(a) (b)

Figure 12: Failure mechanism of (stiffened) 300SW beam section: (a) experimental; (b) ANSYS.

Table 4: Evaluation of FE analysis and DSM results.

Model ID	Depth (mm)	Yield stress (N/mm^2)	Thickness (mm)	Flexural strength (kNm)					
				M_{ANSYS}	M_{DSM}	M_Y	M_{ANSYS}/M_{DSM}	M_D	M_{ANSYS}/M_D
D200Y220T1.2	200	220	1.2	9.33	6.02	17.98	1.55	7.82	1.19
D250Y220T1.2	250	220	1.2	7.23	6.67	24.66	1.08	7.37	0.98
D300Y220T1.2	300	220	1.2	6.65	7.28	31.81	0.91	7.09	0.94
D200Y275T1.2	200	275	1.2	10.76	6.93	22.48	1.55	8.50	1.27
D250Y275T1.2	250	275	1.2	8.34	7.67	30.82	1.09	7.92	1.05
D300Y275T1.2	300	275	1.2	7.93	8.37	39.77	0.95	7.89	1.01
D200Y340T1.2	200	340	1.2	12.28	7.92	27.79	1.55	9.13	1.34
D250Y340T1.2	250	340	1.2	9.98	8.76	38.11	1.14	8.55	1.17
D300Y340T1.2	300	340	1.2	9.13	9.54	49.17	0.96	9.10	1.00
D200Y220T1.6	200	220	1.6	15.78	9.79	23.80	1.61	14.22	1.11
D250Y220T1.6	250	220	1.6	14.35	10.92	32.64	1.31	14.20	1.01
D300Y220T1.6	300	220	1.6	9.98	11.96	42.13	0.83	13.74	0.73
D200Y275T1.6	200	275	1.6	16.40	11.30	29.75	1.45	15.83	1.04
D250Y275T1.6	250	275	1.6	14.91	12.58	40.80	1.19	15.43	0.97
D300Y275T1.6	300	275	1.6	12.05	13.76	52.66	0.88	14.76	0.82
D200Y340T1.6	200	340	1.6	16.86	12.94	36.78	1.30	17.38	0.97
D250Y340T1.6	250	340	1.6	15.33	14.38	50.44	1.07	16.58	0.92
D300Y340T1.6	300	340	1.6	14.39	15.71	65.11	0.92	15.84	0.91
D200Y220T2.0	200	220	2	22.81	14.19	29.52	1.61	21.63	1.05
D250Y220T2.0	250	220	2	21.70	15.92	40.51	1.36	22.67	0.96
D300Y220T2.0	300	220	2	21.14	15.74	47.07	1.34	20.47	1.03
D200Y275T2.0	200	275	2	23.33	16.42	36.90	1.42	24.52	0.95
D250Y275T2.0	250	275	2	23.25	18.36	50.63	1.27	25.10	0.93
D300Y275T2.0	300	275	2	22.15	18.14	58.83	1.22	22.25	1.00
D200Y340T2.0	200	340	2	23.61	18.84	45.62	1.25	27.41	0.86
D250Y340T2.0	250	340	2	23.47	21.02	62.60	1.12	27.41	0.86
D300Y340T2.0	300	340	2	22.37	20.73	72.74	1.08	23.90	0.94
Mean							1.22		1.00
Standard deviation							0.24		0.13

unstiffened beam is superior than the stiffened beam section. Similar type of behavior was observed by Manikandan and Sukumar [25], wherein the strength of built-up I-beam along with stiffened channel sections (connected back-to-back) was found to be less than the beams with unstiffened channel sections.

6. Parametric Study

A detailed parametric study was done with the aid of the verified FE model to calculate the strength and flexural behavior of the hollow flange built-up beam sections. The parametric study was conducted only for the unstiffened hollow flange beam sections as the stiffened web sections did not have any considerable effect on the flexural capacity of beams. Yield stress, depth, and the thickness of the section were considered as variable parameters whilst the beam length and bolt spacing remained constant. The yield stress of the material was taken as 220 N/mm^2, 275 N/mm^2, and 340 N/mm^2, whereas the thickness of the sections was taken as 1.2 mm, 1.6 mm, and 2 mm. A total number of 27 FE models were analyzed in the parametric study. The results and their comparisons with theoretical investigation are presented in Table 4. It can be observed that the DSM values (M_{DSM}) were not conservative with the results of FEA (M_{ANSYS}). The DSM method had underestimated the flexural strength of cold-formed steel built-up beams with hollow rectangular flange sections. The average value of M_{ANSYS}/M_{DSM} ratio was equal to 1.22 with a standard deviation of 0.24. Hence, in this investigation, a new customized design curve (shown in Figure 13) and a design formula (given in equation (1)) are proposed to determine the flexural strength of cold-formed steel built-up beams with hollow rectangular flange sections. The design flexural strength (M_D) was calculated using the proposed design equation, and the average value of M_{ANSYS}/M_D ratio was equal to 1.00 with a standard deviation of 0.13. The design flexural strength had agreed well with the results of FEA.

Further, it can be noticed that the yield stress, depth, and the thickness of the material have a significant influence on the strength of the section. However, it is observed that the web aspect ratio does not have a significant effect on the load carrying capacity of beams at higher thickness and yield stress.

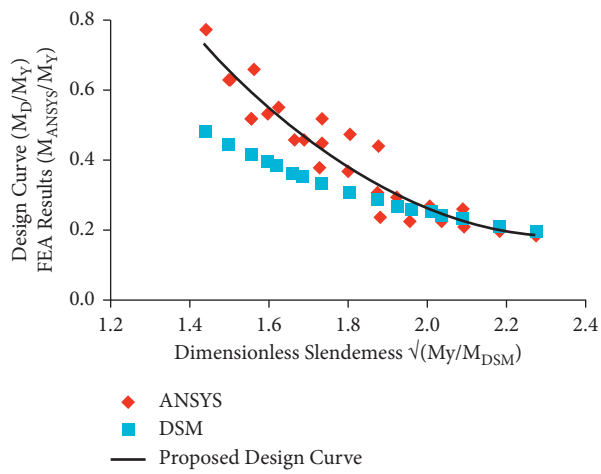

Figure 13: Design curve.

$$M_D = \begin{cases} M_Y, & \text{for } \lambda_d \leq 1.4, \\ M_Y\left(0.697\left(\dfrac{M_Y}{M_{DSM}}\right) - 3.24\left(\sqrt{\dfrac{M_Y}{M_{DSM}}}\right) + 3.96\right), & \text{for } \lambda_d > 1.4, \end{cases} \quad (1)$$

where

M_{DSM} is the flexural strength using the direct design method

M_Y is the yield strength

M_D is the design flexural strength

$\lambda_d = \sqrt{M_Y/M_{DSM}}$

7. Conclusions

In this work, a detailed investigation has been carried out on the flexural behavior of built-up CFS beams with hollow tubular flange sections, and the following inferences are drawn:

(1) Due consideration has to be given to web buckling and web aspect ratio in the design of hollow tubular flange CFS built-up section.

(2) Simple web stiffeners do not have any significant effect on the load carrying capacity. The web stiffeners that are closer to the flange (flange/web junction) led to premature buckling of the web at the supports.

(3) The yield stress, thickness, depth, and web aspect ratio of the section play a substantial role in the flexural capacity of the beam.

(4) The experimental results are well-compared with the numerical study. However, geometric imperfection may be the reason for the minor difference in the values. The failure mode prediction by FE models is matched exactly with the experimental test results.

(5) Flexural strength of the beams, designed using AISI specification [20], is mismatched with the experimental results and the failure load prediction (FE models). Hence, the customized design equation has been mooted and delineated in this study to determine the flexural strength of cold-formed steel built-up beams with hollow tubular flange sections.

Data Availability

The "Experimental Research" data used to support the findings of this study are available from the corresponding author upon request.

Conflicts of Interest

The authors declare that there are no conflicts of interest.

References

[1] L. Sundararajah, M. Mahendran, and P. Keerthan, "Web crippling experiments of high strength lipped channel beams under one-flange loading," *Journal of Constructional Steel Research*, vol. 138, pp. 851–866, 2017.

[2] P. Keerthan, M. Mahendran, and E. Steau, "Experimental study of web crippling behaviour of hollow flange channel beams under two flange load cases," *Thin-Walled Structures*, vol. 85, pp. 207–219, 2014.

[3] B. Wang, G. L. Bosco, B. P. Gilbert, H. Guan, and L. H. Teh, "Unconstrained shape optimisation of singly-symmetric and open cold-formed steel beams and beam-columns," *Thin-Walled Structures*, vol. 104, pp. 54–61, 2016.

[4] W.-b. Yuan, N.-t. Yu, and L.-y. Li, "Distortional buckling of perforated cold-formed steel channel-section beams with circular holes in web," *International Journal of Mechanical Sciences*, vol. 126, pp. 255–260, 2017.

[5] C. D. Moen and B. W. Schafer, "Elastic buckling of cold-formed steel columns and beams with holes," *Engineering Structures*, vol. 31, no. 12, pp. 2812–2824, 2009.

[6] L. Wang and B. Young, "Behaviour and design of cold-formed steel built-up section beams with different screw arrangements," *Thin-Walled Structures*, vol. 131, pp. 16–32, 2018.

[7] J.-L. Ma, T.-M. Chan, and B. Young, "Design of cold-formed high strength steel tubular beams," *Engineering Structures*, vol. 151, pp. 432–443, 2017.

[8] S. Kesawan, M. Mahendran, Y. Dias, and W.-B. Zhao, "Compression tests of built-up cold-formed steel hollow flange sections," *Thin-Walled Structures*, vol. 116, pp. 180–193, 2017.

[9] N. Tondini and A. Morbioli, "Cross-sectional flexural capacity of cold-formed laterally-restrained steel rectangular hollow flange beams," *Thin-Walled Structures*, vol. 95, pp. 196–207, 2015.

[10] One Steel Australian Tube Mills (OATM), *Design of Lite Steel Beams*, One Steel Australian Tube Mills (OATM), Brisbane, Australia, 2008.

[11] R. I. Dempsey, "Structural behaviour and design of hallow flange beams," in *Proceedings of the 2nd National Structural Engineering Conference*, pp. 327–335, Institution of Engineers, Adelaide, Australia, January 1990.

[12] S. Kesawan, V. Jatheeshan, and M. Mahendran, "Elevated temperature mechanical properties of hollow flange channel sections," *Construction and Building Materials*, vol. 87, pp. 86–99, 2015.

[13] S. Kesawan and M. Mahendran, "Post-fire mechanical properties of cold-formed steel hollow sections," *Construction and Building Materials*, vol. 161, pp. 26–36, 2018.

[14] E. Magnucka-Blandzi, "Effective shaping of cold-formed thin-walled channel beams with double-box flanges in pure bending," *Thin-Walled Structures*, vol. 49, no. 1, pp. 121–128, 2011.

[15] T. Anapayan and M. Mahendran, "Improved design rules for hollow flange sections subject to lateral distortional buckling," *Thin-Walled Structures*, vol. 50, no. 1, pp. 128–140, 2012.

[16] T. Anapayan, M. Mahendran, and D. Mahaarachchi, "Lateral distortional buckling tests of a new hollow flange channel beam," *Thin-Walled Structures*, vol. 49, no. 1, pp. 13–25, 2011.

[17] P. Avery and M. Mahendran, "Finite-element analysis of hollow flange beams with web stiffeners," *Journal of Structural Engineering*, vol. 123, no. 9, pp. 1123–1129, 1997.

[18] M. Mahendran and P. Avery, "Buckling experiments on hollow flange beams with web stiffeners," *Journal of Structural Engineering*, vol. 123, pp. 1130–1134, 2002.

[19] P. Avery, M. Mahendran, and A. Nasir, "Flexural capacity of hollow flange beams," *Journal of Constructional Steel Research*, vol. 53, no. 2, pp. 201–223, 2000.

[20] American Iron and Steel Institute, *AISI-S100:Specification for the Design of Cold-Formed Steel Structural Members*, American Iron and Steel Institute, Granite City, IL, USA, 2016.

[21] W.-X. Ren, S.-E. Fang, and B. Young, "Finite-element simulation and design of cold-formed steel channels subjected to web crippling," *Journal of Structural Engineering*, vol. 132, no. 12, pp. 1967–1975, 2006.

[22] L. Xu, P. Sultana, and X. Zhou, "Flexural strength of cold-formed steel built-up box sections," *Thin-Walled Structures*, vol. 47, no. 6-7, pp. 807–815, 2009.

[23] M. M. Pastor and F. Roure, "Open cross-section beams under pure bending II. Finite element simulation," *Thin-Walled Structures*, vol. 47, no. 5, pp. 514–521, 2009.

[24] P. Manikandan, S. Balaji, S. Sukumar, and M. Sivakumar, "Experimental and numerical analysis of web stiffened cold-formed steel channel column with various types of edge stiffener," *International Journal of Advanced Structural Engineering*, vol. 9, no. 2, pp. 129–138, 2017.

[25] P. Manikandan and S. Sukumar, "Behaviour of stiffened cold-formed steel built-up sections with complex edge stiffeners under bending," *KSCE Journal of Civil Engineering*, vol. 19, no. 7, pp. 2108–2115, 2015.

[26] D. N. Kankanamge and M. Mahendran, "Behaviour and design of cold-formed steel beams subject to lateral-torsional buckling," *Thin-Walled Structures*, vol. 51, pp. 25–38, 2012.

Hindawi
Advances in Civil Engineering
Volume 2021, Article ID 1908568, 10 pages
https://doi.org/10.1155/2021/1908568

Research Article

Energy Auditing for Efficient Planning and Implementation in Commercial and Residential Buildings

Angalaeswari Sendrayaperumal,[1] Somyak Mahapatra,[1] Sabuja Sanket Parida,[1] Komal Surana,[1] Parandhaman Balamurugan,[2] L. Natrayan,[3] and Prabhu Paramasivam[4]

[1]*School of Electrical Engineering, Vellore Institute of Technology, Chennai 600127, Tamil Nadu, India*
[2]*eVITRC, Vellore Institute of Technology, Chennai 600 127, Tamil Nadu, India*
[3]*Department of Mechanical Engineering, Saveetha School of Engineering, SIMATS, Chennai 602105, Tamil Nadu, India*
[4]*Department of Mechanical Engineering, College of Engineering and Technology, Mettu University, Mettu 318, Ethiopia*

Correspondence should be addressed to Angalaeswari Sendrayaperumal; angalaeswari.s@vit.ac.in, L. Natrayan; natrayanphd@gmail.com, and Prabhu Paramasivam; prabhuparamasivam21@gmail.com

Received 28 July 2021; Revised 22 August 2021; Accepted 2 September 2021; Published 15 September 2021

Academic Editor: Rahul V. Ralegaonkar

The ideology of ensuring energy-efficient design and construction of buildings by providing minimum requirements is the core objective of this work. Energy audit was conducted to improve the design of the building with incremental requirements to further enhance the energy efficiency. The Energy Conservation Building Code (ECBC) has been modified extensively over the years, starting from its initial deployment in the year 2011 to its latest modifications in the year 2019. The energy conservation standards in ECBC apply to building envelope, heating ventilation, air conditioning, lighting, service water heating, and electric power distribution. It should also be ensured that all-electric systems, transformers, energy-efficient motors, and diesel generators must meet the regulated set of mandatory requirements. From among the various software types that have been approved for ECBC design and application, this study has employed Energy Plus software to simulate the design based on the given input and the selected location. The location that has been chosen for this study was Bhubaneshwar, India. All necessary details ranging from latitude, longitude, weather, time zone, elevation, building area, lighting, heating, cooling, and much more have been covered in the simulation. Utilizing ECBC regulated standards for an energy-efficient building design has resulted in an increase in the energy savings by 27.4%, and thus, the building qualifies to be regarded as an ECBC compliant building.

1. Introduction

In India, the increased level of energy consumption has led to awareness regarding energy conservation among the public at a national level. The energy conservation bill along with the energy conservation Act was passed in the year 2001 and was later amended in 2010. The energy management center was reestablished and renamed as Bureau of Energy Efficiency (BEE) in the year 2002 [1]. Further in 2007, the BEE launched the Energy Conservation Building Code (ECBC) to set up the minimum requirements for the construction of buildings to attain energy efficiency by properly following the design specifications. The main aim of ECBC is to meet out the increasing energy demand in newly constructed buildings. Similar to ECBC, the Energy conservation Policies of Buildings (ECPB) in China combine the national-level plans to be implemented, laws to be followed, and the regulations for the buildings in order to enhance the energy efficiency [2].

The energy code established by the European commission known as the Energy Performance of Buildings Directive (EPBD) emphasizes that new buildings must be zero energy buildings by the year 2020 [3]. The acceptable indoor conditions in a building are being suggested by national and

international Indoor Environmental Quality (IEQ). A critical review that provides comparisons of the requirements for environmental conditions by taking into consideration international standards such as international organization for standardization (ISO), American Society of Heating, Refrigerating and Air conditioning Engineers (ASHRAE), and national standards of countries like India and China can be founded [4]. This article critically reviews the standards for thermal comfort, with the main focus being on the quality of indoor air.

The trend to modify the existing structure of buildings in terms of construction and load equipment has shifted to a new paradigm of energy conservation. Scenario-tree method-based impact analysis and the optimization of the overall cost of electricity and natural gas for a building operation over a time horizon are minimized while satisfying the energy balance and complicated operating constraints of individual energy supply equipment and devices. It was proved that significant energy cost savings can be achieved through integrated scheduling and controlling of various building energy supply sources with emphasis on the full utilization of solar energy and optimization of the operation of electrical storage. It was also shown that precooling is a simple way to achieve energy savings [5].

Pan et al. [6] proposed an IoT based framework for smart energy buildings, wherein the broad application of the proposed solution has led to significant economic benefits not only in terms of energy-saving and improving home/office network intelligence, but also in bringing in a huge social impact in terms of global sustainability. In [7], the analysis of the energy-saving potential in shopping centers in two selected countries was conducted by implementing energy-efficient measures based on shopping center market data, and the key energy figures and scenarios of the energy consumption were predicted and computed till the year 2030.

It is held that the behavior of a person depends on the living environment, which is based on values related to energy usage and energy consumption of the building. The occupants' comfort level plays a vital role in the performance and productivity level of any commercial building. By taking into consideration the occupant-related value, occupant-related review has been carried out in two phases in buildings in twenty-three regions [8]. The first phase comprises quantitative analysis based on the schedules and the density of occupants, while the second phase was carried out based on the code requirements. The occupants broadly categorized as residential and office building occupants were taken for analysis, and the satisfactory level of energy usage and consumption was measured. A survey was carried out with the task of design and validation of the questionnaire, occupant values, and potential energy-related factors, enrollment of the answerer, and the analysis of the survey [9]. The survey identified that among the occupant values that were important was health, which had significant influence on the performance.

To reduce the manual dependency, an automated energy compliance checking algorithm was proposed in [10] based on the information extracted using the ontology approach. This algorithm consisted of seven steps to evaluate the gathered data. Using various combinational techniques, the information about the building was gathered and compared with the standard codes. The proposed algorithm was tested with the energy requirements of the conservation code and was found to produce a precise output of 98 percent.

In this work [11], a passive methodology for reducing the energy consumption in HVAC systems of a commercial building by providing thermal insulation using composite materials and shaded windows was proposed and implemented leading to green building. The state-of-the-art materials and solutions implemented in the design process of buildings are described in [12]. The energy performance of a building was assessed through TRNSYS simulations according to its location (mountain, temperate continental climate area), occupancy, and specific office activities with low energy building as the target. A renewable energy mix consisting of the ground-water heat pump, flat plate solar thermal collectors, and a photovoltaic platform is expected to cover 90.9% of the energy demand of the building.

The optimal cost reduction measures in demand for space heating that is attained by efficient energy conservation measures and district heating systems were investigated in [13] as a Swedish case study, and it was observed that the investment cost for the proposed energy conservation measure was higher for the given scenario. In [14], it was stated that, in the state of Gujarat in India, over a span of forty years, the energy consumption in commercial buildings will be higher by fifteen times and that in the residential buildings will be higher by four times if the energy policies are not implemented. The open-source model, namely, Global Change Assessment Model (GCAM), was adopted in [14] to connect demand and supply. The GCAM has been developed further by considering separate models for India and Gujarat. Finally, it was concluded that the awareness about the ECBC codes and the concept of green buildings would decrease the new capacity addition of electricity with economical savings.

The indices proposed by the Taiwan government that include envelope energy load and performance of air conditioning systems have been incorporated for the building envelopes and air conditioning systems [15]. A multi-objective model was developed based on the above indices to achieve minimal cost and minimal carbon-dioxide emission. The model was integrated and coded in Fortran language using the MATLAB platform. In this study, a comparison was made among the various building components such as walls, glass curtains, glass, and roofs for unoptimized and optimized designing of the building.

A review on the energy conservation has been carried out in [16], and the steps involved were discussed considering the behavioral change of the works, altering the design of the existing structure, using proper energy sources, implementing the needed driver circuits, carrying out of substituting materials, and finally adopting the traditional building methods. Reports show that it is possible to predict the peak demand of a building using pivot table analysis as mentioned in [17]. A university campus was considered for analysis, and the peak demand of the building along with the factor that contributes more to the peak demand was

predicted using real-time data. This analysis suggested energy management in high peak demand building.

Machine learning algorithm has been used to predict the energy demand in [18] to increase the use of renewable energy and reduce energy consumption. The data corresponding to various commercial buildings for a period of two years was selected for the analysis. The estimation of power consumption at the microlevel leads to high internal gain as highlighted in [19]. Among the two models that have been proposed, the first model relied on the samples, while the second model used a bottom-up method for estimating the demand and energy usage.

The work in [20] integrates microgrid with the smart grid, thereby decentralizing the power flow, through which the excess of harvested energy within the community is distributed amongst them. This is expected to solve issues such as (1) balancing of supply/demand within MGs, (2) understanding how energy allocation to a user affects his/her community, and (3) identifying the economic benefits for the users. The authors proposed six Energy Allocation Strategies (EASs) for MGs ranging from simple to optimal as well as their combinations. The usage of harvested energy within the MG is maximized.

For the implementation of ECBC, the buildings are classified based on their function, design, and construction. For an ECBC building, the minimum energy savings should be 25%, while those for ECBC plus should be at least 35%, and those for Super-ECBC should be 50% and above. The major classifications include the following: hospitality buildings that provide accommodation for commercial purposes such as hotels, lodges, and resorts and health care buildings like hospitals, research centers, laboratories, and test houses that are being used to provide medical assistance to individuals who suffer from mental or physical ailments.

Buildings that are used for recreational, entertainment, religious, travel, or social purposes, cinema halls, airports, railway stations, and gathering halls are categorized as assembly buildings, while buildings that are utilized for carrying out business transactions, keeping financial records, and other similar purposes are generally termed as business buildings. They are further classified into 24-hour business and daytime business. By default, all business-buildings have both these subdivisions. It includes buildings used to provide education, including schools, universities, and training institutions.

Shopping Complex includes buildings that are used as part of shops and stores that sell various products and merchandise, for example, wholesale stores, retail stores, and shopping malls. In Mixed-Use Buildings, if the building has a lot of classifications and is fewer than 10% of the total grade floor area, then the classification having the highest percentage will determine its requirements, and if the classifications exceed 10% of the total grade floor area, then each classification that is above 10% will determine its requirements.

The objective of this work is to conduct an energy audit in a commercial building and to propose new load equipment and structural modifications in the building for energy saving and to make the building ECBC compliant. For this purpose, a commercial building was chosen in the city of Bhubaneshwar, India, and an energy audit was performed. Based on the consumption and utilization, a detailed audit on the energy requirements was carried out. Developing an energy-efficient building from the construction stage will result in greater energy savings and hence in the cost. So, the audit aims to propose new load equipment consuming less energy without affecting the comfort level of the user. This will guide the new users to build/develop more greener buildings that consume reduced energy, thereby leaving a negligible carbon footprint.

2. Methods and Detection

The methods and detection comprise 3 parts, namely, mandatory requirements, performance characteristics, and electrical system.

2.1. Mandatory Requirements. The buildings must adhere to all the mandatory requirements that include *Fenestration*, *Opaque Construction, Day Lighting,* and *Building Envelope Sealing* [21]. Fenestration refers to products that are transparent or translucent materials along with sash, dividers, and frame. Windows, sliding glass doors, skylights, garden windows, and glass blocks are few prominent examples. *Opaque Construction* usually comprises the structural or support portion of the building that can be constructed using a variety of materials.

The above grade floor area must meet the daylight requirements as per the various classifications of buildings. Assembly buildings are often exempted from meeting these requirements as they might interfere with their normal functioning. The day lighting requirements of various building are as follows: business and education buildings: 40%, hospitality and health care buildings: 30%, and shopping complexes: 45%.

There is a requirement for sealing off certain areas of the building with an exception for naturally ventilated buildings and spaces. These areas include joints around fenestration, openings between walls and foundations, and those between walls and roof. The fitting of exhaust fans should be done with a sealing device, for example, a self-closing damper, and operable fenestration should be constructed to avoid air leakages from fenestration frame and shutter frame.

2.2. Performance Characteristics. The properties and requirements of buildings can be assessed and specified based on the following performances characteristics.

U Factor. It is the rate at which fenestration products conduct non-solar heat flow. The lower the U-Factor, the more energy efficient the windows, glass doors, and skylights [22].

Air Leakage. In the presence of a specific pressure difference, air leakage is the rate of air movement around windows, doors, and other forms of fenestration. Products that have a lower air leakage rating are

much tighter than those that have a higher air leakage rating.

2.3. Electrical System

2.3.1. Transformers. While choosing the rating and design for a power transformer, it is to be ensured that the minimum acceptable efficacy at 50% and full-load rating is satisfied. Allowable net loss values should not exceed 5% of the maximum total loss of oil type transformer, with voltage greater than 11 kV but less than 22 kV and 7.5% of the maximum total loss of oil type transformer with voltage greater than 22 kV but less than or equal to 33 kV. Regular assessment of losses should be conducted using proper modern meters, and also in transformers with a capacity higher than 500 kVA, there should be additional attachments of current transformers and potential transformers to monitor and study the periodic losses. Voltage-drop for feeders should not exceed 2% at the rated/specified load, and voltage-drop for branch circuit should not exceed three percent at the specified regular load.

2.3.2. Energy Efficient Motors. Three-phase asynchronous motors should follow the Indian Standard (IS) 12615 with individual requirements for ECBC, ECBC+, and Super-ECBC buildings. ECBC buildings should use motors of IE 2 class, i.e., high efficiency, while motors used in ECBC plus and Super-ECBC buildings should be of IE 3 class, i.e., premium efficiency and IE 4 class, i.e., super-premium efficiency, respectively. All polyphase motors that have been permanently wired with 0.375 kW or more and are being used in the building are expected to operate for more than 1,500 hours per year. All polyphase motors that have been permanently wired with 50 kW or more and are being used in the building are expected to operate for more than 500 hours per year. Both of these should have a minimum acceptable nominal full load motor efficiency.

The horsepower ratings of the motor should not exceed 20% of the maximum forecasted load being served. The nameplates should contain a list of the nominal motor efficiencies and power factor at full-load. Proper rewinding practices should be followed for any rewound motors, and in cases where this is not possible, the damaged motor should be replaced with a new and efficient one.

The rating of the diesel generator in ECBC buildings should be at least 3 stars, while the generators in ECBC plus buildings and Super-ECBC buildings should have minimum ratings of 4 stars and 5 stars, respectively.

3. Software Implementation

Energy Plus is a simulation software that is highly efficient in modeling and calculating energy consumption levels for heating, ventilation, cooling, lighting, plugs, and much more. The major features of this software are as follows:

Integrated, simultaneous solution: These include thermal zone conditions and an HVAC system that does not assume that the HVAC system put in place could necessarily meet the zone loads and be able to simulate unconditioned and underconditioned spaces.

Building object: This describes all the parameters that are being utilized throughout the process of simulation of any building. The data entries of a particular object and certain inputs from the site are linked together in ways such as weather station and site and height variation objects, more specifically within the terrain field.

Subhourly, user-definable time steps: The thermal zones and the environment interact through automated varying time steps for a similar interaction between thermal zones and HVAC. This imparts the Energy Plus software with fast dynamics while at the same time trading of the speed of simulation for precision.

Location object. This helps identify the building's location. Most importantly, it allows for only one particular location. The existence of a weather data file location for the location of choice would override the object.

Advanced fenestration models: These could include a variety of items such as manual and automated controllable window blinds, layer-by-layer heat balances, and electrochromic glazing, which helps computation of solar energy that is being engrossed by the window panes.

Illuminance and glare calculations: These are used for reporting visual comfort and driving lighting controls.

Component-based HVAC: This supports both standard and novel system configurations.

Built-in HVAC and lighting control strategies: They are an extensible runtime scripting system for user-defined control.

Standard summary and detailed output reports: These are user-specific definable reports that have selectable time resolution ranging from annual to subhourly. All of these are equipped with energy source multipliers. The input data that has been entered by a user, based on the location of choice, provides the software with sufficient information to regulate and analyze parameters that would be necessary to build an energy-efficient structure.

In this study, the location selected for the simulation is Bhubaneswar, India. The weather file report was noted from a popular site that specializes in providing accurate weather report information about various cities within India. It can also be noted that Energy Plus has a few predefined reports on particular locations. For the input file, 5Zone Electric Baseboard was used to edit the entire file as per the specific requirements of the project, such as the location parameters, climate, lighting, internal gains, HVAC templates, fans, cooling, and other factors

Once these values have been entered into the launch application, the next step is to simulate the software, which would, in turn, provide the values of each parameter. The values obtained through the tables after the simulation can

be referred to, to comprehend and analyze the energy requirements to further increase the efficiency of the building. The necessary changes could be made based on the values obtained to improve the efficiency factor and comply with the ECBC standard. Several values including, but not limited to lighting, HVAC, and fans, were modified for the study to ensure that the building was ECBC compliant.

3.1. Parameter Setting for Energy Plus Software. The two most important parameters taken into consideration were the index file and the weather file. The latter was taken from the ISHRAE website for weather data of various Indian cities of India as mentioned earlier. The weather data is available free of cost and was accessed by providing some details of the user as shown in Figure 1. The downloaded zip file contains weather data in different formats, out of which a ".epw" file was selected to load in the weather file of the energy plus software.

3.2. Weather File Selection. The weather file of Bhubaneswar was downloaded from the abovementioned site and was implemented in the weather file section of the EP-Launch of Energy Plus. Some weather files were predefined and can be used depending on the location as shown in Figure 2.

3.3. EP-Launch. The input file used was an electric baseboard, where objects about the site location, average temperatures during different months of the year, and much more have been added. This was achieved with the help of the IDF Editor option that is present under the Input file selection option as shown in Figure 3.

3.4. Site Location Mapping. In this, important aspects of the Bhubaneswar city such as the longitude, latitude, elevation, and time zone were loaded. The values are specific for the city as shown in Figure 4 and can vary depending on the city in which the building is being constructed.

As in Figure 5, this parameter was updated as per the average temperature of the city in which the building is to be built.

3.5. Simulation in Energy Plus Software. Figure 6 provides the basics of the simulation carried out with the Energy Plus software. It includes parameters such as Run Period, Weather File, Latitude, Longitude, and Elevation of the site location. Table 1 provides details of the total area of the building on which the Energy Plus simulation was performed.

Table 2 provides details of the electricity usage of different utilities including cooling, lighting, fans, and pumps. The last row gives the total power requirement of the building. The objective of this study is to bring down the value as low as possible without hampering the perfect working conditions of the utility equipment.

3.6. Analysis of Results from Energy Plus

3.6.1. Cooling. In order to cool the building, energy-efficient air conditioners that have higher Energy Efficiency Ratio (EER) were used. These are higher BEE-rated air conditioners that give the same output with higher energy savings even with less power input. This resulted in 24.4% of power savings on the basis of power consumption as per ECBC compliance.

3.6.2. Interior Lighting. In order to make the building ECBC compliant, a shift from conventional lighting systems (Tube Lights, incandescent bulbs, CFL bulbs) to energy-efficient ones like the latest LED bulbs was recommended.

3.6.3. Interior Equipment. Fridge, washing machine, and television (TV) were taken into consideration, and the use of more energy-efficient equipment such as higher energy rated refrigerator and washing machine was recommended. Latest LED TVs rather than conventional LCD or old CRT TVs were also taken into consideration. A few other equipment such as charging adapters, calling bells, and water purifiers was left unchanged because of nonavailability of alternatives.

3.6.4. Fans. The conventional fans were replaced with fans that have BLDC or DC Motors or that are certified by Energy Star, as they tend to consume lower amounts of energy as compared to other ceiling fans. With proper selection of fans with BLDC or DC Motors, power savings up to 46.3% can be achieved.

3.6.5. Water Pumps. The sole purpose of the water pump is to pump water to the tanks. The working capability of the equipment was retained so as not to hamper the pumping process. Hence, it was decided to use the same prescribed power rated pump in Energy plus. However, this system does not converge under ECBC compliance.

3.6.6. Heat Rejection. Heat rejection refers to the process of acquiring excessive amount of heat from cooling a system and its elimination through a condenser or a cooler. It can also be defined as the combination of the work done by a compressor and the total heat energy that is transferred from the colder side to the warmer side. Hence, it implies that this process has a connection to the cooling utility. It was observed that the power saving in heat rejection accounts for about 27.3%.

4. Summary of Results

The results of the study performed on a 927 sq. ft. commercial building in Bhubaneshwar using Energy Plus software are summarized in this section. The results of the analysis carried out by considering the various class of electrical loads without tampering with its purpose/functionality in conventional building and ECBC compliant buildings are presented in Table 3. The table includes the

No.	Select	Station/Description	Type	WMO #	Complete/Incomplete	# of Records/ Month	Latitude	Longitude	Elevation	Time Zone	Price (USD)
1	☐	Ahmadabad	ISHRAE	426470	Complete	549	23.067	72.633	55	5.5	$0.00
2	☐	Akola	ISHRAE	429340	Complete	730	20.700	77.030	282	5.5	$0.00
3	☐	Allahabad-Bamhrauli	ISHRAE	424750	Complete	442	25.450	81.733	98	5.5	$0.00
4	☐	Amritsar	ISHRAE	420710	Complete	600	31.633	74.867	234	5.5	$0.00
5	☐	Aurangabad-Chikalth	ISHRAE	430140	Complete	437	19.850	75.400	579	5.5	$0.00

Figure 1: Web user interface of ISHRAE.

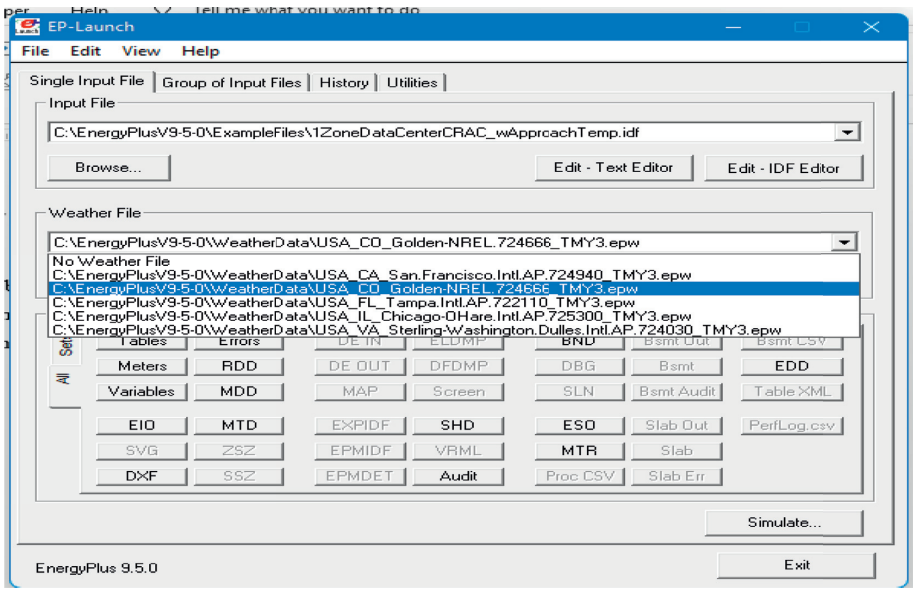

Figure 2: Datafile selection interface.

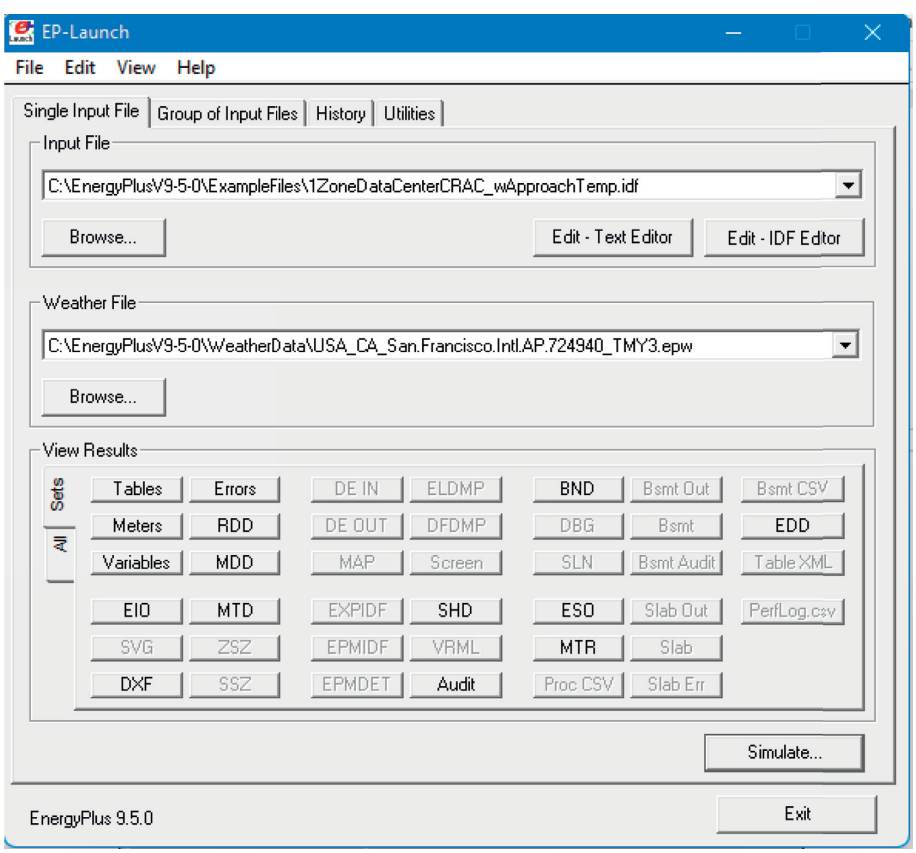

Figure 3: User interface of the Energy Plus software.

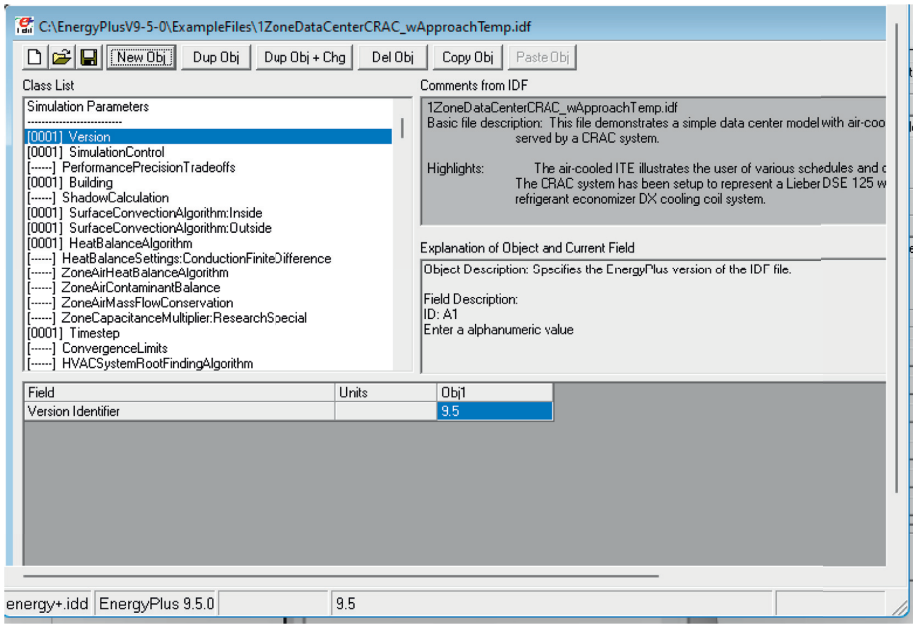

Figure 4: User interface of Energy Plus for location mapping.

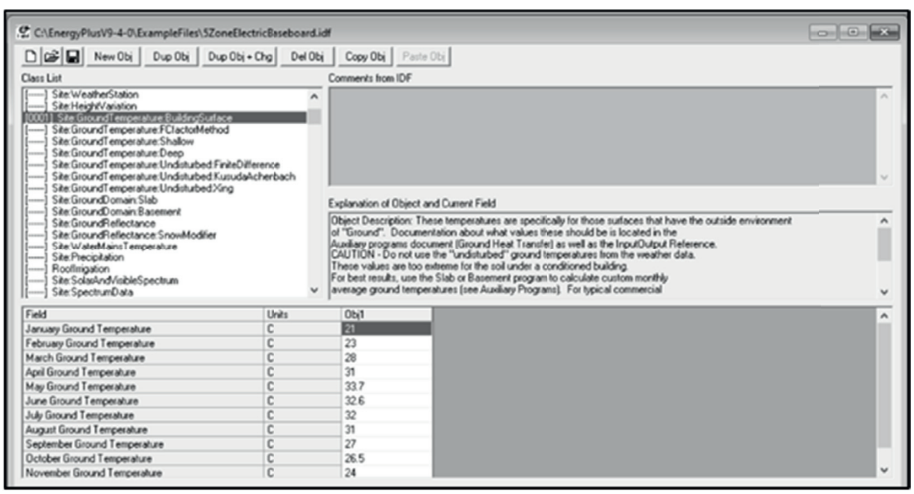

Figure 5: Selection and parameter feeding of site location.

General

	Value
Program Version and Build	Energy Plus, Version 9.4.0-998c4b76le, YMD=2020.11.07 19:24
RunPeriod	BHUBANESWAR INDIA ANNUAL COOLING 1% DESIGN CONDITIONS DB/MCWB HVAC Sizing Pass 1
Weather File	BHUBANESHWAR-IND ISHRAE2 WMO#=429710
Latitude [deg]	20.25
Longitude[deg]	85.83
Elevation [m]	46.00
Time Zone	5.50
North Axis Angle [deg]	20.00
Rotation for Appendix G [deg]	0.00
Hours Simulated [hrs]	744.00

Figure 6: Energy plus simulation parameter interface.

Table 1: Details of the building under study.

Building area	Area (m^2)
Total	927.20
Net conditioned	927.20
Unconditioned	0.00

Table 2: Details of power consumption by various loads in a day.

Nature of consumption	Power consumption in W (evaluated at the peak time of 11.30 on 21.04.2021)
Heating	0.0
Cooling	24957.01
Interior lighting	7500.00
Exterior lighting	0.00
Interior equipment	4500.00
Exterior equipment	0.00
Fans	4117.22
Pumps	1174.63
Humidification	0.00
Heat recovery	0.00
Water systems	0.00
Refrigeration	0.00
Generators	0.00
Total end usage	44013.01

Table 3: Comparison of power consumed by various loads without and with ECBC compliance.

Process	Power consumption without ECBC compliance in watts	Power consumption with ECBC compliance in watts	Power savings, % saving
Cooling	25000	18900	6,100.00 W, 24.4%
Interior lighting	7500	4500	3000.00 W, 40.0%
Interior equipment	4500	3700	800.00 W, 17.8%
Fans	4100	2200	1900.00 W, 46.3%
Pump	1850	1850	ECBC not applied
Heat rejections	1110	800	300.00 W, 27.3%
Total	44060	31950	12,110 W, 27.4%

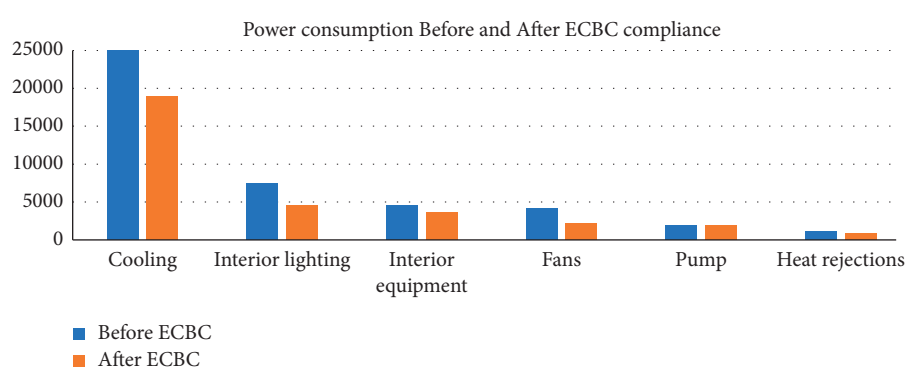

Figure 7: Comparison of power consumption by various category loads before and after incorporation of ECBC guidelines.

comparison between the power consumed by various classes of loads of similar output performance, with and without incorporation of ECBC guidelines and the resultant power savings achieved. The percentage power savings with the incorporation of ECBC are considerably high when compared to those of conventional loads with similar performance. The results of the study are pictorially represented in Figure 7, while Figure 8 provides the readers a clear insight

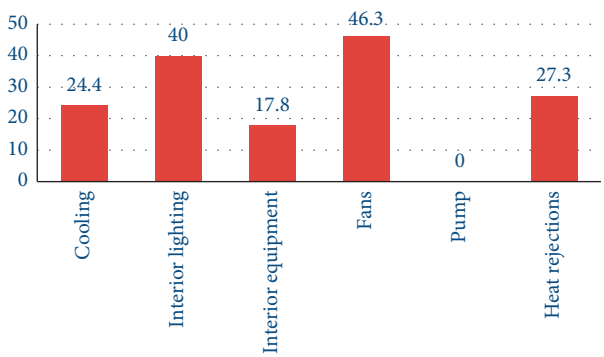

Figure 8: Percentage power savings achieved due to ECBC compliant electrical devices.

into the need for ECBC in developing energy-efficient buildings in the current scenario and for the future. Figure 7 details the power consumption of conventional loads against ECBC compliant electrical appliances performing a similar operation. Figure 8 shows the percentage saving of power consumption by each category of load. This aids the user to analyze and understand the behavior of ECBC compliant electrical loads and provides them with flexible choices to select appropriate electrical devices for their premises.

Table 3 reveals that the power consumed by each category of load equipment with the incorporation of the ECBC guidelines resulted in greater power savings and hence reduction in the energy requirements of the building. Equipping the upcoming constructions with different categories of utilities such as fans, cooling, and lighting that comply with the ECBC guidelines enhances the operation cost savings, in addition to minimal increment in the investment cost. The total power savings percentage against every utility that was set up following ECBC is a rough average of the individual power savings of each utility. In this study, an appreciable power saving of 27.4% was obtained by revamping the conventional load equipment with modern ECBC compliant appliances without affecting the performance as in the conventional utilities.

5. Conclusion

A major criterion that is required to upgrade a building to ECBC standard is the energy-saving rate. For an ECBC building, the minimum energy savings should be 25%, while those for ECBC plus should at least be 35%, and those for Super-ECBC should be 50% and above. In this work, energy conservation measures were employed by taking into consideration the electrical appliances only. The civil structure of the building, materials, or other kinds of thermal radiation measures have been considered to make the building energy-efficient. The simulated building with a total built-up area of 927 m^2 situated in Bhubaneswar with its unique climatic conditions has recorded energy savings up to 27.4%, which brings it into the respectable ECBC compliant buildings list. The levels of impact of ECBC are highly dependent on the effectiveness of its enforcement and compliance. The energy savings can still be improved through structural modification by utilizing natural lighting for the interiors, thus paving way for reducing the number of lights to be installed. The present-day market scenario has recorded a rise in new buildings that are being constructed following the ECBC code utilizing natural energy sources for lighting, heating, and ventilation purposes. Similar changes are being made to older buildings to ensure that they meet the ECBC standards.

Data Availability

The data used to support the findings of this study are included in the article. Should further data or information be required, these are available from the corresponding author upon request.

Disclosure

It was performed as a part of the Employment of Mettu University, Ethiopia.

Conflicts of Interest

The authors declare that there are no conflicts of interest regarding the publication of this paper.

Acknowledgments

The authors thank Vellore Institute of Technology, Chennai, and Saveetha School of Engineering, SIMATS, Chennai, for the technical assistance. The authors appreciate the supports from Mettu University, Ethiopia.

References

[1] S. Shetty, P. Kishore, P. Kini, R. R. Acharya, and A. Raj, "Energy Conservation Building Code (ECBC) based optimum wall composition with respect to thermal transmittance and thickness for different commercial pockets of Tier-1 city in temperate climatic zone of India," *Procedia Manufacturing*, vol. 44, pp. 229–236, 2020.

[2] S. Han, R. Yao, and N. Li, "The development of energy conservation policy of buildings in China: a comprehensive review and analysis," *Journal of Building Engineering*, vol. 38, Article ID 102229, 2021.

[3] European Commission, *Evaluation of the Energy Performance of Buildings Directive 2010/31/EU*, European Commission, UK, 2015.

[4] D. Khovalyg, O. B. Kazanci, H. Halvorsen et al., "Critical review of standards for indoor thermal environment and air quality," *Energy and Buildings*, vol. 213, Article ID 109819, 2020.

[5] X. Guan, Z. Xu, and Q. S. Jia, "Energy-efficient buildings facilitated by microgrid," *IEEE Transactions on Smart Grid*, vol. 1, no. 3, pp. 243–252, 2010.

[6] J. Pan, R. Jain, S. Paul, T. Vu, A. Saifullah, and M. Sha, "An internet of things framework for smart energy in buildings: designs, prototype, and experiments," *IEEE Internet of Things Journal*, vol. 2, no. 6, pp. 527–537, 2015.

[7] R. Bointner and Electric Drives, "Energy efficient design in shopping centres – a pathway towards lower energy consumption," in *Proceeding of the 2016 2nd International*

Conference on Intelligent Green Building and Smart Grid (IGBSG), vol. 5–9, Prague, Czech Republic, 2016.

[8] W. O'Brien, F. Tahmasebi, R. K. Andersen et al., "An international review of occupant-related aspects of building energy codes and standards," *Building and Environment*, vol. 179, Article ID 106906, 2020.

[9] K. Amasyali, N. M. El-Gohary, and El-Gohary, "Energy-related values and satisfaction levels of residential and office building occupants," *Building and Environment*, vol. 95, pp. 251–263, 2016.

[10] P. Zhou and N. El-Gohary, "Ontology-based automated information extraction from building energy conservation codes," *Automation in Construction*, vol. 74, pp. 103–117, 2017.

[11] A. Gillespie, T. F. Xulu, S. Simplice Igor, N. noubissie tientcheu, and S. P. D. Chowdhury, "Building Design Considerations for an Energy-Efficient HVAC System," in *Proceeding of the 2018 IEEE PES/IAS PowerAfrica*, pp. 919–924, June 2018, https://doi.org/10.1109/PowerAfrica.2018.8520995.

[12] V. Ion and M. Macedon, "Energy-efficient built environment of the RD Institute of the transilvania university of brasov Romania," in *Proceeding of the 2020 7th International Conference on Energy Efficiency and Agricultural Engineering, EE and AE 2020 - Proceedings*, pp. 12–15, IEEE, Prague, Czech Republic, November (2020), https://doi.org/10.1109/EEAE49144.2020.9279027.

[13] D. Romanchuk, E. Nyholm, M. Odenberger, and F. Johnsson, "Balancing investments in building energy conservation measures with investments in district heating–a Swedish case study," *Energy and Buildings*, vol. 226, Article ID 110353, 2020.

[14] S. Yu, Q. Tan, M. Evans, P. Kyle, L. Vu, and P. L. Patel, "Improving building energy efficiency in India: state-level analysis of building energy efficiency policies," *Energy Policy*, vol. 110, pp. 331–341, 2017.

[15] Y.-H. Lin, M.-D. Lin, K.-T. Tsai, M.-J. Deng, and H. Ishii, "Multi-objective optimization design of green building envelopes and air conditioning systems for energy conservation and CO2 emission reduction," *Sustainable Cities and Society*, vol. 64, Article ID 102555, 2021.

[16] A. Arul Marcel Moshi, S. Guruvasanth, P. M. Samuel, and S. S. Billigraham, "Effective techniques for energy conservation in buildings - a comprehensive review," *Materials Today: Proceedings*, vol. 45, pp. 535–539, 2021.

[17] I. Yarbrough, Q. Sun, D. C. Reeves, K. Hackman, R. Bennett, and D. S. Henshel, "Visualizing building energy demand for building peak energy analysis," *Energy and Buildings*, vol. 91, pp. 10–15, 2015.

[18] S. Walker, W. Khan, K. Katic, W. Maassen, and W. Zeiler, "Accuracy of different machine learning algorithms and added-value of predicting aggregated-level energy performance of commercial buildings," *Energy and Buildings*, vol. 209, Article ID 109705, 2020.

[19] A. C. Menezes, A. Cripps, R. A. Buswell, J. Wright, and D. Bouchlaghem, "Estimating the energy consumption and power demand of small power equipment in office buildings," *Energy and Buildings*, vol. 75, pp. 199–209, 2014.

[20] N. Kouvelas and R. V. Prasad, "Efficient allocation of harvested energy at the edge by building a tangible micro-grid-the Texas case," *IEEE Transactions on Green Communications and Networking*, vol. 5, no. 1, pp. 94–105, 2021.

[21] M. Bhatnagar, J. Mathur, and V. Garg, "Development of reference building models for India," *Journal of Building Engineering*, vol. 21, pp. 267–277, 2019.

[22] K. Hemalatha, C. James, L. Natrayan, and V. Swamynadh, "Analysis of RCC T-beam and prestressed concrete box girder bridges super structure under different span conditions," *Materials Today: Proceedings*, vol. 37, no. 2, pp. 1507–1516, 2021.

Hindawi
Advances in Civil Engineering
Volume 2021, Article ID 5693101, 11 pages
https://doi.org/10.1155/2021/5693101

Research Article

Reduction of Embodied Energy and Construction Cost of Affordable Houses through Efficient Architectural Design: A Case Study in Indian Scenario

Deepak Bansal,[1] **V. K. Minocha**,[2] **Arvinder Kaur**,[3] **Vaidehi A. Dakwale**,[4] **and R. V. Ralegaonkar**[4]

[1]*GGSIP University Delhi 110075, India & Joint General Manager with Housing and Urban Development Corporation Limited (HUDCO), New Delhi 110003, India*
[2]*Delhi Technological University, New Delhi 110042, India*
[3]*GGSIP University, New Delhi 110075, India*
[4]*Civil Engineering Department, VNIT, Nagpur 440010, Maharashtra, India*

Correspondence should be addressed to Deepak Bansal; dbansalindia@gmail.com

Received 9 July 2021; Revised 20 August 2021; Accepted 31 August 2021; Published 9 September 2021

Academic Editor: Amos Darko

Embodied energy and cost of construction of any building depends upon the consumption of resources, more specifically construction materials. In housing clusters, the spaces provided for horizontal and vertical circulation of occupants such as corridors and contribute in the built-up area of individual unit without any increase in the usable/carpet area. Thus, an efficient architectural planning of common circulation spaces plays a major role in lowering the built-up-to-carpet area ratio of individual housing unit in clusters. This may, thus, result in lesser embodied energy and maximum area availability for occupant usage. In the present study, 30 clusters of Indian affordable housing units (IAHUs) of similar typology and different architectural designs are analyzed. The built-up and carpet area of each IAHU are estimated, and the ratio of the built-up to carpet area is calculated. Detailed estimates of construction materials for each IAHU is prepared, and cost of construction and embodied energy is calculated. The calculations of embodied energy and construction cost are done for major construction materials, viz., cement, steel, bricks, sand, and coarse aggregate and compared with different built-up-to-carpet area ratio. The study of IAHUs concludes that a variation of 1.30 to 1.62 in the built-up area-to-carpet area ratio results in variation in construction cost (INR 13,425.00 to 20,138.00 per m^2 carpet area) and embodied energy (4–6.5 GJ per m^2 carpet area). Analysis suggests that the IAHU with a lower built-up-to-carpet area ratio exhibits reduction in the cost of construction and embodied energy simultaneously. Thus, an efficient architectural design plays a major role in improving the sustainability of IAHUs and built-up-to-carpet area ratio is an important indicator of sustainability.

1. Introduction

Life cycle energy of buildings is associated with different phases of buildings, which includes embodied energy (EE), operating energy (OE), and energy required for demolition and disposal. Of these, major phases of energy consumption are construction or preoccupancy phase (EE) and operational or occupancy phase (OE) [1–10]. EE of the buildings is the sum of all energy incurred on sourcing, procession/manufacturing of building materials, and transportation of building materials including construction equipment and labor, energy incurred for onsite construction, and all secondary and tertiary process. Life cycle energy of buildings due to demolition, disposal, and transportation of material and use of construction equipment is very less, that is, 1-2% [11–14] and 0.7% [15–17], respectively. The energy in construction activities is negligible due to the predominance of manual labor in Asia [12, 13, 16, 18].

Furthermore, the energy usage pattern in buildings depends on many factors. Low-rise and high-rise buildings, load bearing, RCC framed structures or hybrid construction, building use, buildings with different construction materials/envelopes/typologies, and so on, have different patterns of energy consumption during its lifetime [16, 19, 20]. In conventional buildings, OE is more predominant, whereas in energy efficient buildings, EE becomes significant [2, 15, 21–29]. There are two approaches for reduction of EE of any building: first, using low embodied energy construction material and second, by material resource conservation. The material resource load can be expressed as quantity of material used per unit of area. In housing clusters, the built-up area of an individual house is the addition of its own carpet area, external wall area in plan, and proportionate built-up area derived from common spaces and utilities. The utilities may be lifts, staircases, corridors, and so on. The houses intended for economically weaker sections (EWSs) have a low built-up area, and thus, material resource conservation becomes crucial for reducing its EE. Construction materials, which have high embodied energy and high cost, are used minimally in housing for economically weaker sections [3, 7, 12, 28, 29], further reducing its embodied energy (EE), life cycle energy (LCE), and construction cost (CC).

In India, Pradhan Mantri Awas Yojna (PMAY) [30] is an ambitious social housing scheme carried out by Government of India and is being implemented by its Ministry of Housing and Urban Affairs (MoHUA) for providing affordable housing with basic amenities to the masses on pan-India basis. This mission addresses housing shortages among the economically weaker sections (EWS) including slum dwellers by ensuring a permanent house to all eligible households. The mission supports construction of houses of about 30–60 m^2 carpet area with basic civic infrastructure for the EWS population.

The requirement of OE in IAHUs is limited due to the inability to afford heating and cooling systems due to financial issues of the stakeholders. In this scenario, EE becomes more significant for improving sustainability index of the Indian affordable housing [3, 7, 9, 12, 30, 31]. Life cycle energy (LCE) of a building is expressed as energy consumed per unit area. In this expression, the denominator may be either the built-up area or carpet area. Therefore, any building may have two boundary values of LCE: higher limiting value with carpet area and lower limiting value with built-up area, unless the built-up and carpet areas are equal. Since the carpet area is the actual usable area available to occupants, the LCE value with the carpet area in the denominator becomes significant. Thus, the LCE values reported with the built-up area in the denominator may give a false interpretation of lower embodied energy or LCE of the buildings. In other words, the ratio of the built-up to carpet area is a major indicator in expressing the embodied energy and cost indexes in sustainable buildings. This indicator becomes even crucial in buildings, where energy efficiency is defined by primarily construction material conservation, such as housing for EWS. Efficient architectural design and judicious planning of common circulation areas and other spaces in buildings help to reduce requirement of construction materials, thus reducing EE and CC. The present paper investigates the effect of the built-up-to-carpet area ratio on EE and CC by analyzing 30 case studies of housing for the EWS in the Indian scenario.

2. Literature Review

In literature, life cycle energy analysis (LCEA) for different types of buildings has been carried out and values of LCE, EE, OE, and CC are reported for per unit area of the buildings [2–9, 16, 19, 20, 32–37]. The prescribed LCA/LCEA values in the literature may vary too much due to different system boundaries and typologies of the buildings, and thus, it is reflected in the energy footprint per m^2 of area [8, 13, 23, 26, 37]. The type of structures (framed/load bearing/hybrid) [28], height [29], occupancy type (Apartment/individual/population), circulation spaces, built-up area [38], etc., have different requirement of construction materials. Reducing wall thickness and designing circulation spaces efficiently will not only increase the carpet area of the building but also reduce demand of construction materials, which, in turn, reduces CC and EE of the buildings. It has been observed in literature that while reporting LCE values, the ratio of the built-up area and carpet area varies from 1 to 1.45.

Pacheco-Torres et al. [39] analyzed a three-storey house in Spain with a built-up area of 313.13 m^2 and total carpet area as 260.86 m^2. The results were reported on an energy per unit area basis taking the built-up area in the denominator. Paulsen and Sposto [4] analyzed houses with mass in Brazil for an area of 48 m^2; however, as per available drawings, the carpet area is 43.40 m^2. This is 1.10 times higher than the carpet area. Das [32] have analyzed housing complexes in India for energy conservation, with apartments of different built-up areas. However, the author assumed that the same set of staircases and lifts can be fitted into any design, which may not be correct. Pinky Devi and Palaniappan [3] have analyzed an affordable, single-storey house in India with an area of 32.5 m^2, but as per architectural drawings, the carpet area is 22.32 m^2, resulting in a ratio of 1.45. Oyarzo and Peuportier [33] have analyzed houses in Chile, with an area of 32 m^2, a carpet area of 32 m^2 as per drawings, and the ratio as 1. Embodied energy values of low-rise Indian affordable housing have been compiled by Bansal et al., [20] as 1.6–5.0 GJ/sqm of plinth area.

EE can also be reduced using alternative construction materials and physical planning. Bansal et al. [7] & Stephan and Athanassiadis, [40]. Antonín et al. [41] have studied strategies for reducing embodied energy and CO_2 emission through efficient designing building elements, structural system, and passive systems of houses. Vukotic et al., [42] have presented ways for optimization of energy in different stages of building, primarily by construction materials. Worth et al. [43] have optimized a roofing system based on EE and cost.

From the literature, it has been observed that as the height of buildings increases, the circulation space requirement increases, thus increasing the built-up-to-carpet

area ratio. Bansal et al., [44] carried out a study to find the variation in the carpet area and built-up area for different heights of buildings from single storied to 30 storied and found that for the same carpet area, built-up areas increased from 32% to 148% as the height of the building increases [20, 44]. The results are presented in Figures 1(a) and 1(b) below. The increase is visualized due to the increase in provision of floor area for circulation spaces for staircases, lifts, elevator, and so on in high-rise buildings.

However, in the studied literature, the discussion on change in LCE, EE, and CC values due to difference in the built-up-to-carpet area ratio is not highlighted. Thus, an integrated approach toward reducing EE and CC of a building design efficiency in terms of the built-up area-to-carpet area ratio is not addressed in past studies. In the present study, authors investigate the effect of the built-up-to-carpet area ratio on EE and CC of buildings specifically for EWS housing projects. Thirty buildings from Indian affordable housing units (IAHU) are identified and analyzed. Buildings are analyzed for their architectural design-based design efficiency in terms of the built-up area-to-carpet area ratio. EE and CCs have been calculated per m^2 of built-up and carpet areas to choose the optimum architectural design with the least EE and CC. This will provide an integrated approach to designers about the design efficiency of architectural designs, in terms of EE and CC, based on the ratio of the built-up to carpet area. The design efficiency of architectural design will help in analyzing sustainable buildings by the finding optimum range of ratio of built-up–carpet area that will result in minimum construction cost and embodied energy.

3. Methodology

In the present study, 30 representative Indian affordable housing units (IAHU) from PMAY have been selected for this case study. These buildings have been designed according to the guidelines of PMAY and the technical specifications of National Building Code of India (NBC) [45] and are located in different parts of country. These 30 IAHUs have ground plus two storeys with a load-bearing structure. Each IHAU is designed as cluster consisting of 2 to 12 apartments per storey. The service life of buildings in India is about 50 years [28, 31]. The plan for a typical IAHU is presented in Figure 2. Table 1 presents specifications of IAHU. While designing the IAHU, the safe bearing capacity of soil is taken as 11 MT/m^2 at 1.0 metre depth from natural ground level, seismic zone III, and basic wind speed 47 m/s as per the NBC.

The architectural plan in terms of length of walls, openings, arrangement of rooms, and provision of common spaces in a cluster play a major role in building construction. For the same built-up area, if the number of internal walls or the area of staircases, corridors, and so on increases, the effective or usable area (carpet area) will reduce and vice versa. This change is reflected in the consumption of construction materials or bills of quantity as well. The quantity of construction material thus varies per unit of the built-up/carpet area in different architectural designs due to the different arrangement of walls and spaces. Since reinforcing steel, cement, fired clay bricks, sand, and coarse aggregates are the main contributors in construction cost (CC) and embodied energy (EE) [46–48]; any change in the quantities of these construction materials is reflected positively or negatively in CC and EE. Thus, an efficient design may lead to reduction in CC and EE, and the built-up area-to-carpet area ratio plays a significant role in the overall CC and EE of buildings. Figure 3 indicates the interrelation of these parameters.

The present study investigates and quantifies effect of the built-up area-to-carpet area ratio on CC and EE of 30 case study IAHUs. The IAHUs are designated as A1 to A30 and arranged in the ascending order of the built-up area in Table 2, which presents the built-up area and carpet area values of the selected IAHU. As evident, the built-up area-to-carpet area ratio changes from 1.30 to 1.62 due to the change in architectural design.

The bill of quantities for the IAHU in this study has been prepared. Since cost estimates prepared by government agencies are based on the schedule of rates published by the Central Public Works Department (CPWD) and Delhi scheduled Rates (DSRs) 2016 [49], the cost of construction materials is adopted from these publications and presented in Table 3.

Similarly, the EE value for 30 IAHUs based on major construction material consumption was calculated. Since the embodied energy of a material depends on a variety of factors such as raw material (local/imported), processing (manual/mechanical), transportation, and so on [50–52], the embodied energy values have been taken from the Indian scenario [9, 50, 52, 53] as well as international sources [54]. These values are presented and compared in Table 4. These values show large variations, which is primarily due to the factors discussed earlier. To represent the local condition, in this study, the EE values from the Indian scenario are considered for the calculation of EE of the case study IAHU.

4. Results and Discussion

Construction materials are major contributors to CC and EE in any building construction. In the present study, the bill of quantity for each IAHU is tabulated and the cost of construction is calculated based on consumption of construction materials. Cost of construction includes materials, labor, electrical, plumbing, and so on completely. As per the CPWD 2016 [55], the cost of construction materials is about 36%, cost of labor is 30%, PHE/electrical works is 7%, hire charges of tool and plants, consumables and miscellaneous is 12%, and contractor profit is taken as 15%, making a total of 100%. Table 5 presents a summary of cost of construction for 30 IAHUs and indicates that the cost of construction varies between INR 13,425.00 to 20,138.00 per m^2 of carpet area. It is seen from Table 4 that the built-up area varies from 1.30 to 1.62 of carpet area due to different architectural designs with the same specifications and the same functional requirements. This is reflected in the construction cost of the IAHU.

The total cost of major construction materials such as fired clay bricks, cement, steel, sand, and aggregates is

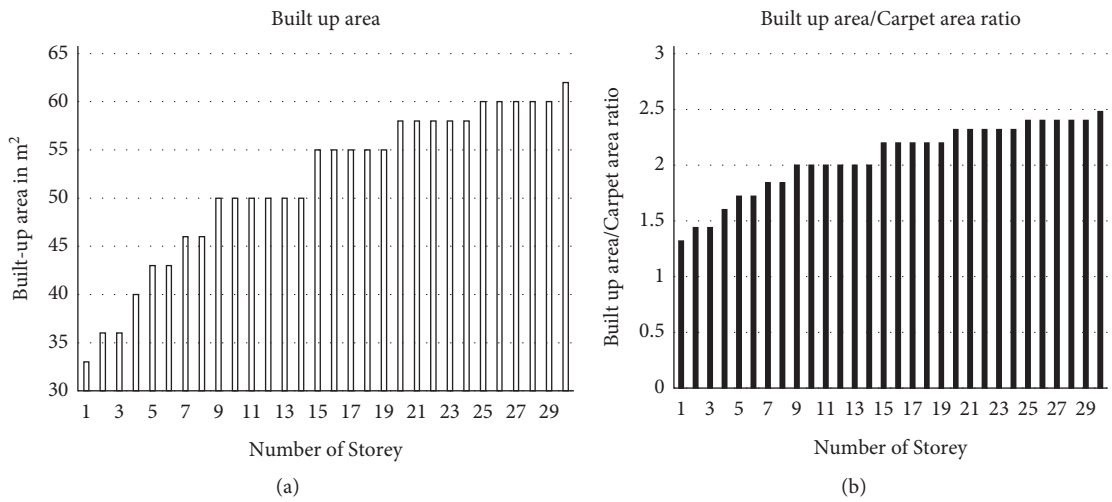

Figure 1: Table showing relation between number of storey and built up area, carpet area.

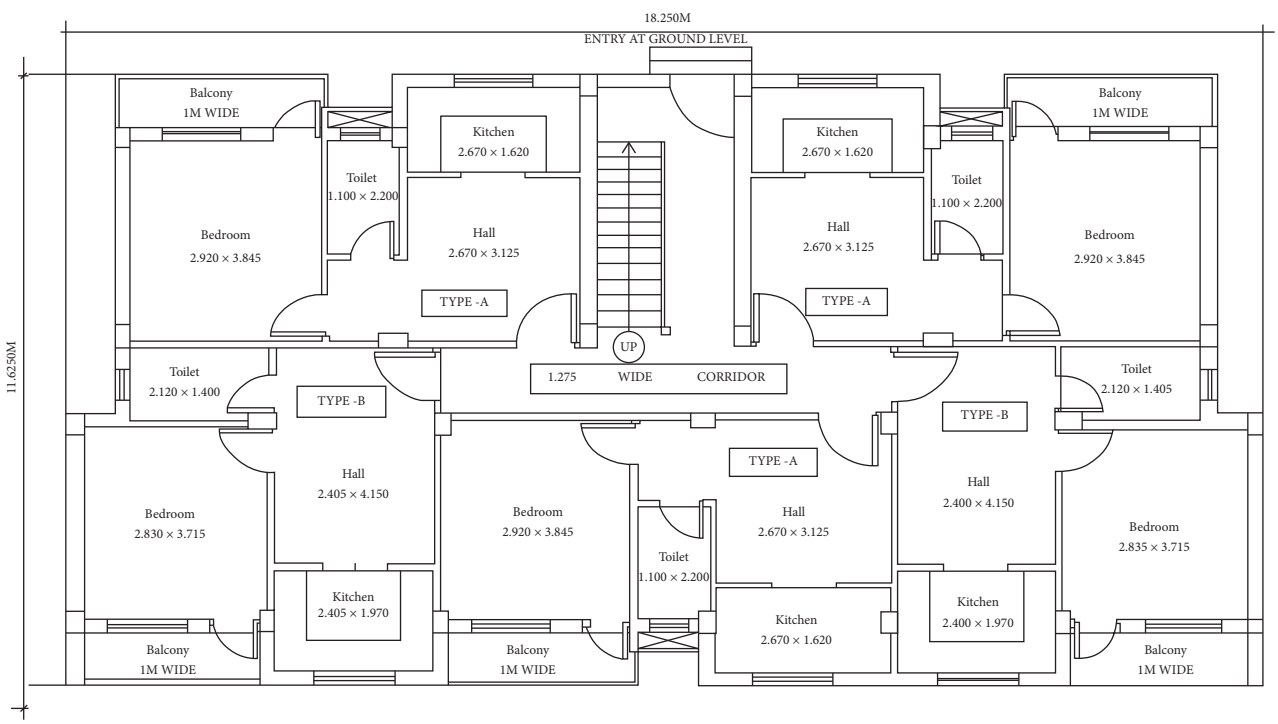

Figure 2: Typical architectural design of an IAHU [30].

calculated from the bill of quantities for each IAHU and is tabulated in Table 6 with the per unit carpet area. It is also observed that cement, sand, aggregate, steel, and brick together account for 35%–38% of the total cost of construction that varies from INR 4,697.00 to 7,433.00 per m^2 on the carpet area basis with brick as the major contributor. It is evident from Table 6 that in the load-bearing structure, brick, cement, and steel contribution is in the descending order of the total cost of building. Thus, reducing consumption of these construction materials reduces the overall cost of construction.

Similarly, EE of major construction materials has been calculated and presented in Table 7. For calculation of embodied energy, the average values of EE indicated in Table 4, for respective construction materials has been used. It is observed that fired clay bricks are major contributors in the total EE of IAHUs. Thus, a good architectural design with lesser volume of main and interior walls plays a major role in reducing EE of the IAHU.

From the results, it is observed that the minimum cost of construction and EE is corresponding to built-up-to-carpet area ratio 1.31 for IAHU, which is design no. A22 and the

Table 1: Specifications of the chosen Indian affordable housing [44].

S. no.	Component	Details
1	Structure	Load-bearing structure
2	Wall	230 mm thick brick masonry in mortar with cement and coarse sand in 1 6 proportion
3	Roof	115 mm thick flat reinforced cement concrete (RCC) roof with concrete of M25 grade and with TMT Fe 500D grade reinforcement, 1% by volume of RCC
4	Flooring	40 mm thick plain cement concrete (PCC) of M15 grade
5	Skirting/dado	12 mm thick 100 mm/1200 mm high, in mortar with cement and coarse sand in 1 6 proportion
6	Plaster/rendering	12/15 mm thick with in mortar with cement and coarse sand in 1 6 proportion
7	Terrace finishing	100 mm average with brick tiles and mud fuska (treatment with local clay and mud to reduce radiant heat gain)
8	Parapet	900 mm high in 115 mm thick brick masonry in mortar with cement and coarse sand in 1 4 proportion
9	Joinery	Mild steel frames with steel grills and glass panels
10	CC gola/khurrah/ coping	CC gola (over the deck treatment at junction of parapet wall and roof slab to prevent seepage) in PCC of M15 grade Khurrah (rainwater spout) Coping (PCC over parapets to protect it from rainwater)

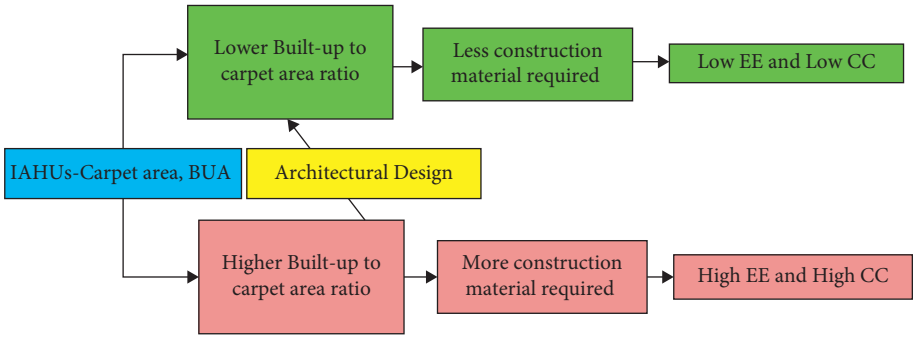

Figure 3: Interrelation of the construction area, built-up area-to-carpet area ratio, construction cost, and embodied energy.

Table 2: Carpet area, built-up area, and built-up-to-carpet area ratio for selected 30 IAHUs.

IAHU	Built-up area (m^2)	Area occupied by common amenities and external walls	Carpet area (m^2)	Built-up area-to-carpet area ratio
A1	28.47	8.45	20.02	1.42
A2	30.50	9.71	20.79	1.47
A3	30.81	7.78	23.03	1.34
A4	31.63	9.09	22.54	1.40
A5	31.64	9.15	22.49	1.41
A6	32.56	9.89	22.67	1.44
A7	32.84	10.36	22.48	1.46
A8	33.27	9.21	24.06	1.38
A9	33.71	11.25	22.46	1.50
A10	33.77	11.83	21.94	1.54
A11	33.90	11.52	22.38	1.51
A12	34.11	10.72	23.39	1.46
A13	34.14	7.82	26.32	1.30
A14	34.25	8.99	25.26	1.36
A15	34.68	12.25	22.43	1.55
A16	34.94	13.40	21.54	1.62
A17	34.98	12.59	22.39	1.56
A18	35.32	8.84	26.48	1.33
A19	35.70	9.87	25.83	1.38
A20	36.34	10.88	25.46	1.43
A21	36.97	11.36	25.61	1.44
A22	37.05	8.71	28.34	1.31

Table 2: Continued.

IAHU	Built-up area (m^2)	Area occupied by common amenities and external walls	Carpet area (m^2)	Built-up area-to-carpet area ratio
A23	37.31	12.02	25.29	1.48
A24	39.20	13.30	25.90	1.51
A25	40.52	10.53	29.99	1.35
A26	40.76	11.83	28.93	1.41
A27	40.80	11.37	29.43	1.39
A28	40.82	12.04	28.78	1.42
A29	41.58	13.18	28.40	1.46
A30	42.06	14.73	27.33	1.54

Table 3: Cost of common construction materials [50].

Items	Cement	Steel	Bricks	Sand	Coarse aggregate
Unit	Bag of 50 kg	kg	Per number	m^3	m^3
Cost in INR	285.00	37.30	5.20	1200.00	1300.00

Table 4: Embodied energies of construction materials [9, 46–48, 51].

S. no.	Item	Embodied energy (MJ/kg)		% change in international to Indian scenario (%)
		Indian scenario	International source	
1	Cement	5.9–7.8 (avg. 6.85)	4.5	−34
2	Fine aggregate	0.1–0.2 (avg. 0.15)	0.83	+453
3	Coarse aggregates	0.4	0.83	+107
4	Reinforcement steel	28.2–42 (avg. 35.1)	17.4	−50
5	Burnt clay bricks (weight of brick 2.6 kg/no's)	1.8	3	+66
6	Lime wash	5.65	5.3	−6
7	Woodwork	7.2	10	+38
8	Copper wire	110	36	−67
9	PVC conduit	104–108 (avg. 106)	67.5	−36

Table 5: Built-up-to-carpet area ratio and construction cost for selected 30 IAHUs.

IAHU	Built-up-to-carpet area ratio	Construction cost per unit carpet area (INR)	Construction cost per unit built-up area (INR)
A1	1.42	16958.97	24113.59
A2	1.47	16852.84	24723.98
A3	1.34	17260.68	23091.69
A4	1.40	17222.26	24167.70
A5	1.41	17012.15	23933.49
A6	1.44	16485.14	23676.94
A7	1.46	16611.51	24267.00
A8	1.38	15361.28	21241.48
A9	1.50	17537.10	26321.27
A10	1.54	19096.25	29392.91
A11	1.51	20138.31	30504.41
A12	1.46	16362.00	23860.97
A13	1.30	15155.91	19658.34
A14	1.36	14491.13	19648.50
A15	1.55	18918.65	29250.95
A16	1.62	18666.13	30278.30
A17	1.56	19558.89	30559.67
A18	1.33	15910.67	21222.24
A19	1.38	17044.65	23557.65

Table 5: Continued.

IAHU	Built-up-to-carpet area ratio	Construction cost per unit carpet area (INR)	Construction cost per unit built-up area (INR)
A20	1.43	16784.81	23957.58
A21	1.44	16293.65	23521.14
A22	1.31	13425.83	17552.11
A23	1.48	15248.91	22496.51
A24	1.51	18685.40	28270.77
A25	1.35	14110.41	19064.82
A26	1.41	15329.75	21598.36
A27	1.39	16209.59	22472.01
A28	1.42	15634.69	22175.40
A29	1.46	16458.23	24096.25
A30	1.54	18099.73	27854.91

Table 6: Cost of major construction materials for selected 30 IAHUs in INR.

IAHU	Cement a	Steel b	Bricks c	Sand d	Aggregate e	Total cost a+b + c + d + e	Percent of total cost of an IAHU
A1	1499.1	1140.26	1980.83	681.6	494.77	5796.57	34
A2	1499.1	1147.72	2021.96	682.4	507.40	5858.59	35
A3	1556.1	1163.01	2272.6.0	725.6	486.59	6203.92	36
A4	1556.1	1180.91	2202.72	716.8	501.45	6158.00	36
A5	1539.0	1176.81	2146.19	704.8	500.71	6067.53	36
A6	1487.7	1113.77	2030.28	680.8	499.22	5811.79	35
A7	1487.7	1117.88	2094.09	684.8	499.97	5884.44	35
A8	1390.8	1086.92	1856.29	628.0	470.25	5432.27	35
A9	1601.7	1217.84	2147.34	727.2	530.43	6224.52	35
A10	1670.1	1228.28	2776.02	808.8	523.74	7006.95	37
A11	1812.6	1424.11	2785.84	846.4	563.86	7432.82	37
A12	1476.3	1099.6	2067.2	679.2	496.25	5818.57	36
A13	1402.2	1055.96	1847.92	632.8	458.36	5397.26	36
A14	1316.7	1042.53	1684.02	589.6	456.88	5089.74	35
A15	1664.4	1253.65	2682.26	796.0	526.71	6923.03	37
A16	1641.6	1253.65	2584.45	780.8	535.63	6796.14	36
A17	1761.3	1396.51	2624.8	818.4	560.88	7161.91	37
A18	1459.2	1053.35	2077.08	675.2	473.22	5738.07	36
A19	1556.1	1134.66	2374.84	732.8	487.34	6285.75	37
A20	1527.6	1146.97	2215.09	709.6	494.77	6094.04	36
A21	1493.4	1076.47	2160.49	693.6	491.05	5915.03	36
A22	1254.0	969.42	1481.01	548.8	443.51	4696.75	35
A23	1419.3	1062.67	1753.38	632	493.28	5360.65	35
A24	1704.3	1164.87	2800.51	824.8	523.74	7018.24	38
A25	1328.1	980.61	1683.81	595.2	454.65	5042.38	36
A26	1413.6	1083.93	1964.09	646.4	475.45	5583.49	36
A27	1527.6	1049.24	2245.82	713.6	484.37	6020.65	37
A28	1447.8	1021.64	2092.01	674.4	473.97	5709.83	37
A29	1533.3	1170.1	2187.06	704.0	506.65	6101.13	37
A30	1767.0	1211.5	2637.28	805.6	557.91	6979.31	39

maximum ratio1.51 for IAHU, which is design no. A11. Design no. A17 with built-up area-to-carpet area ratio of 1.56 is very close to design no. A11.

Figure 4 makes it clear that design A22 is the most efficient design with cost of construction materials as INR 4,697 per m^2, cost of construction INR 13,425 per m^2 and embodied energy of 4.0 GJ per m^2 and design A11 (with built-up-to-carpet area ratio 1.51) is the most inefficient design with cost of construction materials as 7,433.00 per m^2, construction cost as INR 20,138.00 per m^2, and embodied energy as 6.5 GJ per m^2.

This study shows that the construction cost, cost of major construction materials, and EE are directly proportional to the built-up-to-carpet area ratio. The more the ratio, the more inefficient design would be. The cost of construction materials varies from INR 4,697.00 to 7,433.00 per m^2 of carpet area, which is about 35%–37% of construction cost per sqm of carpet area. It is seen from this study that architectural designs have a major bearing on construction cost and embodied energy of the buildings; as in an architectural design, spaces are arranged in a particular way, which results in different placement of walls and

Table 7: EE of major construction materials for selected 30 IAHUs in MJ/m^2 of the carpet area.

IAHU	Cement a	Steel b	Bricks c	Sand d	Aggregates e	Total EE a+b + c + d + e
A1	1801.55	1073.01	1790.37	127.80	266.40	5059.13
A2	1801.55	1080.03	1827.55	127.95	273.20	5110.28
A3	1870.05	1094.42	2054.09	136.05	262.00	5416.61
A4	1870.05	1111.27	1990.92	134.40	270.00	5376.64
A5	1849.50	1107.41	1939.83	132.15	269.60	5298.49
A6	1787.85	1048.09	1835.07	127.65	268.80	5067.45
A7	1787.85	1051.95	1892.74	128.40	269.20	5130.13
A8	1671.40	1022.81	1677.81	117.75	253.20	4742.97
A9	1924.85	1146.02	1940.87	136.35	285.60	5433.68
A10	2007.05	1155.84	2509.10	151.65	282.00	6105.64
A11	2178.30	1340.12	2517.98	158.70	303.60	6498.70
A12	1774.15	1034.75	1868.44	127.35	267.20	5071.89
A13	1685.10	993.68	1670.24	118.65	246.80	4714.47
A14	1582.35	981.05	1522.10	110.55	246.00	4442.04
A15	2000.20	1179.71	2424.35	149.25	283.60	6037.12
A16	1972.80	1179.71	2335.95	146.40	288.40	5923.26
A17	2116.65	1314.14	2372.42	153.45	302.00	6258.66
A18	1753.60	991.22	1877.37	126.60	254.80	5003.59
A19	1870.05	1067.74	2146.49	137.40	262.40	5484.08
A20	1835.80	1079.33	2002.11	133.05	266.40	5316.68
A21	1794.70	1012.99	1952.76	130.05	264.40	5154.89
A22	1507.00	912.25	1338.61	102.90	238.80	4099.56
A23	1705.65	1000.00	1584.79	118.50	265.60	4674.54
A24	2048.15	1096.17	2531.23	154.65	282.00	6112.21
A25	1596.05	922.78	1521.91	111.60	244.80	4397.14
A26	1698.80	1020.01	1775.24	121.20	256.00	4871.24
A27	1835.80	987.36	2029.88	133.80	260.80	5247.65
A28	1739.90	961.39	1890.86	126.45	255.20	4973.80
A29	1842.65	1101.09	1976.77	132.00	272.80	5325.31
A30	2123.50	1140.05	2383.70	151.05	300.40	6098.70

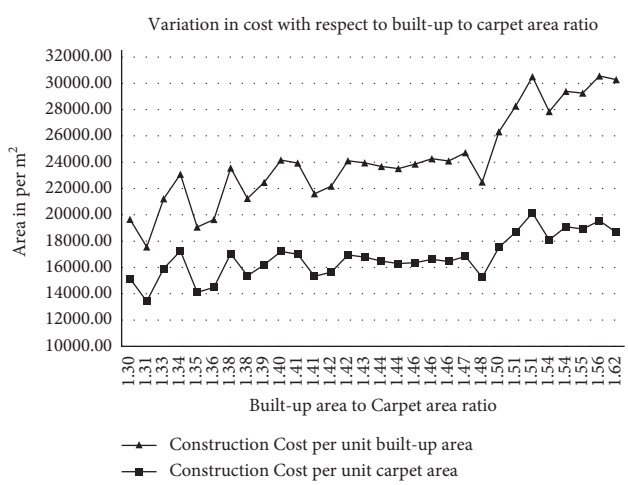

Figure 4: Variation in construction cost with respect to built-up-to-carpet area ratio.

circulation areas. This results in different built-up areas for the same carpet areas in different architectural designs. To reduce the overall cost and EE of any building, its architectural design must be efficiently planned so that the built-up-to-carpet area ratio is at the minimum.

5. Conclusion

As per the norms of the Government of India, a carpet area of 30 m^2 to 60 m^2 is proposed for economically weaker sections and low-income groups. The total usable area (carpet area) per IAHU is calculated by subtracting the area consumed in the circulation spaces plus the area occupied by external walls from built-up areas. Increasing the area in common or circulation spaces reduces effective usable or carpet area per IAHU in a cluster, which increases consumption of construction materials. This results in an increase in construction cost and embodied energy of IAHUs. Thus, the built-up-to-carpet area ratio plays a major role in the sustainable and affordable design of IAHUs. This can be achieved by an efficient architectural design having more carpet area in a given built-up area, keeping the built-up-to-carpet area ratio minimum. The embodied energy of these houses is estimated as varying from 4 to 6.5 GJ/sqm of carpet area and with the built-up-to-carpet area ratio varying from 1.3 to 1.62; these values are 30%–62% higher on built-up area's basis, which is in line with embodied energy of low-rise Indian affordable houses (1.6–5.0 GJ/sqm) calculated by many researchers. This study is based on the analysis of 30 numbers of low-rise load-bearing designs of IAHUs of the most common typologies. In designing sustainable and affordable housing, it is essential to choose an efficient architectural design, which has the least variation in the ratio of the built-up and carpet area so that its CC and EE are minimized. Much information is available on construction materials about their cost and embodied energy, but very few researchers have worked on the efficiency of architectural design to design sustainable buildings. Efficient architectural designs are essential as 30% to 62% of the carpet area goes into external walls and circulation spaces, resulting in variation in embodied energy by 62.5% and construction cost by 50%, which can be optimized in sustainable affordable housing. The built-up-to-carpet area ratio can give a true picture of the efficiency of affordable housing.

Abbreviations

Carpet area:	Floor area of a building within external walls
Load-bearing construction:	System of building construction, in which masonry/walls are the main load transferring members
RCC:	Reinforced cement concrete
RCC framed construction:	System of building construction, in which RCC columns and beams are the main load transferring members
M25:	Cement concrete, whose 28 days characteristic strength is 25 MPa (Mega Pascal)
TMT:	Thermomechanically treated steel reinforcing bars
Plinth/built-up area:	Carpet area plus floor area occupied by external walls along with proportional common/circulation areas including areas under lifts & staircases
PMAY:	Pradhan Mantri Awas Yojna (affordable housing scheme in India)
Indian affordable houses:	These are naturally ventilated houses constructed with local construction materials for the poor, having about 20–30 m^2 carpet area with two habitable rooms, one toilet & bath and kitchen, bare minimum furnishings, with an average service life of about 50 years
EWS:	Economically weaker section
EE:	Embodied energy
OE:	Operational energy
CC:	Construction cost
IAHU:	Indian affordable housing units
LCA/LCEA:	Life cycle analysis/life cycle energy analysis
1 USD ($):	73 INR as in May 2021.

Data Availability

All the data used in this work are available from the corresponding author upon reasonable request.

Conflicts of Interest

The authors declare that they have no conflicts of interest.

Acknowledgments

The authors are thankful for and acknowledge the support and help provided by Mrs. Manju Safaya, Ex. Executive Director (Design), HUDCO, New Delhi, India, for providing permission to use the housing data of the HUDCO for carrying out this research. The authors are also thankful to Dr Shailesh Kr. Agarwal, Executive Director, Building Materials and Technology Promotion Council (BMTPC), New Delhi, India, and Ms Yashika Bansal, student of B. Design, FDDI, Noida, India, for constant encouragement and help in analyzing data and for critical comments during this study.

References

[1] Ipcc, *Working Group III Contribution to the Fourth Assessment*, Report of the IPCC [AR4], 2007.

[2] T. Ramesh, R. Prakash, and K. Kumar Shukla, "Life cycle energy analysis of a multifamily residential house: a case study in indian context," *Open Journal of Energy Efficiency*, vol. 2, no. 1, pp. 34–41, 2013.

[3] L. Pinky Devi and S. Palaniappan, "Life cycle energy analysis of a low-cost house in India," *International Journal of Construction Education and Research*, vol. 15, no. 4, pp. 256–275, 2018.

[4] J. S. Paulsen and R. M. Sposto, "A life cycle energy analysis of social housing in Brazil: case study for the program "my house my life"," *Energy and Buildings*, vol. 57, pp. 95–102, 2013.

[5] I. C. Ezema, A. O. Olotuah., and O. I. Fagbenle, "Estimating embodied energy in residential buildings in a Nigerian context," *International Journal of Applied Engineering Research*, vol. 10, no. 24, pp. 44140–44149, 2015.

[6] R. Barbara, M. Anne-Françoise, G. Mauritz, and R. Sigrid, "Life-cycle assessment of residential buildings in three different European building and environment," *Building and Environment*, vol. 51, pp. 395–401, 2012.

[7] D. Bansal, R. Singh, and R. L. Sawhney, "Effect of construction materials on embodied energy and cost of buildings-a case study of residential houses in India up to 60m2 of plinth area," *Energy and Buildings*, vol. 69, pp. 260–266, 2014.

[8] M. K. Dixit, J. L. Fernández-Solís, S. Lavy, and C. H. Culp, "Need for an embodied energy measurement protocol for buildings: a review paper," *Renewable and Sustainable Energy Reviews*, vol. 16, no. 6, pp. 3730–3743, 2012.

[9] L. Pinky Devi and S. Palaniappan, "A case study on life cycle energy use of residential building in Southern India," *Energy and Buildings*, vol. 80, pp. 247–259, 2014.

[10] C. K. Chau, T. M. Leung, and W. Y. Ng, "A review on life cycle assessment, life cycle energy assessment and life cycle carbon emissions assessment on buildings," *Applied Energy*, vol. 143, pp. 395–413, 2015.

[11] P. Crowther, "Design for disassembly to recover embodied energy," in *Proceedings of the 16th International Conference on Passive and Low Energy Architecture*, S. S. Szokolay, Ed., pp. 22–24, Melbourne, Brisbane, Cairns, September 1999.

[12] N. Sengupta, S. Roy, and H. Guha, "Assessing embodied GHG emission reduction potential of cost-effective technologies for construction of residential buildings of Economically Weaker Section in India," *Asian Journal of Civil Engineering*, vol. 19, no. 2, pp. 139–156, 2018.

[13] T. Ramesh, R. Prakash, and K. K. Shukla, "Life cycle energy analysis of buildings: an overview," *Energy and Buildings*, vol. 42, no. 10, pp. 1592–1600, 2010.

[14] P. Winistorfer, Z. Chen, B. Lippke, and N. Stevens, "Energy consumption and greenhouse gas emissions related to the use, maintenance, and disposal of a residential structure," *Wood and Fiber Science*, vol. 37, no. 2007, pp. 128–139, 2007.

[15] W. David, E. Lucia, W. Russel, and F. Chris, "Climate change influence on building lifecycle greenhouse gas emissions: case study of a UK mixed-use development," *Energy and Buildings*, vol. 48, pp. 112–126, 2012.

[16] T. Y. Chen, J. Burnett, and C. K. Chau, "Analysis of embodied energy use in the residential building of Hong Kong," *Energy*, vol. 26, no. 4, pp. 323–340, 2001.

[17] A. Stephan, R. H. Crawford, and K. de Myttenaereb, "A comprehensive assessment of the life cycle energy demand of passive houses," *Applied Energy*, vol. 112, pp. 23–34, 2013.

[18] A. Utama and S. H. Gheewala, "Life cycle energy of single landed houses in Indonesia," *Energy and Buildings*, vol. 40, no. 10, pp. 1911–1916, 2008.

[19] A. Debnath, S. V. Singh., and Y. P. Singh, "Comparative assessment of energy requirements for different types of residential buildings in India," *Energy and Buildings*, vol. 23, no. 2, pp. 141–146, 1995.

[20] D. Bansal, V. K. Minocha, and K. Arvinder, "Embodied energy, CO_2e, and construction cost of indian housing: model of low-rise versus high-rise development," *Journal of Architectural Engineering*, vol. 27, no. 3, 2021.

[21] L. Gustavsson and A. Joelsson, "Life cycle primary energy analysis of residential buildings," *Energy and Buildings*, vol. 42, no. 2, pp. 210–220, 2010.

[22] U. Y. A. Tettey, A. Dodoo, and L. Gustavsson, "Effects of different insulation materials on primary energy and CO_2 emission of a multi-storey residential building," *Energy and Buildings*, vol. 82, pp. 369–377, 2014.

[23] X. G. Casals, "Analysis of building energy regulation and certification in Europe: their role, limitations and differences," *Energy and Buildings*, vol. 38, no. 5, pp. 381–392, 2006.

[24] A. Z.-Z. Szalay, "What is missing from the concept of the new European building directive?" *Building and Environment*, vol. 42, no. 4, pp. 1761–1769, 2007.

[25] S. S. Shrestha, K. Biswas, and A. O. Desjarlais, "A protocol for lifetime energy and environmental impact assessment of building insulation materials," *Environmental Impact Assessment Review*, vol. 46, pp. 25–31, 2014.

[26] F. Luisa, B. Camila, M. Josep, B. Esther, and A. Inés Fernández, "Low carbon and low embodied energy materials in buildings: a review," *Renewable and Sustainable Energy Reviews*, vol. 23, pp. 536–542, 2013.

[27] F. H. Abanda and J. H. M. Tah, F. K. T. Cheung, "Mathematical modelling of embodied energy, greenhouse gases, waste, time-cost parameters of building projects: a review," *Building and Environment*, vol. 59, pp. 23–37, 2013.

[28] A. Dodoo, L. Gustavsson, and R. Sathre, "Building energy-efficiency standards in a life cycle primary energy perspective," *Energy and Buildings*, vol. 43, no. 7, pp. 1589–1597, 2011.

[29] G. A. Keoleian, S. Blanchard, and P. Reppe, "Life-cycle energy, costs, and strategies for improving a single-family house," *Journal of Industrial Ecology*, vol. 4, no. 2, pp. 135–156, 2000.

[30] Ministry of Housing & Urban Affairs, *Affordable Housing*, http://mohua.gov.in/w_new/AffordableHousing.pdf - accessed on 2-March-2019, 2019.

[31] D. Bansal, V. K. Minocha, and A. Kaur, "Componentwise-embodied energy analysis of affordable houses in India," *Asian Journal of Civil Engineering*, vol. 21, no. 1, pp. 137–145, 2020.

[32] D. Sutapa, "Analysis of energy saving potential of a residential building complex using energy conservation building code 2017," in *Proceedings of the annual International conference on Architecture and Civil Engineering (ACE 2018)*, pp. 23–31, Singapore, May 2018.

[33] J. Oyarzo and B. Peuportier, "Life cycle assessment model applied to housing in Chile," *Journal of Cleaner Production*, vol. 69, pp. 109–116, 2014.

[34] P. K. Das, "Planning and design for sustainable habitat: adoption of appropriate and green construction technologies-the need of the day," in *Proceedings of the National Seminar on Design & Planning for Sustainable Habitat*, IDRC,CRDI, HSMI HUDCO, Background Papers, New Delhi, July 2011.

[35] F. Pomponi, C. De Wolf, and A. Moncaster, *Embodied Carbon in Buildings: Measurement, Management, and Mitigation*, Springer Science, New York, NY, USA, 2018.

[36] European Standard 15978, *Sustainability of Construction Works -ASSESSMENT of Environmental Performance of Buildings - Calculation Method*, p. 66, European Committee for Standardization (CEN), Brussels, Belgium, 2011.

[37] M. K. Dixit, "Life cycle embodied energy analysis of residential buildings: a review of literature to investigate embodied energy parameters," *Renewable and Sustainable Energy Reviews*, vol. 79, pp. 390–413, 2017.

[38] A. Stephan and R. H. Crawford, "The relationship between house size and life cycle energy demand: implications for

energy efficiency regulations for buildings," *Energy*, vol. 116, no. 1, pp. 1158–1171, 2016.

[39] R. Pacheco-Torres, E. Jadraque, J. Roldán-Fontana, and J. Ordóñez, "Analysis of CO_2 emissions in the construction phase of single-family detached houses," *Sustainable Cities and Society*, vol. 12, pp. 63–68, 2014.

[40] A. Stephan and A. Athanassiadis, "Quantifying and mapping embodied environmental requirements of urban building stocks," *Building and Environment*, vol. 114, pp. 187–202, 2017.

[41] L. Antonín, N. Marie, M. Štěpán et al., "Design strategies for buildings with low embodied energy," *Proceedings of the Institution of Civil Engineers - Engineering Sustainability*, vol. 170, no. 2, pp. 65–80, 2017.

[42] L. Vukotic, R. A. Fenner, and K. Symons, "Assessing embodied energy of building structural elements," *Proceedings of the Institution of Civil Engineers - Engineering Sustainability*, vol. 163, no. 3, pp. 147–158, 2010.

[43] Z. Worth, C. Boyle, and W. R. McDowall, "Combined life-cycle cost assessment of roof construction," *Proceedings of the Institution of Civil Engineers - Engineering Sustainability*, vol. 160, no. 4, pp. 189–198, 2007.

[44] B. Deepak and V. K. Minocha, "Analysis of low-rise vs. high rise development of affordable housing in India, for cost and energy optimization," in *Proceedings of the International Conference on Clean Technologies and Sustainable Development*, pp. 105–111, NITTTR Chandigarh and DOST, GOI, Chandigarh, February 2018.

[45] National Building Code 2016, "Bureau of Indian standards," 2016, http://www.bis.org.in/sf/nbc.html -accessed on 2-March-2015.

[46] A. B. Saka and D. W. M. Chan, "Knowledge, skills and functionalities requirements for quantity surveyors in building information modelling (BIM) work environment: an international Delphi study," *Architectural Engineering and Design Management*, vol. 16, no. 3, pp. 227–246, 2019.

[47] A. F. Mohamed, M. Mokhtar, and S. Elghobashy, "Comparative study of bio-materials versus conventional materials in building construction methods; economical evaluation of different building materials," *SN Applied Sciences*, vol. 1, no. 10, 2019.

[48] B. Borah, V. Singhal, and H. B. Kaushik, "Sustainable housing using confined masonry buildings," *SN Applied Sciences*, vol. 1, no. 9, 2019.

[49] Development Alternatives (Da), *Energy Directory of Building Materials*, Building Materials & Technology Promotion Council, New Delhi, India, 1995.

[50] Bmtpc (Building Materials and Technology Promotion council, New Delhi, http://www.bmtpc.org.

[51] V. A. Dakwale, R. V. Ralegaonkar, and S. Mandavgane, "Improving environmental performance of building through increased energy efficiency: a review," *Sustainable Cities and Society*, vol. 1, no. 4, pp. 211–218, 2011.

[52] B. V. Venkatarama Reddy and K. S. Jagadish, "Embodied energy of common and alternative building materials and technologies," *Energy and Buildings*, vol. 35, no. 2, pp. 129–137, 2003.

[53] A. Shukla, G. N. Tiwari., and M. S. Sodha, "Embodied energy analysis of adobe house," *Renewable Energy*, vol. 34, no. 3, pp. 755–761, 2009.

[54] *Inventory of Carbon & Energy*, University of Bath, 2011, http://www.bath.ac.uk/mech-engg/sert/embodied.

[55] Central Public Works Department (Cpwd 2019), *Plinth Rates*, https://cpwd.gov.in/Publication/PLINTH_AREA_RATES_2019.pdf -accessed on 5-November-2020.